



Communications  
Research Centre  
Canada

An Agency of  
Industry Canada

Centre de recherches  
sur les communications  
Canada

Un organisme  
d'industrie Canada

# Ka-Band Holographic Antennas

*by Kathia Lévis*

**Advanced Antenna Technology**

IC

LKC  
TK  
5102.5  
.C673e  
#2000-002  
002  
c.2

Canada

**CRC Report No. CRC-RP-2000-002  
January 27, 2000**

CRC

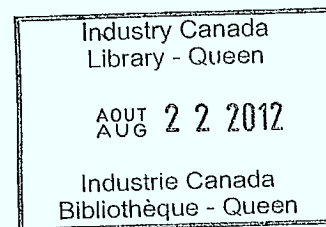
TTc  
S102.5  
C673e  
# 2000-002  
C.e.  
S-Gen

# Ka-Band Holographic Antennas

By Kathia Lévis

~~CRC LIBRARY~~  
~~-03-19 2000~~  
~~BIBLIOTHEQUE~~

Advanced Antenna Technology



CRC Report No. CRC-RP-2000-002  
January 27, 2000



## ABSTRACT

In this work holographic antennas are investigated as an alternate technology to reflectors and microstrip phased arrays for use in Ka-band applications. These antennas combine the advantages of low profile printed technology with an unconstrained feed to avoid excessive losses associated with conventional phased array feeds.

The main purpose of this work is to apply optical holography theory at microwave frequencies in the design of Ka-band holographic antennas. As with optical frequencies, the interference pattern between two waves is calculated in order to generate the hologram. The simplest pattern is a zone plate representing the destructive pattern which can be easily reproduced using microstrip technology. To fabricate the antennas, conductor strips are etched on a dielectric material where the two interfering waves are  $180^\circ$  out of phase. The hologram is then illuminated by the reference wave to reconstruct the desired antenna pattern. An interesting feature of these antennas is that they can be designed so that the feed is in the same plane as the holographic plate, making the structures almost flat and preventing feed aperture blockage.

Measurements of various prototypes validated the holographic concept and have shown that the efficiency of the proposed holographic antennas is comparable to that of Ka-band passive phased arrays with conventional microstrip feeds. Also, based on the experimental results, some design guidelines are established along with a methodology for enhancing the efficiency. The efficiency-improvement methods include multi-layer structures, feed horns, dipole-holograms, diamond-shaped holograms, and many others.

## TABLE OF CONTENTS

<b>CHAPTER 1 Introduction .....</b>	<b>1</b>
1.1 Background and Motivations.....	1
1.2 Thesis Objectives.....	3
1.3 Thesis Contributions.....	4
1.4 Thesis Organization.....	5
<b>CHAPTER 2 Review of Hologram Theory and Application to an Antenna.....</b>	<b>7</b>
2.1 Definition of Optical Holography.....	7
2.1.1 Recording of the hologram.....	8
2.1.2 Reconstruction of the object wave .....	9
2.2 Interference Pattern between a Spherical Wave and a Plane Wave .....	10
2.2.1 General case .....	10
2.2.2 Special case: destructive interference pattern .....	14
2.3 Application of Hologram Theory at Microwave Frequencies.....	17
2.3.1 Holographic antennas.....	17
2.3.2 Specific case of a holographic antenna .....	18
2.3.3 General approximations .....	22
<b>CHAPTER 3 Microwave Analysis of Holograms .....</b>	<b>23</b>
3.1 Array Theory .....	23
3.1.1 General review .....	23
3.1.2 Beam scan versus frequency and the guided wavelength .....	25
3.1.3 Far-field radiation pattern.....	29
3.1.4 Dipole hologram.....	33
3.1.5 Two-layer hologram.....	37
3.2 Surface Wave Analysis.....	39
3.2.1 Guided wavelength from the characteristic equations .....	39
3.2.2 Guided wavelength from the point matching approach .....	43
3.2.3 Traveling wave antennas constructed from periodic structures .....	44
3.3 Incident Plane Wave on a Dielectric Sheet .....	50

<b>CHAPTER 4 Holographic Antenna Concept Validation and Design Procedure.....</b>	<b>53</b>
4.1 Validation of a Holographic Antenna.....	53
4.1.1 Prototype and test setup.....	53
4.1.2 Dipole hologram.....	62
4.2 Efficiency and Beam Squint Considerations .....	67
4.3 Design Procedure of a Holographic Antenna .....	71
<b>CHAPTER 5 Holographic Antenna Enhancement Techniques.....</b>	<b>72</b>
5.1 Efficiency Enhancement Techniques .....	72
5.1.1 Two-layer hologram for back lobe suppression.....	72
5.1.2 Feed horn integration for illumination efficiency improvement.....	79
5.1.3 Evaluation of the focal points of a feed horn for phase error reduction.....	83
5.1.4 Diamond-shaped hologram .....	86
5.1.5 Microstrip line width investigations.....	91
5.1.6 Dipole hologram: second design .....	95
5.2 Beam Squint Corrected Hologram .....	98
5.3 Discussion.....	103
5.3.1 Efficiency considerations .....	103
5.3.2 Beam squint issues .....	113
<b>CHAPTER 6 Conclusions and Future Work .....</b>	<b>116</b>
<b>APPENDIX A Point Matching Approach .....</b>	<b>121</b>
<b>APPENDIX B Frame.....</b>	<b>126</b>
<b>APPENDIX C Evaluation of the Dielectric Constant of the Foam .....</b>	<b>128</b>
<b>APPENDIX D H-Plane Sectoral Horn and Pyramidal Horn .....</b>	<b>131</b>
D.1 H-Plane Sectoral Horn.....	131
D.2 Pyramidal Horn.....	136
D.2.1 General description.....	136
D.2.2 Apex and phase center.....	138
<b>REFERENCES.....</b>	<b>142</b>

## LIST OF FIGURES

Figure 2.1. Recording the hologram. ....	8
Figure 2.2. Generation of the object wavefront. ....	9
Figure 2.3. Interference between spherical wave and plane wave. ....	10
Figure 2.4. Normalized interference pattern between spherical wave and plane wave. ....	12
Figure 2.5. Reconstruction of the four wave components. ....	13
Figure 2.6. Destructive interference pattern between spherical wave and plane wave for two locations of point source. ....	15
Figure 2.7. Location of recording medium ....	15
Figure 2.8. Reconstruction of destructive pattern. ....	16
Figure 2.9. Generation of the plane wave ....	19
Figure 2.10. Holographic antenna's layout (area enclosed by dotted lines). ....	20
Figure 2.11. Scattering introduced by single strip. ....	21
Figure 2.12. Predicted far-field radiation pattern. ....	21
Figure 3.1. Uniform array. ....	23
Figure 3.2. Phase delay at frequency $f$ . ....	26
Figure 3.3. Geometry for far-field observation [19]. ....	29
Figure 3.4. Array of loop antennas. ....	31
Figure 3.5. Normalized radiation pattern of holographic antenna approximated by an array of circular arcs. ....	32
Figure 3.6. Dipole holographic antenna. ....	33
Figure 3.7. Dipole Hologram ....	34
Figure 3.8. H-plane normalized radiation pattern of holographic antenna approximated by an array of free-space dipoles. ....	35
Figure 3.9. E-plane normalized radiation pattern of holographic antenna approximated by an array of free-space dipoles. ....	36
Figure 3.10. Two-layer hologram ....	37
Figure 3.11. Lobe suppression. ....	38
Figure 3.12. Dielectric slab. ....	40
Figure 3.13. $\kappa_o$ versus $\beta_z$ for infinitely wide slab with $t = 0.0508cm$ ....	42

Figure 3.14. Dielectric waveguide. ....	43
Figure 3.15. Periodic approximation of the holographic antenna.....	45
Figure 3.16. Classification of the $\kappa_o - \beta_z$ plane [25].....	45
Figure 3.17. $\kappa_o$ versus $\beta_z$ for a periodically loaded traveling-wave structure. ....	46
Figure 3.18. Beam squint at two different frequencies.....	49
Figure 3.19. Incident wave on dielectric sheet. ....	50
Figure 4.1. Holographic Antenna.....	54
Figure 4.2. Focal point with respect to hologram. ....	55
Figure 4.3. Radiation pattern of holographic antenna at $f_o = 30GHz$ . ....	56
Figure 4.4. Radiation lobes with respect to the hologram. ....	56
Figure 4.5. Radiation pattern of the optimized single-layer holographic antenna at $f_o = 30GHz$ . .....	58
Figure 4.6. H-plane radiation pattern of feed without holographic antenna. ....	59
Figure 4.7. Antenna setup. ....	61
Figure 4.8. H-plane radiation patterns of the dipole hologram for $d = \lambda_o$ .....	63
Figure 4.9. E-plane co-polarization patterns at $f = 28GHz$ .....	64
Figure 4.10. Measured E-plane cross-polarization patterns at $f = 28GHz$ .....	65
Figure 4.11. E-plane cross-polarization test setup for feed pattern measurement. ....	66
Figure 4.12. Radiation pattern of the open waveguide. ....	68
Figure 4.13. Open waveguide. ....	68
Figure 4.14. Illumination efficiency .....	69
Figure 5.1. Two-layer hologram with spacers. ....	73
Figure 5.2. H-plane radiation pattern of the two-layer hologram ( $f = 30GHz$ ).....	74
Figure 5.3. H-plane radiation pattern of the double-sided hologram ( $f = 30GHz$ ).....	75
Figure 5.4. Optimized two-layer hologram configuration.....	76
Figure 5.5. H-plane radiation pattern of optimized two-layer hologram ( $f = 28GHz$ ).....	76
Figure 5.6. H-plane radiation pattern of double-sided hologram ( $f = 28GHz$ ).....	77
Figure 5.7. Measured $ S_{11} $ of feed waveguide. ....	78
Figure 5.8. Radiation pattern of the holographic antenna with feed horn #1. ....	80

Figure 5.9. Radiation pattern of the holographic antenna with feed horn #3. ....	80
Figure 5.10. Radiation pattern of the holographic antenna with pyramidal horn. ....	81
Figure 5.11. $ S_{11} $ of single-layer hologram with different feeds. ....	82
Figure 5.12. Hologram generated from two point sources ....	84
Figure 5.13. Radiation pattern of single-layer hologram at different focal points. ....	85
Figure 5.14. $ S_{11} $ of single-layer hologram at different focal points. ....	86
Figure 5.15. H-plane radiation pattern of diamond-shaped hologram with open waveguide feed ( $f = 30GHz$ ). ....	87
Figure 5.16. E-plane cross-polarization radiation pattern of diamond-shaped hologram with open waveguide feed ( $f = 28GHz$ ). ....	88
Figure 5.17. H-plane radiation pattern with horn #3 ( $f = 30GHz$ ). ....	89
Figure 5.18. $ S_{11} $ of the diamond-shaped and square-shaped hologram. ....	90
Figure 5.19. $ S_{11} $ of diamond-shaped and square-shaped holograms at second focal point. ....	91
Figure 5.20. H-plane co-polarization radiation pattern for varying the hologram strip widths ( $f = 30GHz$ ). ....	92
Figure 5.21. H-plane cross-polarization radiation pattern for varying the hologram strip widths ( $f = 30GHz$ ). ....	93
Figure 5.22. $ S_{11} $ of holographic antenna with varying strip widths. ....	95
Figure 5.23. H-plane radiation pattern of dipole holograms ( $f = 30GHz$ ). ....	96
Figure 5.24. E-plane cross-polarization pattern of dipole holograms ( $f = 28GHz$ ). ....	97
Figure 5.25. $ S_{11} $ of feed, continuous-strip and dipole holograms. ....	97
Figure 5.26. H-plane radiation pattern of beam squint corrected hologram ( $f = 30GHz$ ). ....	99
Figure 5.27. H-plane radiation patterns of beam squint corrected hologram. ....	100
Figure 5.28. $ S_{11} $ of beam squint corrected and non-corrected holograms. ....	102
Figure B.1. Frame. ....	126
Figure B.2. Dimensions. ....	127
Figure C.1. Open waveguide test setup. ....	128
Figure D.1. Dimensions of open waveguide. ....	131

Figure D.2. Dimensions of the H-plane sectoral horn. ....	131
Figure D.3. H-plane sectoral horns. ....	132
Figure D.4. H-plane sectoral horn #1 ( $20^\circ$ Beamwidth). ....	133
Figure D.5. H-plane sectoral horn #2 ( $28^\circ$ Beamwidth). ....	134
Figure D.6. H-plane sectoral horn #3 ( $37^\circ$ Beamwidth). ....	134
Figure D.7. Open aperture of H-plane sectoral horns. ....	135
Figure D.8. $ S_{//} $ of H-plane sectoral horns ....	136
Figure D.9. Pyramidal horn. ....	137
Figure D.10. Radiation patterns of pyramidal horn (horn #4). ....	137
Figure D.11. $ S_{//} $ of pyramidal horn. ....	137
Figure D.12. H-plane apex. ....	138
Figure D.13. E-plane apex. ....	140



## LIST OF TABLES

Table 3.1 Characteristics of circular arcs in array .....	32
Table 3.2 General solutions .....	40
Table 4.1 General properties of holographic antenna .....	54
Table 4.2 Beam peak at various frequencies .....	60
Table 4.3 Dielectric constant of foam .....	62
Table 5.1 General properties of two-layer holographic antennas .....	73
Table 5.2 Radiation pattern results at $f = 30GHz$ .....	81
Table 5.3 Gain results .....	82
Table 5.4 Radiation pattern results .....	85
Table 5.5 Holographic antenna with different strip widths .....	92
Table 5.6 Varying the hologram strip widths test results at $f = 30GHz$ .....	93
Table 5.7 Gain of holographic antennas at different frequencies .....	94
Table 5.8 Beam squint from broadside for two holographic antennas .....	101
Table 5.9 Gain results for two holographic antennas .....	101
Table C.1 Return loss measurements .....	129
Table C.2 Dielectric constant of foam .....	130
Table D.1 H-plane sectoral horn characteristics .....	132
Table D.2 New H-plane sectoral horn characteristics .....	133
Table D.3 H-plane sectoral horn results .....	134
Table D.4 Apex and phase center of pyramidal horn .....	141

## GLOSSARY

$a$	amplitude of a plane wave; or radius of loop antenna; or dimension of waveguide
$a_l$	dimension of open aperture of sectoral horns
$\hat{a}'_r$	unit radial vector
$\hat{a}'_\phi$	unit $\phi$ vector
$\hat{a}'_\rho$	unit $\rho$ vector
$A$	amplitude of a spherical wave; or aperture area
$\bar{A}$	array pattern
$\vec{A}$	vector potential
$AF$	array factor
$b$	dimension of waveguide
<b>B</b>	back lobe
$c$	speed of light in free-space; or dimension of waveguide
$d$	distance between elements in antenna array; or dimension of sectoral horns
$D$	directivity
$dl'$	infinitesimal section of the loop antenna
$E_x$	magnitude of the electric field in the $x$ direction
$E_y$	magnitude of the electric field in the $y$ direction
$E_z$	magnitude of the electric field in the $z$ direction
$E_r$	magnitude of the electric field in the radial direction
$E_\phi$	magnitude of the electric field in the $\phi$ direction
$E_\theta$	magnitude of the electric field in the $\theta$ direction
$\bar{E}$	element pattern
$\vec{E}$	electric field vector
$\vec{E}_{PW}$	electric field vector of a plane wave
$\vec{E}_{SW}$	electric field vector of a spherical wave
$f$	frequency in cycles per seconds [Hz]
<b>F</b>	front lobe
$f_c$	cutoff frequency of the rectangular waveguide
$f_o$	desired design frequency in cycles per seconds [Hz]
$f_p$	focal point
$G$	gain
$H_x$	magnitude of the magnetic field in the $x$ direction
$H_y$	magnitude of the magnetic field in the $y$ direction
$H_z$	magnitude of the magnetic field in the $z$ direction
$H_r$	magnitude of the magnetic field in the radial direction
$H_\phi$	magnitude of the magnetic field in the $\phi$ direction
$H_\theta$	magnitude of the magnetic field in the $\theta$ direction
$\vec{H}$	magnetic field vector
$i$	incident wave

$I$	intensity of interference pattern
$I_o$	constant current
$I_\phi$	current distribution on loop antenna
$\vec{I}_e$	current distribution
$j$	imaginary number $[\sqrt{-1}]$
$l$	length of open waveguide
$L$	any dimension for pyramidal horn
$L_a$	radius with respect to apex
$L_p$	radius with respect to phase center
$n$	an integer
$N$	number of elements in an antenna array
$P$	time-average power density
$r$	spherical radial component
$\mathbf{r}$	reflected wave
$R$	distance between any point on loop antenna and the observation point
$\vec{R}$	vector between any point on the loop antenna and an observation point
$s$	thickness of spacers
$S$	period of Floquet mode
$\mathbf{S}$	lobe towards the feed
$S_{11}$	input return loss
$t$	time; or thickness of dielectric slab; or thickness of metal edges of sectoral horns
$\mathbf{t}$	transmitted wave
$\mathbf{T}$	lobe on top of antenna
$T_s$	transmission coefficient
$U$	radiation intensity in units of $[W/unit\ solid\ angle]$
$U_c$	complex field of the reconstructed wave
$U_o$	complex field of the object wave
$U_r$	complex field of the reference wave
$w$	width of microstrip line
$x$	Cartesian coordinate
$x_o$	$x$ coordinate of point source
$\hat{x}$	unit $x$ vector
$y$	Cartesian coordinate
$y_o$	$y$ coordinate of point source
$\hat{y}$	unit $y$ vector
$z$	Cartesian coordinate
$z_o$	$z$ coordinate of point source; or recording medium
$\hat{z}$	unit $z$ vector
$\alpha_n$	phase excitation of each element in antenna array
$\beta$	phase constant
$\beta_p$	progressive phase excitation in array
$\delta$	phase error
$\Delta d$	incremental difference between $\lambda$ at $f_o$ and $\lambda$ at operating frequency $f$
$\Delta e$	dimension with respect to E-plane for pyramidal horn
$\Delta h$	dimension with respect to H-plane for pyramidal horn

$\Delta\phi$	phase delay
$\varepsilon$	permittivity, $(\varepsilon_o\varepsilon_r)$ in units of $[F/m]$
$\varepsilon_o$	permittivity of free-space $(8.854\cdot 10^{-12} [F/m])$
$\varepsilon_r$	dielectric constant of dielectric material
$\varepsilon_r^f$	dielectric constant of foam
$\varepsilon_{r,eff}$	effective dielectric constant of dielectric material
$\phi$	phase of reference wave; or phase of element in array; or spherical coordinate
$\phi_c$	critical angle
$\gamma$	propagation constant
$\Gamma_s$	reflection coefficient
$\eta$	intrinsic impedance of the medium
$\kappa$	any wave number
$\kappa_o$	wave number in free-space
$\lambda$	any wavelength in general
$\lambda_g$	wavelength in a dielectric medium (guide wavelength)
$\lambda_o$	wavelength in free-space
$\mu$	permeability, $(\mu_o\mu_r)$ in units of $[H/m]$
$\mu_o$	permeability of free-space $(4\pi\cdot 10^{-7} [H/m])$
$\mu_r$	relative permeability
$\theta$	phase of object wave; or spherical coordinate
$\theta_n$	beam peak angle value off broadside of Floquet mode
$\theta_s$	beam peak angle value off broadside
$\rho$	radius of spherical wavefront; or spherical coordinate
$\rho_2$	radius with respect to apex
$\rho_h$	length of open aperture of sectoral horns
$\omega$	angular frequency in units of $[rad/s]$
$\psi$	angle in units of $[rad]$
$\psi_h$	angle of open aperture of sectoral horns

## CHAPTER 1

### Introduction

#### 1.1 Background and Motivations

Several new applications are emerging at Ka-band frequencies (26-40GHz) including Local Multi-point Communication/Distribution Systems (LMCS/LMDS) and advanced satellite communications systems (SATCOM) [1-3]. These systems must be capable of delivering high-bandwidth multimedia signals, therefore providing simultaneous services such as voice, fax, high-speed Internet access, videoconferencing, and many others. Since these types of services are primarily targeted for business and home users, the systems require low-cost fixed or mobile user terminals. If the terminal is to be mounted on a house or on top of a car, then a low profile and light weight design are other requirements. Also, at Ka-band frequencies the signals are susceptible to impairments from obstacles such as rain, terrain variations, trees and buildings; therefore, the antennas must generally be in line of sight and provide high gain.

Traditionally, high gain reflectors, or parabolic antennas, are used at Ka-band due to their relatively high efficiency (up to 50%). As well, passive microstrip phased arrays are employed for their low profile and multi-beam capabilities. However, reflectors have a high profile, a heavy weight, and in many cases suffer from feed aperture blockage. An offset reflector configuration can be used to eliminate aperture blockage at the expense of compactness and complexity. At millimeter-wave frequencies the design of low profile printed phased arrays is challenging due to the high feed losses incurred. To compensate for these losses, amplifiers must be added in the feed network, which increases the complexity and the cost, and may

introduce additional problems such as oscillation and overheating. At the moment, active phased array antenna technology is far from mature and much research still remains to be done. Conventional lenses, which have efficiency similar to that of reflectors, are also potential candidates. However, as with reflectors, this technology is bulky and heavy, and has a limited beam scan range for multi-beam applications unless a complicated surface shaping is applied.

In this thesis holographic antennas are investigated as an alternate technology for use in Ka-band applications. These antennas combine the advantages of low-profile printed technology with an unconstrained feed to avoid excessive losses associated with conventional microstrip phased array feed networks. By varying the destructive interference pattern etched on a very thin dielectric slab or by mechanically moving the feed, it is possible to design low-cost dual-polarized, circular polarized, multi-beam, or scanned beam holographic antennas. Another interesting feature of these antennas is that they can be designed so that the feed is in the same plane as the holographic plate, making the structure almost flat and preventing feed aperture blockages.

Holography has been extensively utilized for various applications in optics. However, some researchers have also explored their potential applications at microwave frequencies. Kock [4] and Iizuka *et al.* [5] applied microwave holography for coherent detection of radar echoes. Microwave holography has been demonstrated to be a very useful technique for the measurement of surface accuracy of large reflector antennas [6-8]. Also, holography techniques have been successfully applied in near field antenna measurement systems where a holographic image of the antenna is created and then transformed into a far-field radiation pattern.

In the field of antenna design, however, microwave holography has received little attention. Only a few investigations have been reported in the literature. In 1970, Iisuka *et al.* [5] designed holographic antennas using conducting strips to generate the hologram representing a destructive interference pattern between spherical and plane waves. The strips were photoetched on a printed circuit board to create X-band antennas. In addition, the feed horn used to illuminate the hologram is in the same plane as the holographic plate resulting in a low profile antenna. Another type of antenna is the VHF holographic antenna fabricated from metallic posts, metallic strips and metallic rods tested by Checcacci *et al.* [9-10]. Other similar antennas consist of microwave zoned lenses also made of metal [4]. These holographic antennas investigated in the literature all have the same attractive feature: they can easily be fabricated based on a simple destructive interference pattern. It is interesting to note that Fresnel lens antennas and flat reflectors can be modeled using holography theory. Thus, there are potentially new types of high gain antennas which can be found by applying the principle of holography.

## 1.2 Thesis Objectives

The main purpose of this thesis is to apply optical holographic theory at microwave frequencies to design Ka-band holographic antennas. The idea, based on a simple optical concept, is to estimate the destructive interference pattern or the antenna's layout for a desired radiation pattern and reproduce this hologram using microstrip technology.

The first objective is to characterize and design holographic antennas. This step includes outlining the relationship that exists between optical holography and antenna theory at microwave frequencies, along with the microwave issues neglected at optical frequencies.



Based on initial analysis and experimental results, the second goal is to establish a design procedure for Ka-band holographic antennas and a methodology for improving their efficiency. The methodology will include investigating multi-layer structures, feed horns, and the issues of illumination and spillover efficiency, guided wavelength and focal point location.

The final objective is to assess the applicability of holographic antennas to LMCD/LMDS and Ka-band SATCOM systems. Therefore, throughout the thesis methods of improving the performance of the holographic antennas will be directed towards satisfying the required performance parameters of such systems. Again these parameters are low profile, low cost, and high efficiency.

### **1.3 Thesis Contributions**

Due to many limitations such as a low efficiency and a high profile, not much work has been done on holographic antennas since the 1970's. Also, most of the antennas fabricated at that time were designed at a lower frequency band than the one investigated in this thesis. Therefore, the first contribution is the application of hologram theory at Ka-band frequencies.

This thesis also provides design guidelines and useful mathematical tools for the design of holographic antennas at any frequency band of interest. To complete the design procedure, an efficiency-improvement methodology is also investigated.

New types of holographic antennas, such as the dipole hologram, the diamond-shaped hologram, and the double-sided hologram, are also introduced in this work. These antennas

resulted from an effort to improve the efficiency. Finally, some future ideas on holographic antennas are discussed to complete the work done so far. These ideas include multi-layer antennas, microstrip feeds, and interleaved holograms.

#### **1.4 Thesis Organization**

In Chapter 2, some background on optical hologram theory is presented to introduce and better understand the concept. The review of holography gives the mathematical tools necessary to generate the destructive interference pattern and fabricate holographic antennas using microstrip technology. The behavior of the radiated fields from the conducting strips of the antenna is then used to select the aperture size of the antenna and predict the far-field radiation pattern.

The third chapter consists of the microwave analysis of the holographic antenna. The antenna is treated in turn as an array of conducting strips, a traveling-wave antenna, and a periodic structure to evaluate the beam scan versus frequency and the guided wavelength. Array theory is also applied to calculate the H-plane radiation pattern and to design two-layer holograms. Finally, the guided wavelength of the dielectric slab is evaluated with a surface wave analysis.

Chapter 4 validates the holographic antenna concept developed in the two previous chapters. The design of the first prototypes and the measurement setup are described. The interference between the feed and the holographic antenna is studied as well, along with the beam squint and the effect of the dielectric slab on the main lobes. Then, based on the first

measurement results, some efficiency and beam-squint improvement techniques are considered and a general design procedure is presented for the development of holographic antennas.

All the efficiency considerations outlined in Chapter 4 are verified experimentally in Chapter 5. The measured results, such as radiation patterns and return loss, are illustrated and analyzed in detail so as to allow a complete discussion of holographic antenna performance at the end of the chapter.

The last chapter of the thesis, Chapter 6, outlines the highlights of the thesis work, presents the main conclusions and provides some possible suggestions for future work.

## **CHAPTER 2**

### **Review of Hologram Theory and Application to an Antenna**

A better understanding of the holographic antenna concept requires some background in hologram theory. This chapter offers a review of holography and provides all the mathematical tools necessary to design holographic antennas. The chapter also deals with the application of holograms at microwave frequencies and the effects of using a finite size hologram. Discussion of approximations in a hologram construction is also included.

#### **2.1 Definition of Optical Holography**

Optical holography is a well-established technology and has been extensively discussed in the literature [11-15]. An excellent review of optical holography can be found in [13] and [14]. Many descriptions of holograms have been presented such as a modulation process or as a coding process to store information [4]. In simple terms, a hologram can be defined as a two-dimensional (2-D) recording that produces a three-dimensional (3-D) image. In order to produce such an image, the recording media must store both the phase and magnitude of the optical wave coming from a coherently illuminated object. Because photographic plates or photodetectors such as film only respond to light intensity, the phase information of the optical wave must be converted to intensity variations using the interferometry techniques described in the following section.

### 2.1.1 Recording of the hologram

In order to record a hologram, a reference wave, which is a coherent wavefront of known amplitude and phase, is added to the unknown object wavefront on a recording medium, as shown in Figure 2.1. The reference wave can be represented by the complex field expression:

$$U_r(x, y) = |U_r(x, y)|e^{-j\phi(x, y)}, \quad (2-1)$$

and the object wave by:

$$U_o(x, y) = |U_o(x, y)|e^{-j\theta(x, y)}, \quad (2-2)$$

where  $(x, y)$  are the coordinates on the recording medium.

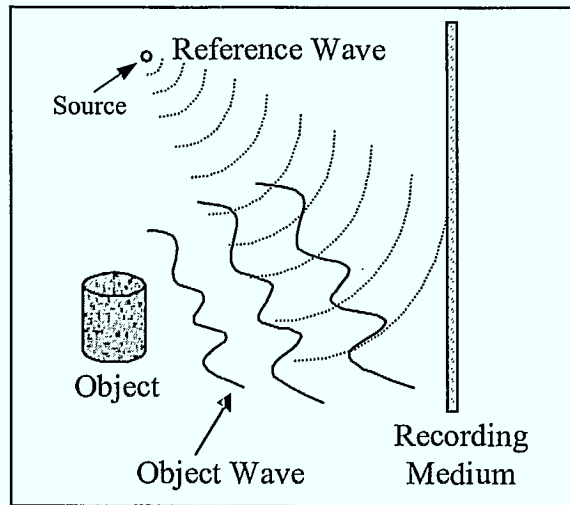


**Figure 2.1. Recording the hologram.**

At optical frequencies, the object wave is generated by illuminating the object with a laser (also referred to as the source) which at the same time is used to generate the reference wave as shown in Figure 2.2.

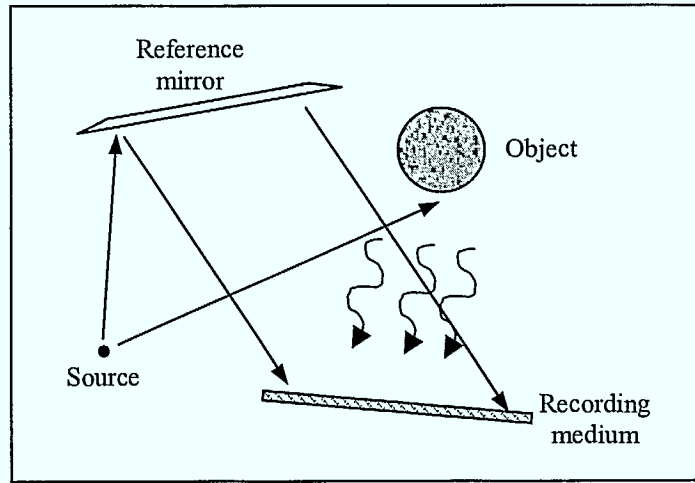


**Figure 2.2. Generation of the object wavefront.**

The intensity, or the interference pattern, of the two waves is given by:

$$\begin{aligned} I(x, y) &= |U_r(x, y) + U_o(x, y)|^2, \\ &= |U_r(x, y)|^2 + |U_o(x, y)|^2 + U_r^*(x, y)U_o(x, y) + U_r(x, y)U_o^*(x, y), \end{aligned} \quad (2-3)$$

where \* represents a complex conjugate. Equation (2-3) can be written as:

$$I(x, y) = |U_r(x, y)|^2 + |U_o(x, y)|^2 + 2|U_r(x, y)||U_o(x, y)| \cos[\phi(x, y) - \theta(x, y)]. \quad (2-4)$$

Equation (2-4) clearly indicates that the phase of both wavefronts is present in the intensity and will be recorded on the film. The intensity is maximum when the two waves add up. It is known as “constructive interference”. In the other case, it is known as “destructive interference” when the waves subtract from each other and the intensity is minimum.

### 2.1.2 Reconstruction of the object wave

To reconstruct (or see) the object’s wavefront, the recorded interference pattern must be illuminated by a similar coherent wavefront used to record the hologram. At the hologram plane,

diffraction will occur and the light waves will spread out such that a replica of the original object wave is created. Mathematically, the reconstructed wave can be expressed as follows:

$$\begin{aligned}
 U_c &= U_r(x, y)I(x, y), \\
 U_c &= U_r(x, y)|U_r(x, y)|^2 + U_r(x, y)|U_o(x, y)|^2 + |U_r(x, y)|^2 U_o(x, y) \\
 &\quad + [U_r(x, y)]^2 [U_o(x, y)]^*.
 \end{aligned} \tag{2-5}$$

From (2-5), the third term corresponds to a duplication of the original object wavefront multiplied by the factor  $|U_r(x, y)|^2$ . The other three terms can be separated from the reconstructed object wave by using various techniques described in [13-14]. To better visualize the reconstructed wave and understand how it behaves, the next section deals with an example of a hologram generated by interference between two familiar wavefronts: the spherical wave and the plane wave.

## 2.2 Interference Pattern between a Spherical Wave and a Plane Wave

### 2.2.1 General case

Consider the case where the reference wavefront is a spherical wave (SW) generated by a point source at coordinates  $(x_o, y_o, z_o)$ , and the object wavefront is a plane wave (PW) normally incident on the recording medium, as shown in Figure 2.3.

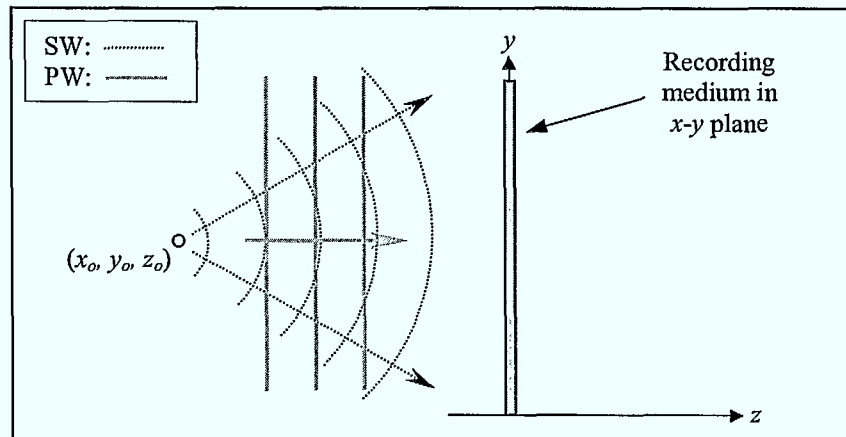


Figure 2.3. Interference between spherical wave and plane wave.



In general, the plane wave can be obliquely incident on the recording medium, but only the normally incident case is considered in this thesis. Assuming both wavefronts have constant amplitude across the entire  $x$ - $y$  plane, identical polarisation, and are propagating in a lossless medium, the complex field for the outgoing spherical wave is defined as:

$$U_r = A \exp \left\{ -j \frac{2\pi}{\lambda} \sqrt{(x - x_o)^2 + (y - y_o)^2 + (z - z_o)^2} \right\}, \quad (2-6)$$

and the incoming plane wave is defined as:

$$U_o = a e^{-j\beta z} = a e^{j\theta(z)}, \quad (2-7)$$

where  $\beta = \frac{2\pi}{\lambda}$ . Note that the implicit  $e^{j\omega t}$  time dependency is suppressed throughout. Placing the recording medium at  $z = z_o$  and the point source at  $x_o = y_o = 0$  and  $z_o$  (same plane as the recording medium), (2-6) simplifies to:

$$U_r = A e^{-j \frac{2\pi}{\lambda} \sqrt{x^2 + y^2}} = A e^{-j \frac{2\pi}{\lambda} \rho} = A e^{j\phi(\rho)}, \quad (2-8)$$

where  $\rho = \sqrt{x^2 + y^2}$  and  $\phi(\rho) = -\frac{2\pi}{\lambda} \rho$ . From the general expression, the interference pattern at the recording medium is:

$$\begin{aligned} I &= A^2 + a^2 + A a e^{-j\phi(\rho) + j\theta(z_o)} + A a e^{j\phi(\rho) - j\theta(z_o)}, \\ I &= A^2 + a^2 + 2 A a \cos(\phi(\rho) - \theta(z_o)). \end{aligned} \quad (2-9)$$

The interference pattern shows the recording of both the amplitude and the phase of the object wave. Equation (2-9) generates the normalized pattern illustrated in Figure 2.4 (assuming  $a = A$ ). This pattern is often referred to as a zone plate where the opaque regions correspond to an intensity of zero, and the white regions to maximum transmittance.

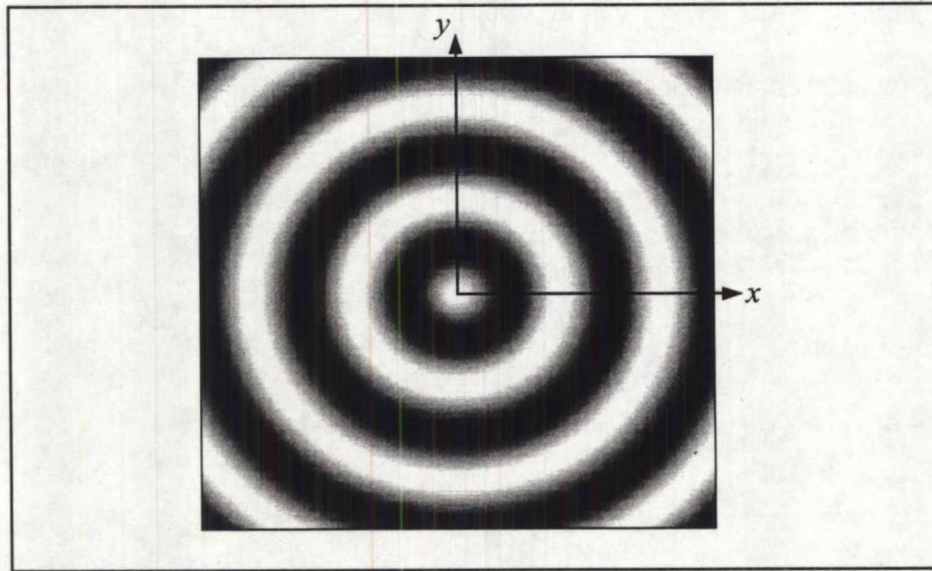


**Figure 2.4. Normalized interference pattern between spherical wave and plane wave.**

At reconstruction, a spherical wave illuminates the hologram and the field generated by the process is:

$$\begin{aligned} U_c &= Ae^{j\phi(\rho)}I, \\ U_c &= A^3e^{j\phi(\rho)} + Aa^2e^{j\phi(\rho)} + A^2ae^{j\theta(z)} + A^2e^{j2\phi(\rho)}ae^{-j\theta(z)}. \end{aligned} \quad (2-10)$$

Equation (2-10) can be broken down into four wave expressions where:

$$\begin{aligned} U_1 &= A^3e^{j\phi(\rho)}, \\ U_2 &= Aa^2e^{j\phi(\rho)}, \\ U_3 &= A^2ae^{j\theta(z)}, \\ U_4 &= A^2e^{j2\phi(\rho)}ae^{-j\theta(z)}. \end{aligned} \quad (2-11)$$

The first two waves are simply the spherical wave multiplied by a constant factor and will follow the same direction of propagation as the reference wave as shown in Figure 2.5. The field of interest  $U_3$ , which corresponds to the plane wave (or the object wave), will continue to propagate in the positive  $z$  direction. As for the fourth term ( $U_4$ ), because it is the conjugate of

the original object wavefront, it will propagate in the negative  $z$  direction and be affected by an additional phase factor of  $e^{j2\phi(\rho)}$ .

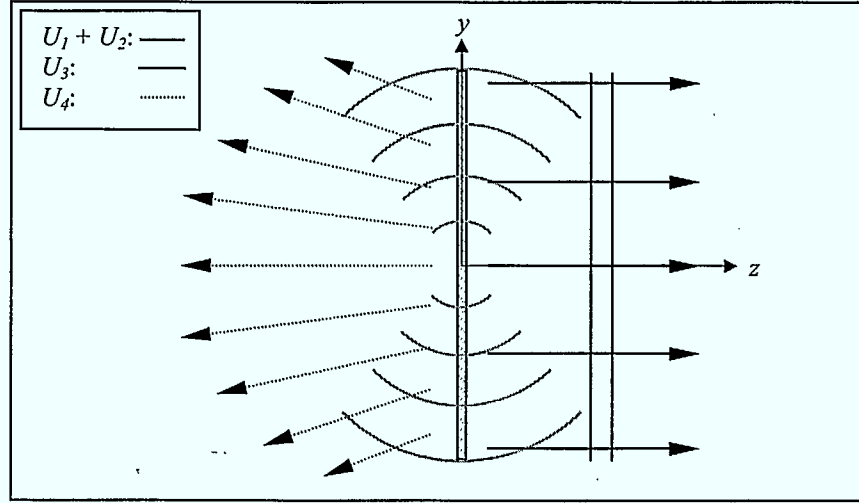


**Figure 2.5. Reconstruction of the four wave components.**

If the above hologram is illuminated by a plane wave instead of a spherical wave, from hologram theory the spherical wave should be reconstructed. This means when recording the hologram, the plane wave is the reference wave, and the spherical wave is the object wave. The interference pattern between these two wavefronts remains unchanged from (2-9), and the reconstructed wave is:

$$\begin{aligned} U_c' &= ae^{j\theta(z)}I, \\ U_c' &= A^2ae^{j\theta(z)} + a^3e^{j\theta(z)} + Aa^2e^{j\phi(\rho)} + Ae^{-j\phi(\rho)}a^2e^{j2\theta(z)}. \end{aligned} \quad (2-12)$$

Again, (2-12) can be broken down into four wave expressions where:

$$\begin{aligned} U_1' &= A^2ae^{j\theta(z)}, \\ U_2' &= a^3e^{j\theta(z)}, \\ U_3' &= Aa^2e^{j\phi(\rho)}, \\ U_4' &= Ae^{-j\phi(\rho)}a^2e^{j2\theta(z)}. \end{aligned} \quad (2-13)$$

The first two wave components now correspond to a plane wave propagating in the positive direction. The third wave is the diverging spherical wave, and finally  $U_4$  is a converging spherical wave multiplied by a linear phase factor.

### 2.2.2 Special case: destructive interference pattern

As mentioned in Section 2.1.1, a hologram is a record of the intensity of interference varying between the maximum and the minimum value. In many applications, such as in the design of Fresnel lenses, a hologram is approximately constructed from the destructive interference pattern since it can easily be reproduced using a perfect conducting material. This destructive pattern corresponds to the case when the intensity  $I$  of the hologram is zero (opaque regions in Figure 2.4). Considering the hologram described in the previous section, and assuming the amplitude of the spherical wave equals the amplitude of plane wave, then (2-9) becomes:

$$\begin{aligned} I &= A^2 + A^2 + A^2 e^{-j\phi(\rho) + j\theta(z_o)} + A^2 e^{j\phi(\rho) - j\theta(z_o)}, \\ I &= 2A^2 [1 + \cos(\phi(\rho) - \theta(z_o))]. \end{aligned} \quad (2-14)$$

When  $I = 0$ ,

$$1 + \cos(\phi(\rho) - \theta(z_o)) = 0, \quad (2-15)$$

and with some simple mathematical manipulations,

$$\phi(\rho) = \pm(2n - 1)\pi + \theta(z_o), \quad (2-16)$$

where  $n = 1, 2, 3, \dots$ . This means the destructive pattern occurs when the reference and the object waves are  $180^\circ$  out of phase. The destructive pattern between a spherical wave generated by a point source at coordinates  $(0, 0, z_o)$  and a plane wave traveling in the positive direction is



plotted in Figure 2.6. Note only the upper  $x$ - $y$  plane region of the recording medium is considered.

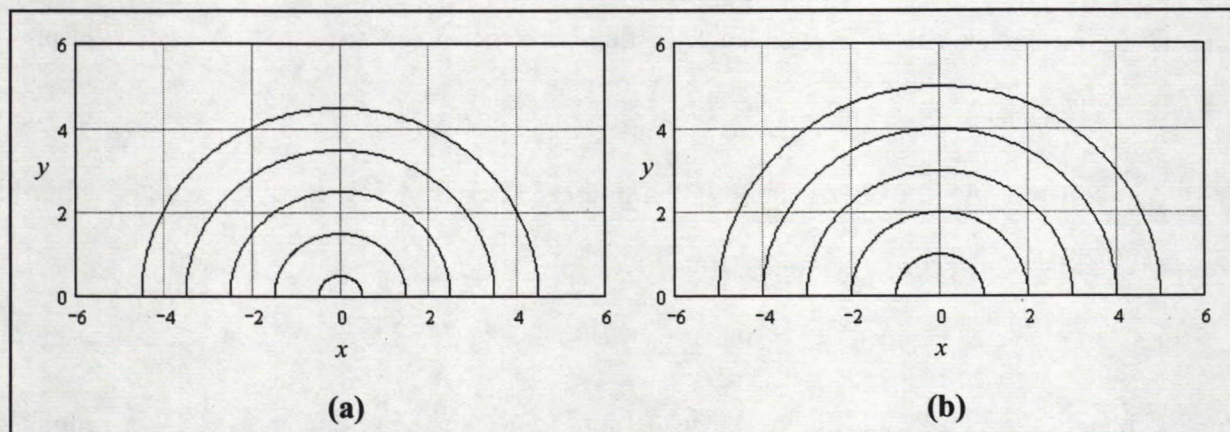


**Figure 2.6. Destructive interference pattern between spherical wave and plane wave for two locations of point source: (a)  $z_o = 0$ , (b)  $z_o = \frac{\lambda_o}{2}$ .**

The two examples illustrated in Figure 2.6 are for when at the recording media (a) the phase of the plane wave is  $0^\circ$  and (b) the phase of the plane wave is  $180^\circ$ , which is shown in Figure 2.7.

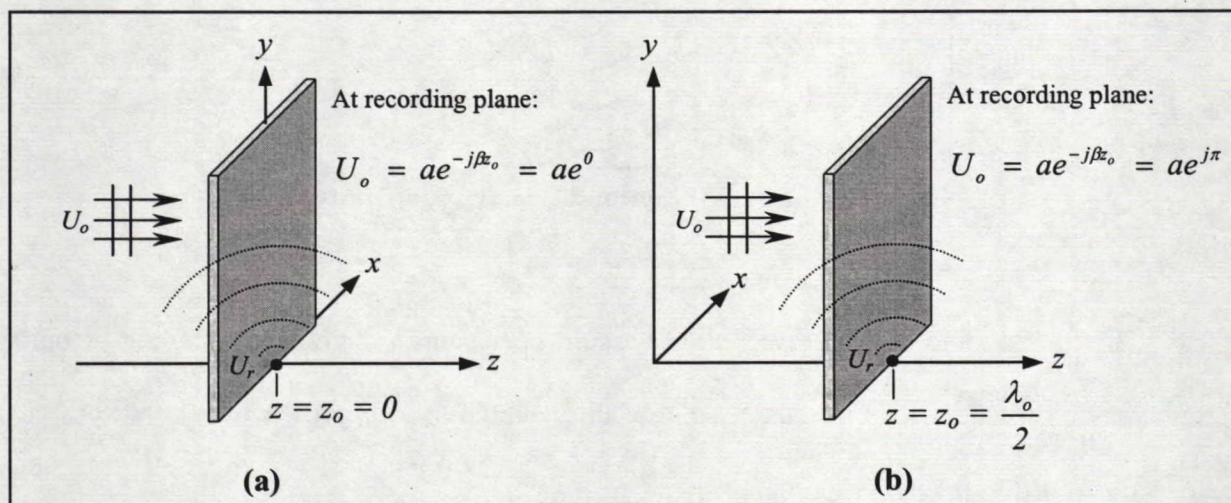


**Figure 2.7. Location of recording medium**

(a)  $z_o = 0$ , (b)  $z_o = \frac{\lambda_o}{2}$ .

Therefore, depending on where the recording media is located, the intensity or the interference pattern will vary. Note that the focal point of the point source is always at  $(0,0,z_o)$ . Also, the distance between each ring in Figure 2.6 is  $\lambda_o$  due to the periodicity of the spherical wavefront.

Reconstructing the hologram by illuminating the recording medium with a spherical wave yields a similar expression to (2-10):

$$U_c = 2A^3 e^{j\phi(\rho)} + A^3 e^{j\theta(z)} + A^3 e^{j2\phi(\rho)} e^{-j\theta(z)}. \quad (2-17)$$

Again, the reconstructed wave can be separated into four wave components which will propagate away from the recording medium in a similar fashion to Figure 2.5, as illustrated in Figure 2.8, where PW\* is the complex conjugate of the plane wave, PW, multiplied by a phase factor.

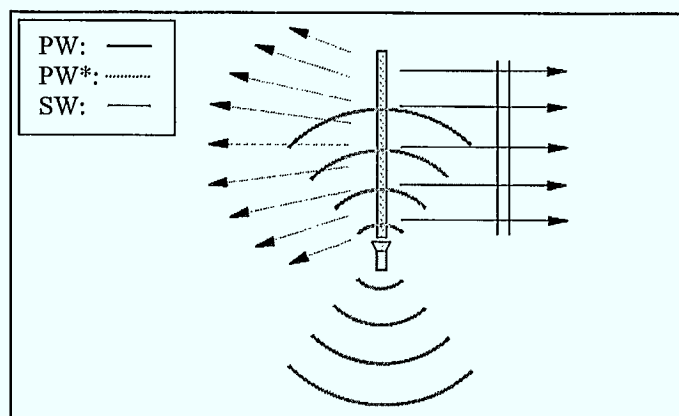


**Figure 2.8. Reconstruction of destructive pattern.**

The holographic review given above assumes that the hologram is recorded at optical frequencies. However, it is possible to apply this technique at microwave frequencies. This issue is discussed in the next section.

## **2.3 Application of Hologram Theory at Microwave Frequencies**

### **2.3.1 Holographic antennas**

As mentioned in Chapter 1, holographic techniques have been applied at microwave frequencies in many areas, such as microwave zoned lenses, coherent side-looking radars, holographic VHF antennas, volume-type holographic antennas, and many others [4-5, 9]. In fact, holography is used in near field systems and in the accurate measurement of electrically large reflector antennas [6-8].

Now, one may wonder how this can be possible since holography techniques are based on optical approximations. Holography is applicable at any frequency range where a coherent source is available [10]. At microwave frequencies, coherence is generally not a problem since microwave sources are usually monochromatic [16-17]. Therefore, a simple microwave feed horn can be used to generate the coherent reference wave, which in this case corresponds to a spherical wave. For hologram construction, the object wave is a plane wave propagating in the desired direction. As seen in the previous sections, if the hologram is illuminated by the reference wave, it generates the object's wavefront, and if illuminated by the object wave, it reproduces the reference's wavefront. Lens and reflector antennas behave in the same manner, that is as a transmitter it transforms a spherical wave to a plane wave, and in the receiving mode it transforms the plane wave into a spherical wave. The hologram, when illuminated by the feed horn (reference wave), produces a plane wave, or in terms of antenna parameters, a radiation pattern. Therefore, like an antenna, the hologram is a transmitter and a receiver (reciprocal).



The most attractive feature of holographic antennas is its instructive nature which allows visualization of the possible antenna configurations from the interference pattern of the desired generated radiation pattern (or object wave). However, application of holography techniques at microwave frequencies does not come without drawbacks. At microwave frequencies there is no practical equivalent to an optic recording film other than liquid crystal, which requires strong field intensities ( $1mW$  per square inch [4] or  $10mW/cm^2$  [18]) and is therefore impractical. Thus, in order to create a simple microwave hologram, approximations must be made such as the destructive pattern shown in Figure 2.6. Due to this approximation the hologram will suffer from phase errors and the resolution (related to efficiency) of the reconstructed wave will be poor. A last important point to mention is the effect of using a finite sized hologram. Ideally, to accurately reproduce an object wavefront, an infinite hologram (or recording medium) is necessary, otherwise some information is lost and the efficiency is reduced. In terms of the antenna, a finite size means a reduction in gain and implies some spillover problems which have to be controlled by proper illumination of the antenna's surface. Nevertheless, all these factors can be overcome and proper holographic antennas can still be designed. A specific case of such an antenna is described in the next section.

### **2.3.2 Specific case of a holographic antenna**

The antennas considered in this thesis are based on the holographic antenna designed in the 70's by Iizuka *et al.* [5]. The general idea is to reproduce the interference pattern between a spherical wave and a plane wave and then illuminate this hologram with a feed horn. As mentioned before, the easiest pattern to reproduce is the destructive one illustrated in Figure 2.6. However, this will create an approximated hologram. From the discussion in Section 2.2.2, the

intensity  $I$  is zero when the spherical wave and the plane wave are  $180^\circ$  out of phase, which means on the recording medium:

$$\vec{E}_{SW} + \vec{E}_{PW} = 0, \quad (2-18)$$

where  $\vec{E}_{SW}$  is the electric field component of the spherical wave and  $\vec{E}_{PW}$  is the electric field component of the plane wave. The tangential electric field component is known to be zero on an electric wall or a perfect conductor. Therefore, the destructive interference pattern between two waves can be reproduced by placing conducting strips where the intensity of the hologram is zero. These conducting strips can be etched onto a thin dielectric slab, which ideally would have a dielectric constant close to that of air. Note that the resulting antenna structure has no ground plane.

As mentioned before, the polarisation of the object wave generated by the holographic antenna is equal to the reference spherical wave's polarisation, which in this case is linear. Not only does this choice simplify the mathematical expressions, but it also allows the antenna to intercept and transmit maximum power. The polarisation of both waves is shown in Figure 2.9, for the case where the destructive interference pattern hologram described in Section 2.2.2 is illuminated by a spherical wave.

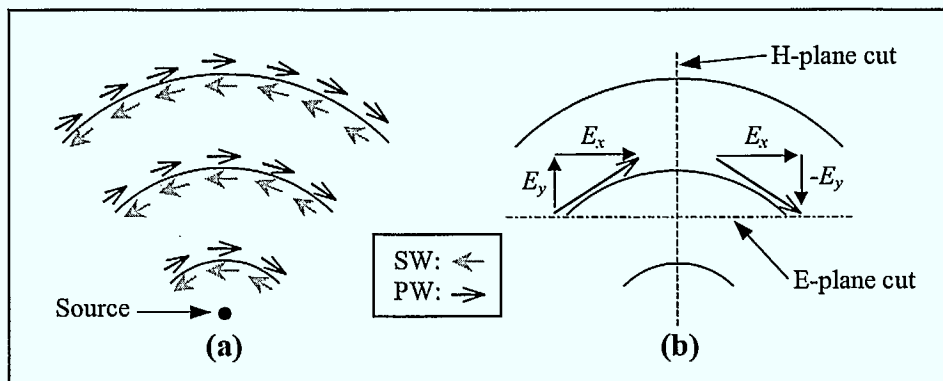


**Figure 2.9. Generation of the plane wave**  
(a) Polarisation (b) Decomposition.

Notice from Figure 2.9 (b) that the plane wave has both horizontal and vertical field components. The antenna's layout can be chosen to favor the horizontal polarization by simply cutting out from the destructive pattern the regions where the vertical component is predominant as shown by the dotted lines in Figure 2.10. Most of the conducting rings inside the dotted boundary have a larger horizontal field component than a vertical one, and this "diamond" shaped hologram should help to reduce the cross-polarization level.

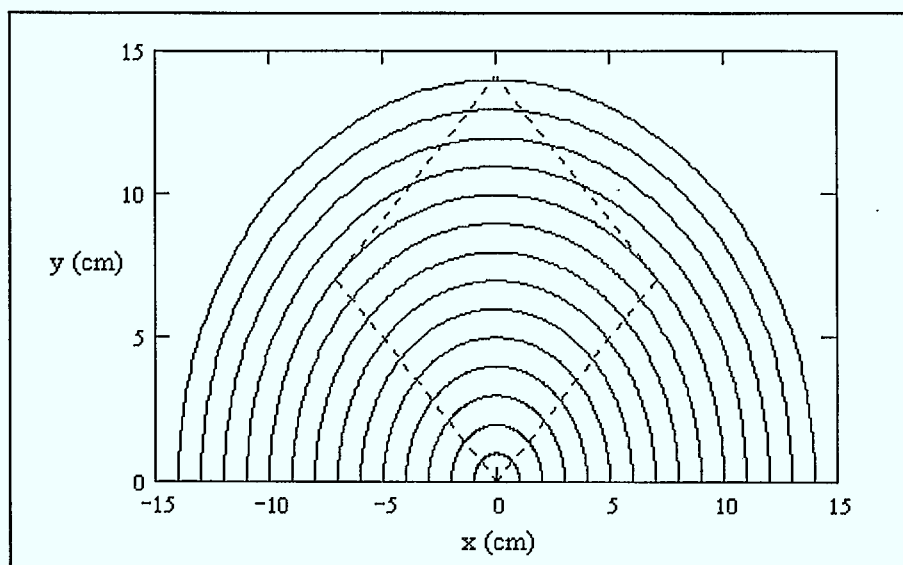


**Figure 2.10. Holographic antenna's layout (area enclosed by dotted lines).**

Based on Figure 2.9, in the H-plane cut the cross-polarization level should be zero at broadside since the vertical field components on the right and left side of the antenna cancel each other out. In the E-plane however, the cross-polarization level will be higher due to the non-symmetry of the antenna. Note that the feed is located at coordinates  $(0,0,z_o)$  where the recording medium is the  $z = z_o$  plane.



From the reconstruction process described in Section 2.2.1 and in Figure 2.9 (a), it is now possible to identify how the beams are formed and what the far-field radiation pattern will look like. Based on the hologram concept, four beams are expected with beam peaks  $90^\circ$  apart from each other. An alternative way to predict the behavior of the antenna is by considering the scattering which occurs when the spherical wave is incident on the conducting strip as shown in Figure 2.11.

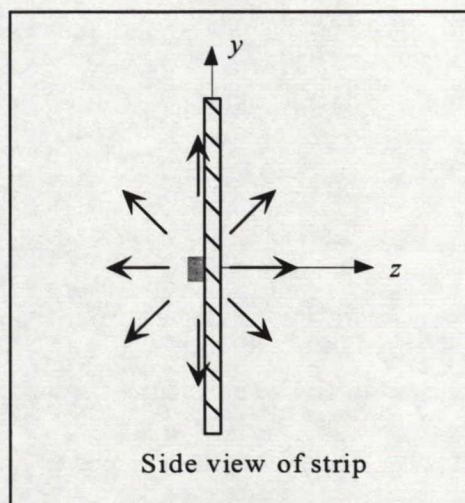


**Figure 2.11. Scattering introduced by single strip.**

With an array of strips separated by a distance of  $d = \lambda_o$ , it can be deduced that the far-field radiation pattern should contain four beams as shown in Figure 2.12. A more detailed treatment of the radiation pattern is given in Chapter 3.

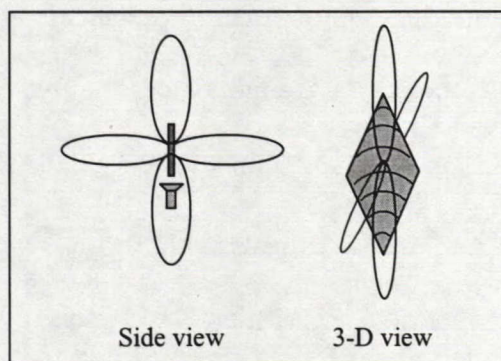


**Figure 2.12. Predicted far-field radiation pattern.**

Note that in order for the hologram to effectively transform the energy from the spherical wave, the feed has to be at the proper focal point. Otherwise, when the spherical wave's rings reach the conducting strips, they will not have the same radii as the strips and only a portion of the wave will be properly reflected. In other words, if the focal point is not respected, the phase of the spherical wave at a point where the interference pattern should be zero will not be  $180^\circ$  out of phase with the phase of the plane wave. The focal point is an important feature of the holographic antenna and should not be neglected. Other approximations, to be considered in the following section, may be applied and the hologram will still operate as an antenna.

### 2.3.3 General approximations

Many approximations are made in the design of the holographic antenna. First it is assumed that the feed horn behaves in the same manner as an ideal point source with constant current, i.e. that the feed generates a perfect spherical wave. A second approximation is that coupling between the conducting strips is non-existent. The presence of coupling, however, will not affect the vanishing tangential electric field component requirement for the hologram construction.

The final and most important approximation pertains to the guided wavelength. At the moment, it is assumed that the guided wavelength equals the free-space wavelength even though the holographic strips are supported by a thin dielectric layer. The effect of using  $\lambda_0$  is discussed in the next chapter, which also deals with various ways of looking at holographic antennas and validates the hologram theory at microwave frequencies.

## CHAPTER 3

### Microwave Analysis of Holograms

Even though holography helps to visualize the antenna's layout and the reconstructed waves' behavior, it does not completely cover all the issues present at microwave frequencies, such as the effect of the dielectric, the guided wavelength, the far-field radiation pattern, the beam scan, and many others. This chapters deals with these factors by treating the holographic antenna as an array and a periodic structure. The expressions for the guided wavelength are also evaluated using well-known methods such as surface wave analysis and array theory.

#### 3.1 Array Theory

##### 3.1.1 General review

Consider a linear array of  $N$  elements equally spaced by a distance  $d$  as shown in Figure 3.1. Assuming that the elements are identical with equal magnitude and a progressive phase,  $\beta_p$ , excitation, the array is called a uniform array [19].

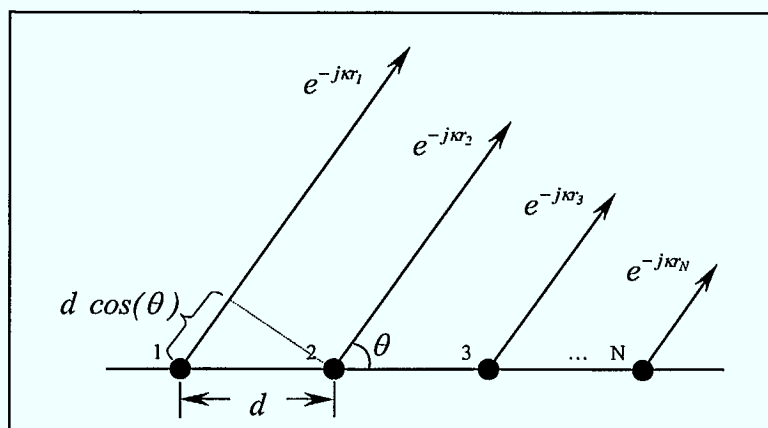


Figure 3.1. Uniform array.

The array pattern ( $\bar{A}$ ) can now be written as the element pattern ( $\bar{E}$ ) multiplied by the array factor ( $AF$ ) which is expressed mathematically as:

$$\bar{A} = \bar{E}(AF) = [\bar{E}] [e^{-j\kappa r_1} + e^{-j\kappa r_2} + e^{-j\kappa r_3} + \dots + e^{-j\kappa r_N}]. \quad (3-1)$$

In the far field (refer to [19, Chapter 6] for complete details),  $r_n$  can be approximated as:

$$\begin{aligned} r_l &= r_n + (n-1) d \cos(\theta), \\ r_n &= r_l - (n-1) d \cos(\theta), \end{aligned} \quad (3-2)$$

where  $n = 1, 2, 3, \dots, N$ , and  $N$  is the number of elements in the array. Substituting (3-2) into (3-1), the array pattern ( $\bar{A}$ ) becomes:

$$\begin{aligned} \bar{A} &= [\bar{E}] [e^{-j\kappa r_1} + e^{-j\kappa[r_1 - d \cos(\theta)]} + e^{-j\kappa[r_1 - 2d \cos(\theta)]} + \dots + e^{-j\kappa[r_1 - (N-1)d \cos(\theta)]}], \\ \bar{A} &= \bar{E} e^{-j\kappa r_1} \sum_{n=1}^N e^{j\kappa(n-1)d \cos(\theta)} = \bar{E} e^{-j\kappa r_1} (AF), \end{aligned} \quad (3-3)$$

where  $\kappa$  is the wave number ( $\kappa = \frac{2\pi}{\lambda}$ ). The array factor ( $AF$ ) is given by:

$$AF = \sum_{n=1}^N e^{j(n-1)[\kappa d \cos(\theta) + \beta_p]} = \sum_{n=1}^N e^{j(n-1)\frac{\psi}{2}} = e^{j(N-1)\frac{\psi}{2}} \left[ \frac{\sin\left(\frac{N}{2}\psi\right)}{\sin\left(\frac{1}{2}\psi\right)} \right], \quad (3-4)$$

and  $\psi = \kappa d \cos(\theta) + \beta_p$ .

In order to obtain a maximum radiation broadside ( $\theta = 90^\circ$ ),  $\beta_p$  must be equal to zero and  $\psi = \kappa d \cos(\theta)$ . Also, it is important to note that for an array where the elements are spaced by  $d = \lambda$  and  $\beta_p = 0$ , the array factor will have two main lobes at  $\pm 90^\circ$  and one at  $0^\circ$  and  $180^\circ$ . In most cases, this type of array is not considered since only one main beam is desired.



In many applications, it is often required to scan the beam to another location off broadside. This implies having a maximum radiation at  $\theta = \theta_s$ , where  $0^\circ \leq \theta_s \leq 180^\circ$ . Maximum radiation occurs when  $\psi = \kappa d \cos(\theta_s) + \beta_p = 0$  which simplifies to:

$$\beta_p = -\kappa d \cos(\theta_s). \quad (3-5)$$

The phase excitation of each element is therefore:

$$\alpha_n = -(n - 1)\kappa d \cos(\theta_s) = (n - 1)\beta_p, \quad (3-6)$$

which is a useful expression when the distance  $d$  and  $\theta_s$  are known.

The holographic antenna described in the previous chapter can be defined as an array where each conductor strip is treated as a single element. For the specific case considered in Chapter 2, the number of elements  $N$  corresponds to 14. The analogy of the hologram to the linear array is an approximation because the elements in the holographic antenna are different from each other. Nevertheless it is still possible to evaluate the phase on the individual element of the hologram using array theory since the rings are spaced equally.

### 3.1.2 Beam scan versus frequency and the guided wavelength

Because of the feeding technique, the holographic antenna can be viewed as a traveling wave antenna where radiation occurs due to scattering at each conducting strip. As the wave of the point source progresses from one element to another in the array, the phase on each of them can be determined. For the special case where  $d = \lambda_o$  (see Section 2.2.2), and at the desired frequency  $f_o$ , the phase on each conducting strip is the same ( $\beta_p = 2\pi = 0$ ) and maximum radiation occurs at broadside. At other frequencies however, a beam scan will occur due to a



phase delay  $\Delta\phi$  introduced by  $\Delta d$  as shown in Figure 3.2. Assuming that the phase of the first element is zero, when the spherical wavefront reaches the second element, the phase is  $2\pi \pm \Delta\phi$  depending whether  $f_1 \leq f_o$  or  $f_1 \geq f_o$ . The beam scan induced by this phase delay can be determined by evaluating the phase difference at the second element when  $\lambda = \lambda_o$  and  $\lambda = \lambda_1$ .

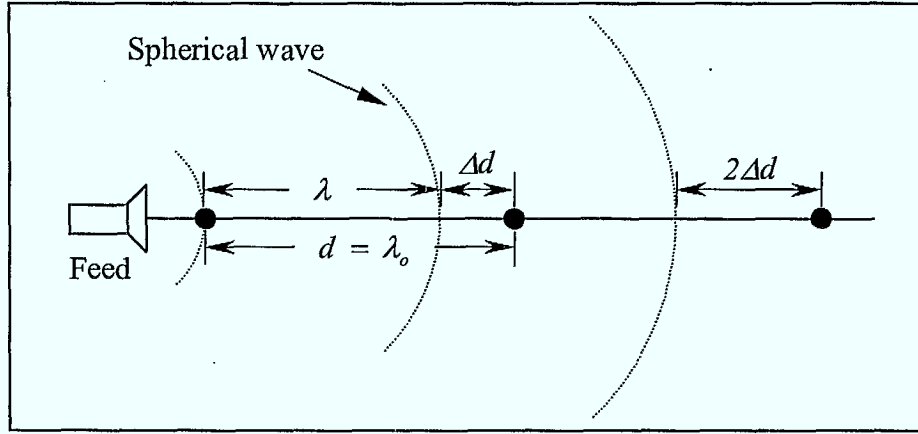


**Figure 3.2. Phase delay at frequency  $f$ .**

From the above statement, the phase on the second element at two different frequencies is:

$$\phi_o = -\frac{2\pi}{\lambda_o} d, \quad (3-7)$$

and,

$$\phi_1 = -\frac{2\pi}{\lambda_1} d. \quad (3-8)$$

Taking the phase difference (knowing that  $\phi_1 = \phi_o + \Delta\phi$ ) and substituting  $d$  by  $\lambda_o$  then:

$$\Delta\phi = \phi_1 - \phi_o = -\frac{2\pi}{\lambda_1} \lambda_o + \frac{2\pi}{\lambda_o} \lambda_o = 2\pi \left[ \frac{\lambda_1 - \lambda_o}{\lambda_1} \right] = \beta_p. \quad (3-9)$$

From the previous section,  $\beta_p = -\kappa_1 d \cos(\theta_s)$ , where  $\kappa_1 = \frac{2\pi}{\lambda_1}$ , and manipulating the

equations the beam scan angle is:

$$\theta_s = \arccos \left[ \frac{\lambda_o - \lambda_l}{\lambda_o} \right]. \quad (3-10)$$

It is evident from (3-10) that as the frequency changes, the beam peak value changes as well. Note that for  $f_l \leq f_o$  the beam will scan in the negative direction (towards the feed) and for  $f_l \geq f_o$  it will scan in the positive direction (away from the feed).

In general, the beam scan would be considered an undesirable feature. However, if the scan is small enough then it is still acceptable within a 10% bandwidth to meet the 3dB beamwidth specification. For example, let's define a 10% bandwidth where  $f_l \leq f_o \leq f_2$  and:

$$\begin{aligned} f_l &= 0.95 f_o, \\ f_2 &= 1.05 f_o. \end{aligned} \quad (3-11)$$

The free-space wavelength is thus:

$$\begin{aligned} \lambda_l &= \frac{c}{f_l} = \frac{c}{0.95 f_o} = \frac{\lambda_o}{0.95}, \\ \lambda_2 &= \frac{c}{f_2} = \frac{c}{1.05 f_o} = \frac{\lambda_o}{1.05}. \end{aligned} \quad (3-12)$$

Substitute (3-12) into (3-10), the beam peak value at both frequencies becomes:

$$\begin{aligned} \theta_l &= \arccos \left[ \frac{\lambda_o - \lambda_l}{\lambda_o} \right] = \arccos \left( 1 - \frac{1}{0.95} \right) \approx 93.02^\circ, \\ \theta_2 &= \arccos \left[ \frac{\lambda_o - \lambda_2}{\lambda_o} \right] = \arccos \left( 1 - \frac{1}{1.05} \right) \approx 87.27^\circ. \end{aligned} \quad (3-13)$$

Therefore, in a 10% bandwidth, the beam scans by approximately  $5.75^\circ$ , which means for an antenna pattern with a beamwidth greater than  $6^\circ$ , most of the power can still be captured in the entire desired frequency range assuming the beamwidth does not change with frequency as the beam scans.

Up to this point, the discussion has been confined mainly to radiating elements located in free space. The spacing  $d$  is thus evaluated in terms of the free-space wavelength. In practice, however, arrays of conducting strips are usually fabricated on printed circuit substrates which can affect the wave propagation velocity. Therefore, if a dielectric-substrate antenna is designed with the free-space wavelength in mind, one should expect a beam scan at the center frequency  $f_o$ . It is possible from (3-9) and  $\beta_p = -\kappa_o d \cos(\theta_s)$ , where  $\kappa_o = \frac{2\pi}{\lambda_o}$ , to evaluate the guided wavelength ( $\lambda_g$ ) at the desired frequency such that the beam peak is broadside ( $\theta_s = 90^\circ$ ). Basically, from the beam scan angle obtained at frequency  $f_o$ , the above equations evaluate the phase delay introduced by  $\Delta d$  for the case when  $\lambda = \lambda_g$  in Figure 3.2. Therefore, for a beam peak of  $\theta_s$  at  $f_o$  the guided wavelength is:

$$\lambda_g = \frac{\lambda_o}{1 + \cos(\theta_s)}, \quad (3-14)$$

where the beam peak,  $\theta_s$ , is measured experimentally.

In this thesis only broadside radiation is of interest. However, it is possible to generate the beam at another angle off broadside by simply varying the distance  $d$ , which is one of the attractive features of the holographic antenna since no complicated feed structures are required. Note that the spacing between elements can also be predicted by observing the destructive interference pattern between a spherical wave and an obliquely incident plane wave onto the recording medium. However, one must be careful since hologram theory will provide  $d$  with respect to  $\lambda_o$ . Nevertheless, this approximation ( $\lambda_g \approx \lambda_o$ ) is good enough for the validation of

holographic principles at microwave frequencies and simplifies the calculation of the antenna far-field pattern described in the next section.

### 3.1.3 Far-field radiation pattern

As discussed before, the holographic theory of the previous chapter can predict accurately the direction of the main beam. However, it does not provide a detailed description of the far-field radiation pattern. This can be done by applying the array theory just described. From array theory, it is possible to treat each ring of the holographic antenna as a loop antenna and from the general expression derived in [19], evaluate the radiation pattern of an array of loop antennas.

Assuming the conducting strips can be approximated by circular loops of uniform current  $I_\phi = I_o$ , from [19, p. 165] and Figure 3.3, the potential function  $\vec{A}$  for a single loop is:

$$\vec{A}(x, y, z) = \frac{\mu}{4\pi} \oint_C \vec{I}_e(x', y', z') \frac{e^{-jkR}}{R} dl' . \quad (3-15)$$

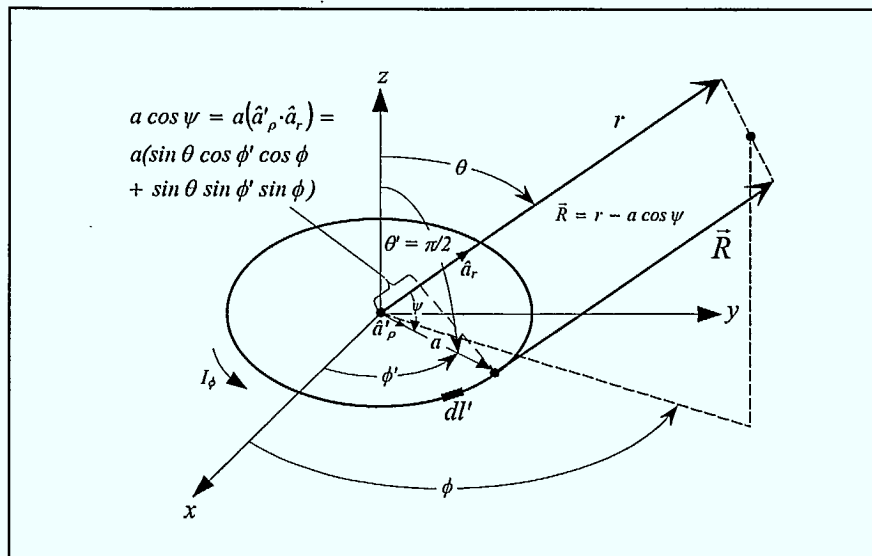


Figure 3.3. Geometry for far-field observation [19].

From the above figure, the primed coordinates represent the source, while the unprimed the observation point. The vector  $\vec{R}$  corresponds to the distance from any point on the loop to the observation point and  $dl'$  is defined as an infinitesimal section of the loop antenna ( $dl' = ad\phi'$ ). In cylindrical coordinates, the distance  $\vec{R}$  can be expressed as:

$$\vec{R} = \sqrt{r^2 + a^2 - 2ar \sin(\theta) \cos(\phi - \phi')}, \quad (3-16)$$

which in the far-field ( $r \gg a$ ) reduces to:

$$\vec{R} \approx \sqrt{r^2 - 2ar \sin(\theta) \cos(\phi - \phi')}. \quad (3-17)$$

Equation (3-17) can be simplified, using the binomial expansion, to:

$$\begin{aligned} R &\approx r - a \sin(\theta) \cos(\phi - \phi') \text{ for phase terms,} \\ R &\approx r \text{ for amplitude terms.} \end{aligned} \quad (3-18)$$

Also in cylindrical coordinates, the current  $\vec{I}_e$  is only flowing in the  $\phi$  direction. Therefore, a good assumption for a thin conducting loop is:

$$\vec{I}_e = \hat{a}_\phi I_\phi \cos(\phi - \phi'). \quad (3-19)$$

Usually, since the current  $I_\phi$  is a constant, the field radiated by the loop will not be a function of the observation angle  $\phi$ . Therefore any observation angle can be selected. However, this applies only to the case where a full loop is considered. For the holographic antenna case, only a section of the loop is analyzed and the observation angle must be chosen depending on the cut of interest. From Figure 3.4, the desired observation angle is  $\phi = 0$  (H-plane cut) and the limits of the integral become  $-\frac{\phi_a}{2}$  to  $\frac{\phi_a}{2}$ . Using (3-18) and (3-19), the potential function simplifies to:

$$A_\phi = \frac{a\mu I_o}{4\pi r} e^{-jkr} \int_{-\frac{\phi_a}{2}}^{\frac{\phi_a}{2}} \cos(\phi') e^{jka \sin(\theta) \cos(\phi')} d\phi'. \quad (3-20)$$

The electric and magnetic fields associated with the above vector potential can now be determined. From [19, Chapter 3], the far-field field expressions are:

$$\begin{aligned}
 E_r &= E_\theta \approx 0, \\
 E_\phi &= -j\omega A_\phi = -j\omega \left[ \frac{a\mu I_o}{4\pi r} \right] e^{-jk r} \int_{-\frac{\phi_a}{2}}^{\frac{\phi_a}{2}} \cos(\phi') e^{jk a \sin(\theta) \cos(\phi')} d\phi', \\
 H_r &= H_\phi \approx 0, \\
 H_\theta &= \frac{E_\phi}{\eta} = j \frac{\omega}{\eta} \left[ \frac{a\mu I_o}{4\pi r} \right] e^{-jk r} \int_{-\frac{\phi_a}{2}}^{\frac{\phi_a}{2}} \cos(\phi') e^{jk a \sin(\theta) \cos(\phi')} d\phi'.
 \end{aligned} \tag{3-21}$$

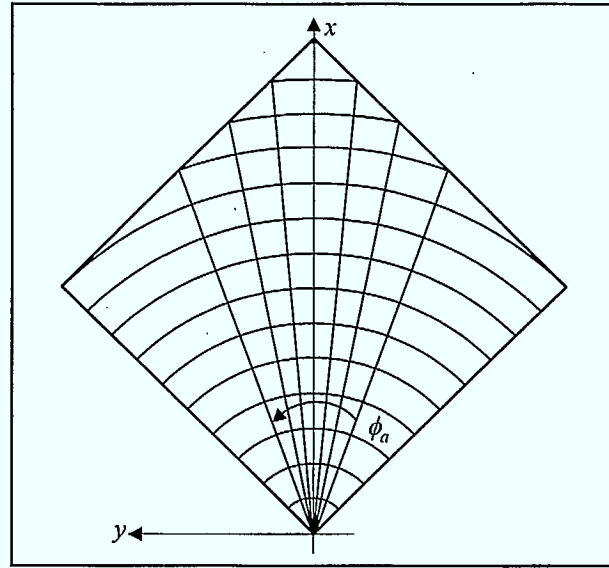


Figure 3.4. Array of loop antennas.

The radiation intensity can be derived based on the time-average power density from [19, p. 178] which is:

$$U = \frac{(a\omega\mu)^2 |I_o|^2}{32\eta\pi^2} \left| \int_{-\frac{\phi_a}{2}}^{\frac{\phi_a}{2}} \cos(\phi') e^{jk a \sin(\theta) \cos(\phi')} d\phi' \right|^2. \tag{3-22}$$

Since (3-22) corresponds to the radiation pattern of a single loop of radius  $a$ , it is necessary to expand this expression such that it takes into account all the loops in the array. The array is simply circular arcs of different radius all centered at the same coordinate. Therefore the radiation intensity becomes:

$$U = \frac{(a\omega\mu)^2 |I_o|^2}{32\eta\pi^2} \left| \sum_{n=1}^N n \int_{\frac{\phi_{a_n}}{2}}^{\frac{\phi_{a_n}}{2}} \cos(\phi') e^{j\kappa n a \sin(\theta) \cos(\phi')} d\phi' \right|^2, \quad (3-23)$$

where  $N$  is the total number of arcs in the array and the  $n^{\text{th}}$  loop has a radius  $a_n = na$ . Equation (3-23) was solved numerically with Mathcad® [20] and the normalized radiation pattern for the holographic antenna with  $N = 14$  and  $\lambda_o = 1\text{cm}$  ( $f_o = 30\text{GHz}$ ), is shown in Figure 3.5. The angular values  $\phi_{a_n}$  for each circular arc along with its respective radius are listed in Table 3.1.

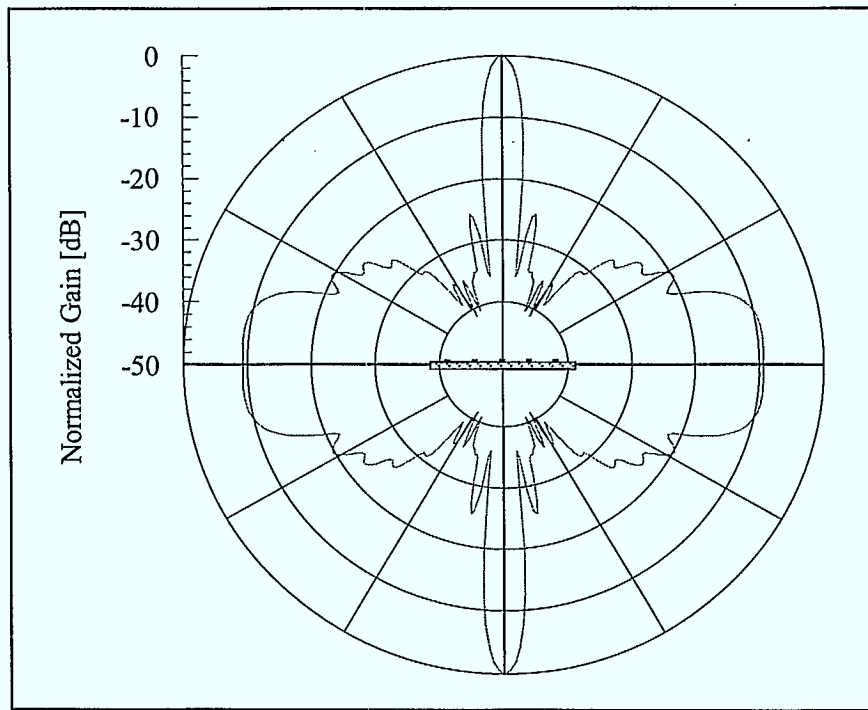


Figure 3.5. Normalized radiation pattern of holographic antenna approximated by an array of circular arcs.

Table 3.1 Characteristics of circular arcs in array

Loop [ $n$ ]	Radius $a$ [cm]	$\phi_{a_n}$ [degrees]
1-10	1-10	90.00°
11	11	40.76°
12	12	22.89°
13	13	10.57°
14	14	1.17°

As predicted from hologram theory, the radiation pattern of the holographic antenna has four beams where the beam peaks are  $90^\circ$  apart. This radiation pattern is useful in the validation of the holographic antenna realized from conducting strip arrays. It will also be compared to another approximation: the dipole hologram which is discussed in the next section.

### 3.1.4 Dipole hologram

A more effective way to construct a hologram, in terms of reducing the cross-polarization level, is to replace the continuous strips by an array of horizontally polarized free-space dipoles. From Figure 3.6, when the spherical wave hits the dipoles, only the horizontal field component is reflected which was not the case with the continuous strips of Figure 2.9, in Chapter 2, where both field components are reflected. Because of the gaps between the elements, one should expect that the dipole hologram will produce less gain in comparison to the continuous-strip case analyzed in the previous section. However, by increasing the number of dipoles, gain reduction will be minimized.

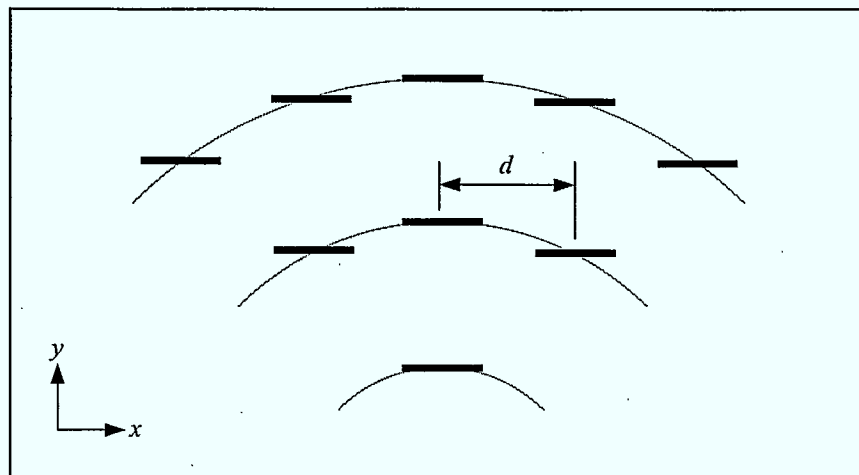
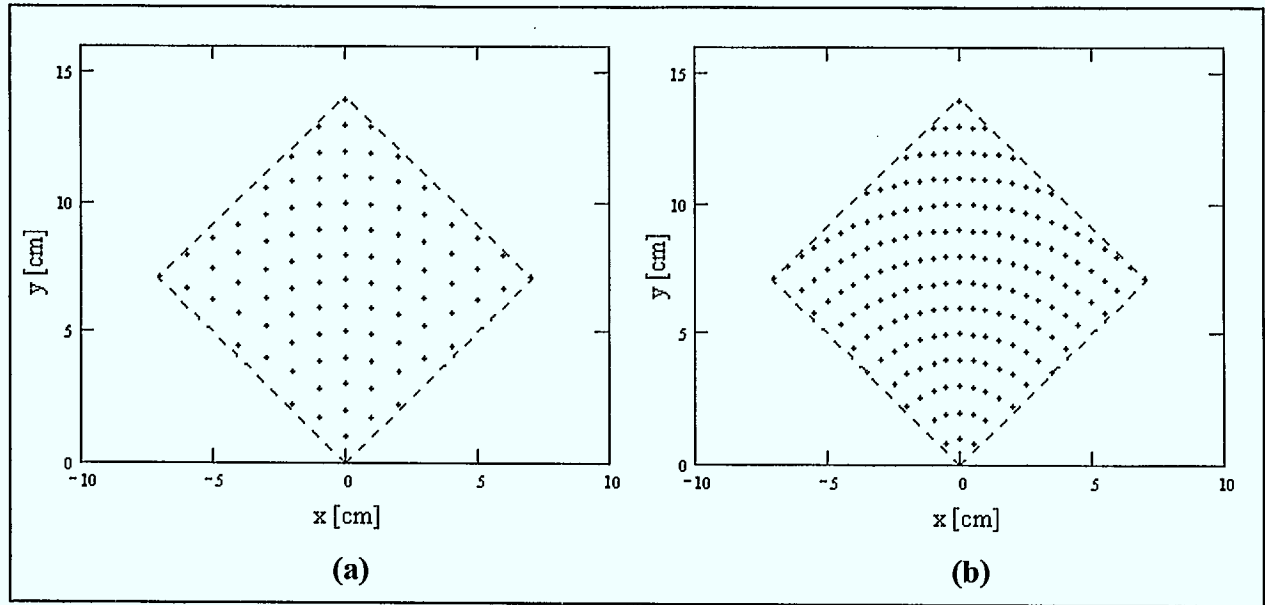


Figure 3.6. Dipole holographic antenna.



Other than reducing the cross-polarization level, the dipole hologram can be used to overlay two holograms on the same plane in order to obtain a dual-polarized, a circular-polarized, or a multi-beam antenna. Array theory can be directly applied to a dipole hologram to predict the far-field radiation pattern of the holographic antenna. As a first order approximation, the dipoles are selected to be half a wavelength long. Half-wave dipoles are known for their convenient current distribution and their efficient scattering qualities. Shorter dipoles can be used but more elements are required to properly model the hologram. Two cases of dipole holograms are considered, as shown in Figure 3.7, where the locations of the free-space dipoles are represented as little crosses.



**Figure 3.7. Dipole Hologram**

(a)  $d = \lambda_o$  (b)  $d = \frac{\lambda_o}{2}$ .

In the first dipole hologram, the spacing  $d$  between each element is selected to be  $\lambda_o$  such that mutual coupling is reduced. Also, it is known from the array concept of periodic grids that no grating lobe appears in free-space for an element spacing of  $d \leq \lambda_o$ . However, this antenna

might not capture enough energy from the feed illumination due to the large gaps between the elements, which explains the second design where  $d = \frac{\lambda_o}{2}$ .

These two antenna arrays were simulated using **ARPS** (Antenna Radiation Patterns Software) [21], and the H-plane radiation patterns are shown in Figure 3.8. Note that **ARPS** neglects mutual coupling between the elements and for this specific case all the elements have an equal amplitude and phase excitation. The radiation pattern of the array of loops (or arc array) from Figure 3.5 is also included in the figure for comparison.

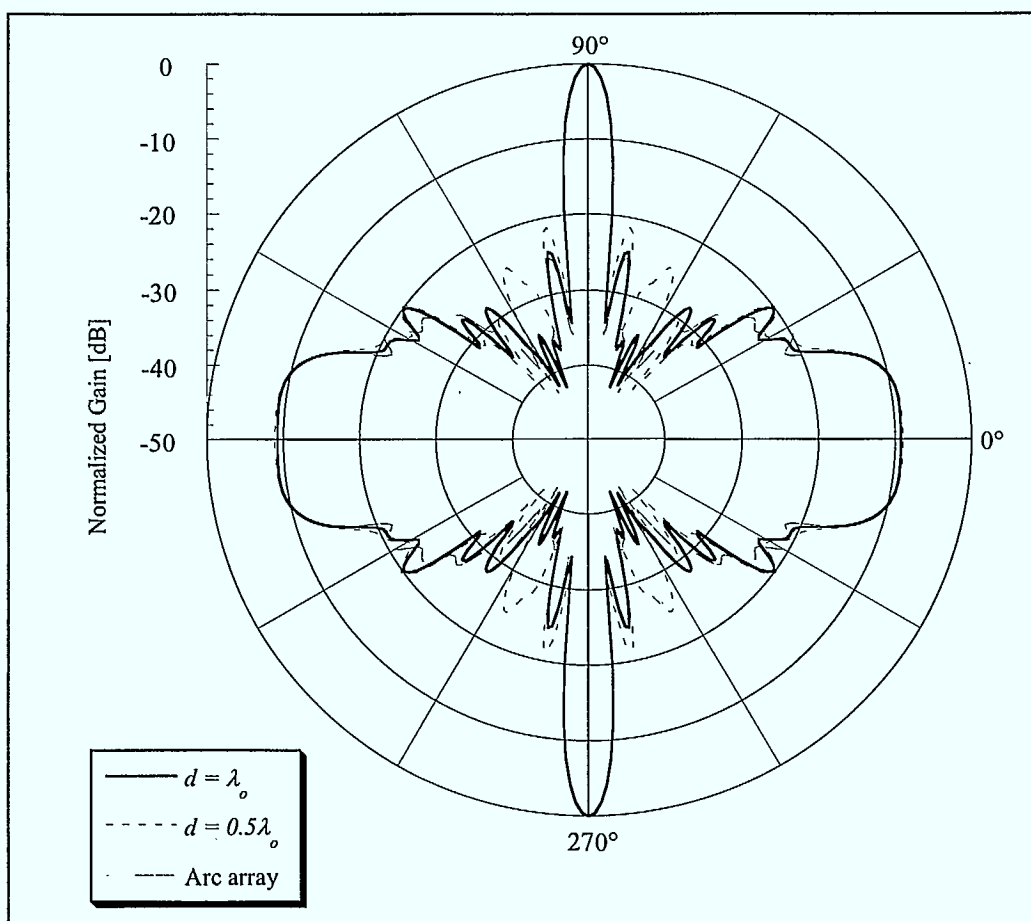


**Figure 3.8. H-plane normalized radiation pattern of holographic antenna approximated by an array of free-space dipoles.**

All three patterns are almost identical except for some of the side lobe levels. The beamwidths of the patterns are less than  $5.5^\circ$  which means, from the discussion in Section 3.1.2, that the 10% bandwidth may not be achieved. The E-plane radiation pattern for both dipole cases are shown in Figure 3.9.

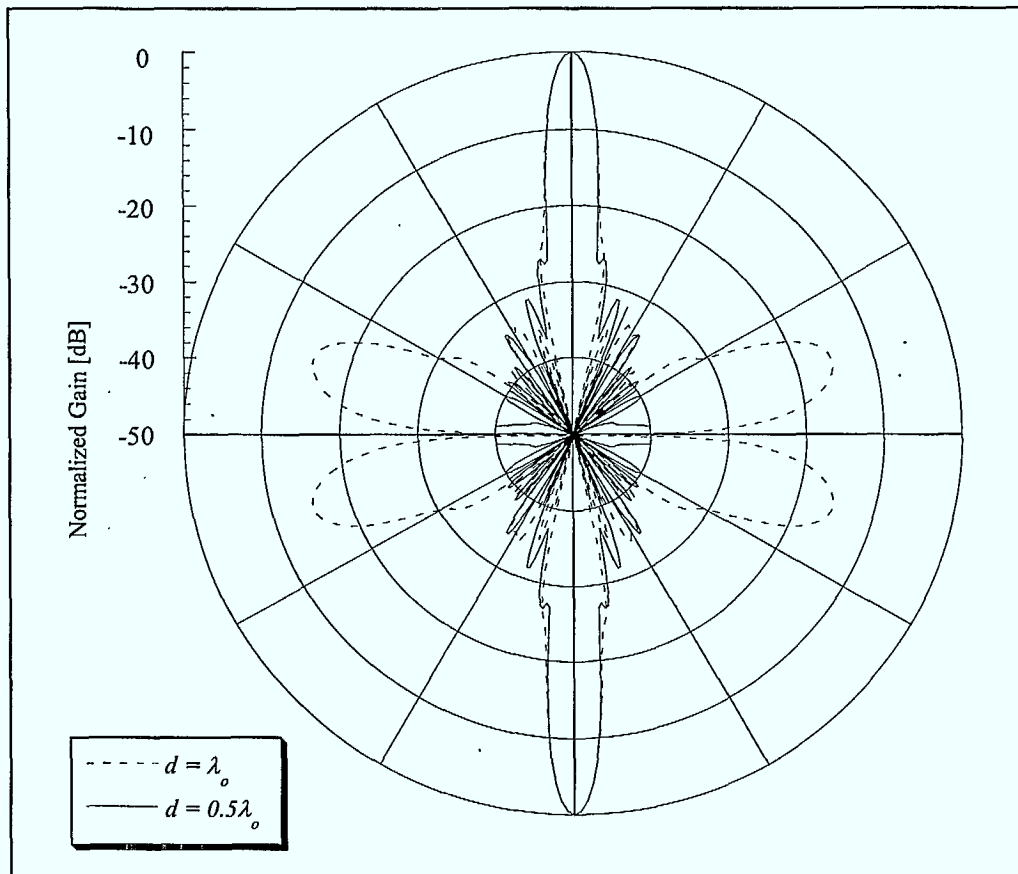


**Figure 3.9. E-plane normalized radiation pattern of holographic antenna approximated by an array of free-space dipoles.**

In the above patterns, if directivity were plotted instead of the normalized gain, the directivity of the dipole holograms would probably be less compared to that of the loop array due to the gaps in the antenna. Nevertheless, both the loop array and dipole array analysis methods agree with each other and provide a good indication of what the radiation pattern should look like. The patterns in Figure 3.8 also point out an important issue about the hologram: three



undesired side lobes are present in the far-field radiation pattern. It is possible, using array techniques, to eliminate some of these side lobes. This topic is discussed in the next section.

### 3.1.5 Two-layer hologram

It is possible using an array of holograms to eliminate the lobe at  $270^\circ$  (referred to as the back lobe) and the side lobe returning towards the feed (one of the two lobes at  $0^\circ$  and  $180^\circ$ ) when referring to Figure 3.8. The general idea is to combine the fields of the two holograms such that they add up in the main lobe (or front lobe) and cancel in the back lobe. This means that a gain increase of at least  $3dB$  should be obtained. As for the side lobe returning towards the feed, the cancellation can significantly improve the feed return loss. To accomplish this task, an array of two properly phased holograms such as in [5] and illustrated in Figure 3.10 is considered.

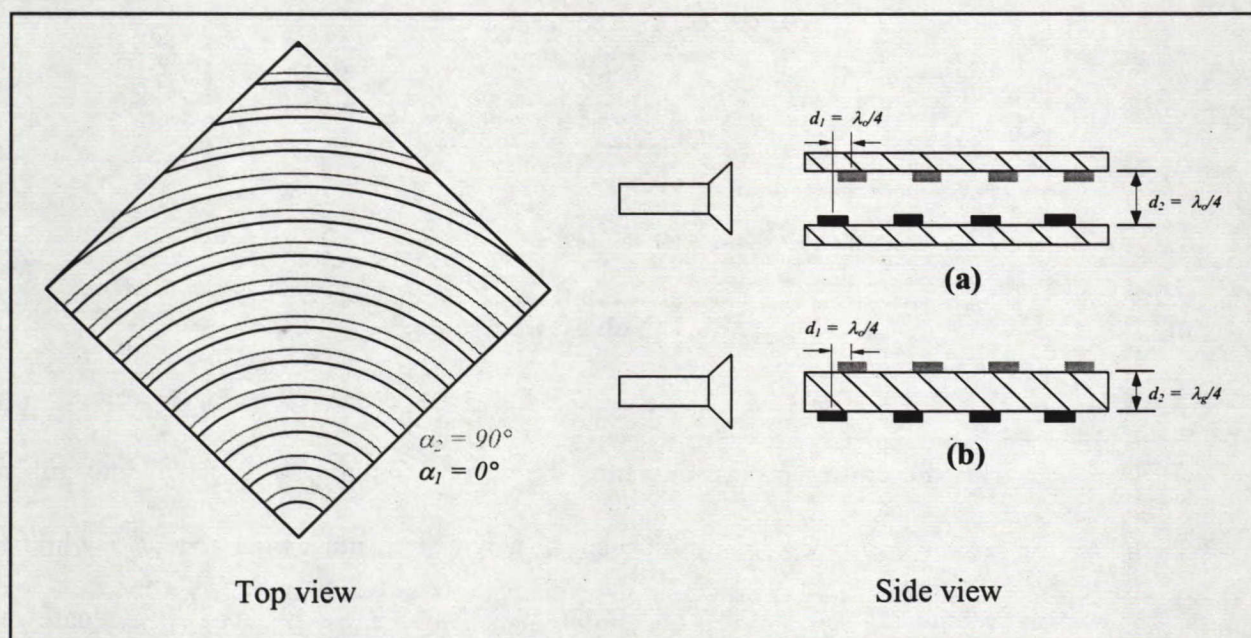


**Figure 3.10. Two-layer hologram**  
**(a) Two-plate hologram (b) Double-sided hologram.**



The first design (case (a) in the above figure) corresponds to two holograms etched on different substrates spaced by  $d_2$  in free space. The second case consists of the same two holograms but this time etched onto a single substrate of dielectric constant  $\epsilon_r$ . The top view shows that the two holograms are separated from each other with respect to the feed such that their relative phase  $\beta_p$  is  $90^\circ$ . For a better understanding, Figure 3.11 helps to visualize how the waves in certain directions cancel out and others add in phase. From this figure, the front lobe is located above the array where the waves of the two holograms are in phase. The waves returning to the feed and going downwards are  $180^\circ$  out of phase, thus canceling out. One problem with this array is that the side lobe to the the right of the antenna will increase by at least  $3dB$  since the waves from both holograms are in phase.

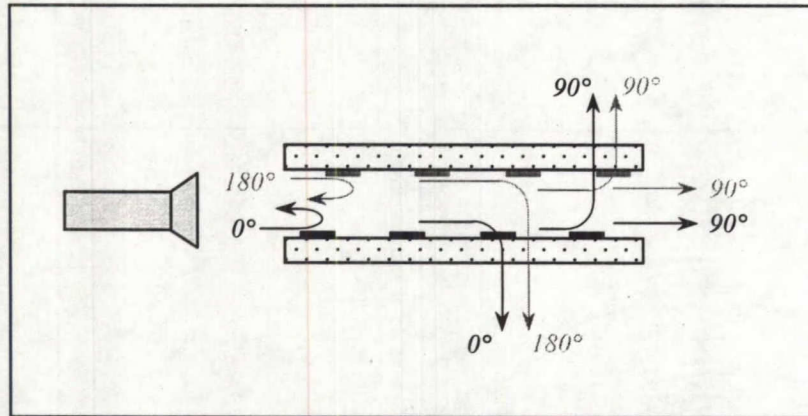


**Figure 3.11. Lobe suppression.**

Depending on the configuration, one must be careful about how to select the guided wavelength. For instance, in case (a) the free-space wavelength must be considered while in case (b), because of the dielectric slab, the guided wavelength must be used to evaluate the spacing between the two holograms. Note that in both designs the effects of mutual coupling are neglected. For the purpose of this thesis, only a two-element array, i.e., two-layer hologram, is

considered; however, more elements or a multiple layer hologram can be used for the suppression of the back lobe and the side lobe. This implies finding the correct spacing  $d$  between the elements (or holograms) in the array and the phase progression  $\beta_p$ .

One technique to reduce the effects of the lobe directed towards the feed is by recording an "offset-reference hologram" (offset feed) described in [13, p. 304]. However, with this method the feed is no longer in the same plane at the holographic plate. Moreover, this approach does not eliminate the back lobe. Therefore, the array approach is considered as the best compromise solution: it has the advantage of providing more gain than with the single layer holograms by enhancing the radiation in the desired direction, and at the same time increasing feed energy interception by the holograms.

## **3.2 Surface Wave Analysis**

### **3.2.1 Guided wavelength from the characteristic equations**

At optical frequencies, the calculation of the destructive pattern assumes that the hologram is recorded on a medium similar to air. Therefore, the resultant wavelength is the free-space wavelength. At microwave frequencies, because of the difficulty in etching microstrip lines on top of a foam with a dielectric constant close to 1, a Duroid material with a higher dielectric constant is used instead. This dielectric slab introduces a surface wave that propagates at a different velocity than the speed of light and results in a guided wavelength shorter than the free-space wavelength. It is possible to apply a surface wave analysis to evaluate in advance the guided wavelength by plotting the dispersion curves for a dielectric slab. In this analysis, the effects of the microstrip lines on the holographic antenna are not taken into account since their



width is less than  $\frac{\lambda_o}{40}$ . Also, the dimension of the antenna is greater than  $10\lambda_o$ , therefore the slab's dimension along the  $x$  and  $z$  axis is assumed to be infinite as shown in Figure 3.12. The thickness of the dielectric is  $t$  and the dielectric constant of the slab is  $\epsilon_{r2}$ . The slab is between two dielectric media which in the hologram case is air ( $\epsilon_{r1} = \epsilon_{r3} = 1$ ). Confinement of the wave occurs along the  $y$  axis only and power should spread along the  $x$  axis during propagation along the  $z$  direction. The slab can support  $TE^z$  and  $TM^z$  modes but since only the horizontal polarization is of interest (due to the horn illumination), the  $TE^z$  mode is considered.

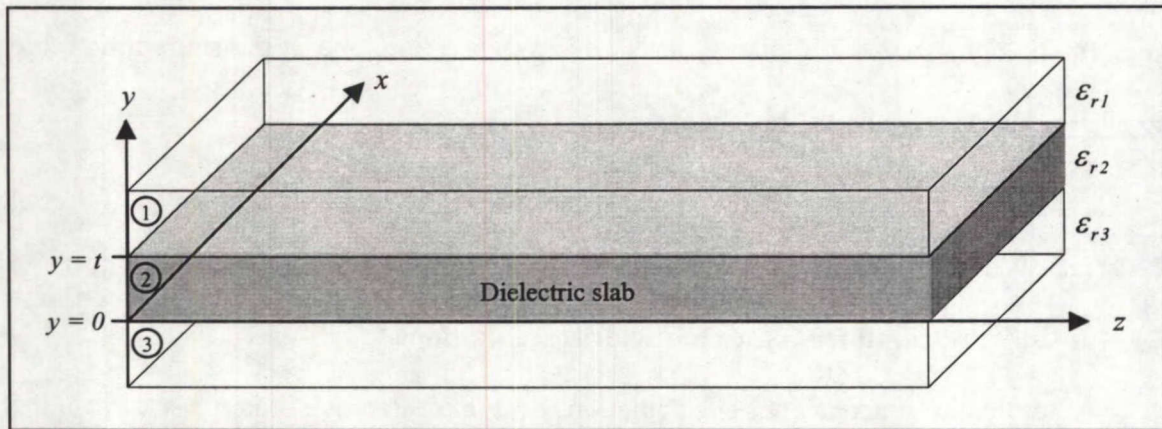


**Figure 3.12. Dielectric slab.**

By definition, for the selected mode,  $E_z = 0$  and the structure has no variation along  $x$ .

Therefore,  $\frac{\partial}{\partial x} = 0$  and  $\beta_x = 0$  for a lossless medium ( $\gamma = j\beta_z$ ). It is now possible to construct solutions for  $H_z$  in each region summarized in Table 3.2.

**Table 3.2 General solutions**

Region	Location	Solution
1	$y > t$	Evanescent dependency along +y
2	$0 < y < t$	Standing wave solution
3	$y < 0$	Evanescent dependency along -y

At the interfaces, the boundary conditions on the tangential fields are:

$$\begin{aligned} \text{at } y = 0 : E_{x2}(0, z) &= E_{x3}(0, z), \\ H_{z2}(0, z) &= H_{z3}(0, z). \\ \text{at } y = t : E_{x1}(t, z) &= E_{x2}(t, z), \\ H_{z1}(t, z) &= H_{z2}(t, z). \end{aligned} \quad (3-24)$$

In all three regions, the fields propagate with the same  $\beta_z$  along  $z$ , and from the detailed derivation in [22, Chapter 9] and enforcing the boundary conditions (3-24) the transcendental equation that  $\beta_z$  must satisfy for the  $TE^z$  modes is:

$$\tan(\beta_{y2}t) = \left[ \frac{2\beta_{y2}\alpha_{y1}}{\beta_{y2}^2 - \alpha_{y1}^2} \right], \quad (3-25)$$

where:

$$\begin{aligned} \alpha_{y1} &= \sqrt{\beta_z^2 - \omega^2 \mu_o \epsilon_1}, \\ \beta_{y2} &= \sqrt{\omega^2 \mu_o \epsilon_2 - \beta_z^2}. \end{aligned} \quad (3-26)$$

Before solving (3-25), one must determine the range of values for  $\beta_z$  such that  $TE^z$  modes are confined to the slab. If a mode is to be confined then  $\alpha_{y1}$  and  $\beta_{y2}$  must be real and the condition for a guided mode becomes:

$$(\omega\sqrt{\mu_o\epsilon_1} = \beta_1) < \beta_z < (\beta_2 = \omega\sqrt{\mu_o\epsilon_2}). \quad (3-27)$$

Using MATLAB [23] to solve the transcendental equation (3-25),  $\kappa_o$  versus  $\beta_z$  for the first mode ( $TE_0$ ) is plotted in Figure 3.13. In this case, the thickness of the slab is selected to be 20mils (0.0508cm) and the dielectric constants as 1 and 3.38.



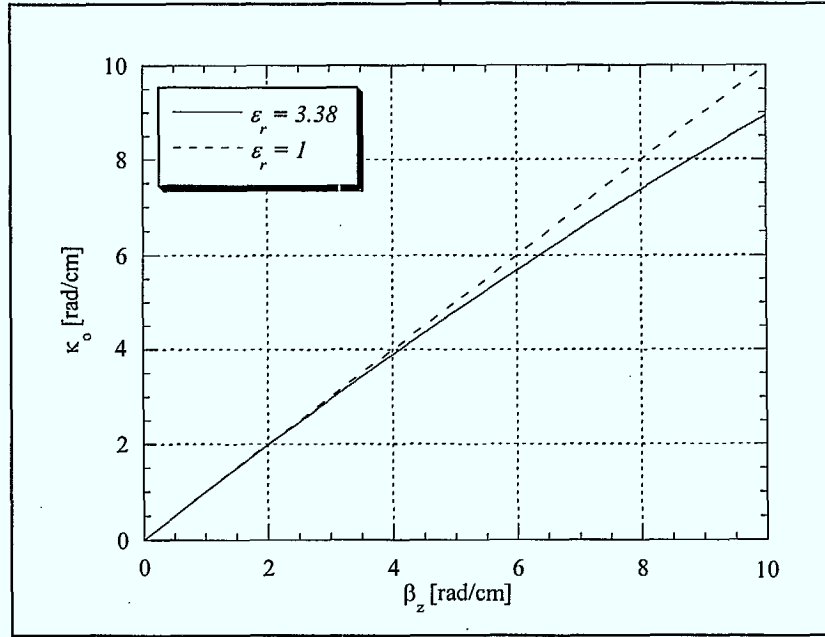


Figure 3.13.  $\kappa_o$  versus  $\beta_z$  for infinitely wide slab with  $t = 0.0508\text{cm}$ .

The above figure shows that as the dielectric constant of the slab increases, so does  $\beta_z$  with respect to  $\kappa_o$  (the wave's velocity decreases). Also, the guided wavelength can be evaluated at a desired frequency. For example, if  $f = 30\text{GHz}$  ( $\lambda_o \approx 1\text{cm}$ ), then  $\kappa_o = 6.2875\text{rad/cm}$  and from Figure 3.13,  $\lambda_g \approx 0.9385\text{cm} \approx 0.9385\lambda_o$  (note that  $\lambda_g = \frac{2\pi}{\beta_z}$ ).

The slab of Figure 3.12 was also analyzed based on the surface wave analysis done by [24, p. 236] where the characteristic equation for the  $TE_n$  modes is derived after the boundary conditions are enforced. The advantage of this method is the fact that the transcendental equation can be solved for only one mode while in [22], the characteristic equation must be evaluated for all modes. Nevertheless, both methods agree with each other and provide a good

approximation for the guided wavelength. In the case where the slab is not treated as infinitely wide, another method called the Point Matching Approach can be employed.

### 3.2.2 Guided wavelength from the point matching approach

It might be in some cases desirable to consider the effect of the dielectric slab's finite size on the guided wavelength. This analysis is possible with the Point Matching Approach (PMA) described in [22, Chapter 10] where the dielectric sheet is treated as a dielectric waveguide of finite dimensions as shown in Figure 3.14 (the waveguide is infinite in the  $z$  direction).

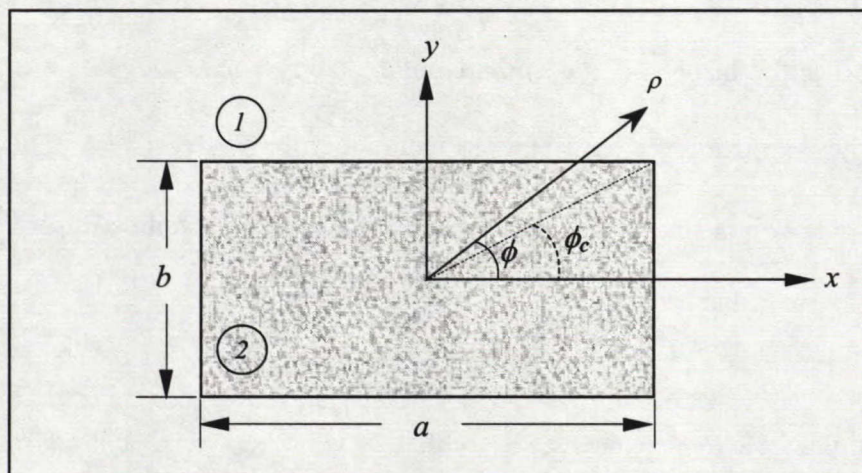


**Figure 3.14. Dielectric waveguide.**

In cylindrical coordinates, a solution for the  $E_z$  and  $H_z$  field components in regions 1 and 2 is proposed. The solution consists of an infinite sum of linearly independent basis functions selected from those generated by the method of separation of variables. Afterwards, a system of homogeneous linear equations is derived by enforcing the boundary conditions on the tangential fields at discrete points on the boundaries. A non-trivial solution exists only when the determinant vanishes. Finally, the determinant equation is solved using a root-finding algorithm.

Because the main electric field component is  $E_x$  (due to the horn illumination), the  $TE_x^{II}$  mode is considered. The  $\kappa_o$  versus  $\beta_z$  curve for the  $TE_x^{II}$  mode was computed for a dielectric waveguide of  $\epsilon_r = 3.38$  with  $a = 10cm$  and  $b = 0.0508cm$  (see [22] for all the details and Appendix A for the MATLAB program). With 11 matching points and using the least squares technique to extract the data from the curve, the guided wavelength at  $f = 30GHz$  was found to be  $\lambda_g \approx 0.9377cm \approx 0.9377\lambda_o$ , which is close to the result obtained previously with the infinitely wide slab. Note that for  $\beta_z$  values less than  $10rad/cm$  (as is the case here) the PMA program had difficulty finding roots since the dielectric waveguide is so thin. Therefore, the results obtained with this technique should not be considered 100% accurate. Also, when extrapolating the data using the least squares technique, the value of  $\lambda_g$  changes depending on the number of data points selected. Nevertheless, this technique could be useful in future design for thicker dielectric slabs.

To validate the theory developed with the array analysis, another method based on periodic structures is investigated to calculate  $\lambda_g$ . This technique is discussed in the following section.

### 3.2.3 Traveling wave antennas constructed from periodic structures

The holographic antenna may be treated as a periodically loaded traveling-wave structure known as a strip-loaded dielectric slab. This analysis is similar to the array analysis of Section 3.1.2 except that in this case, it is assumed that the array of loop antennas has an infinite number of elements. For simplicity, the array is considered to be a periodic structure where the



microstrip arcs are treated as straight infinitely long microstrip lines as shown in Figure 3.15, even though the hologram is quasi-periodic (periodic along the  $x$  axis when referring to Figure 3.4 and the  $z$  axis when referring to Figure 3.15). The quasi-periodicity of the structure will reduce the side lobe levels of the antenna pattern (as seen in Figure 3.5), these being at the same level as the two main lobes in the periodic case.

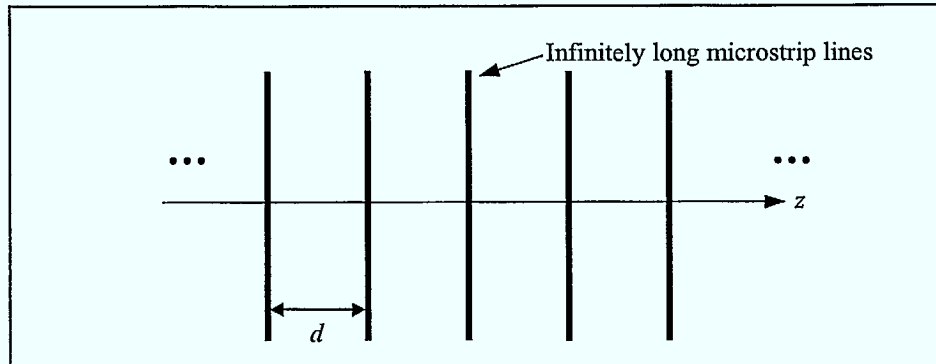


**Figure 3.15. Periodic approximation of the holographic antenna.**

The guided waves on a periodically loaded traveling-wave structure can be characterized using Floquet's Theorem described in [25, p. 186]. As in the surface wave analysis, the  $\kappa_o$  versus  $\beta_z$  curve is used to compute  $\lambda_g$ . The  $\kappa_o - \beta_z$  plane illustrated in Figure 3.13 can be separated into two main regions as shown in Figure 3.16.

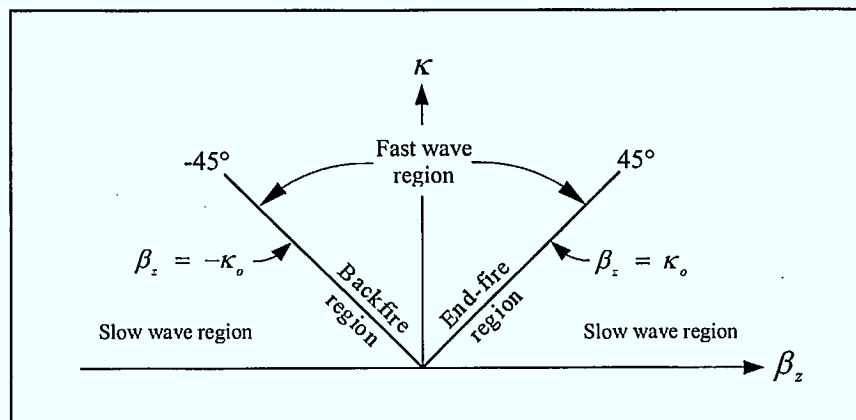


**Figure 3.16. Classification of the  $\kappa_o - \beta_z$  plane [25].**

Based on the above figure, the  $\kappa_o$ -versus- $\beta_z$  curve for the fundamental mode found with the surface wave analysis (Figure 3.12,  $\epsilon_r = 3.38$ ) is in the slow wave region. This result is expected since the holographic antenna is a slow wave type structure. Due to the periodicity of the structure and Floquet's Theorem, the fundamental mode will repeat itself on each element (or infinite strip also called cell) every  $\frac{2\pi}{d}$  as shown in Figure 3.17.

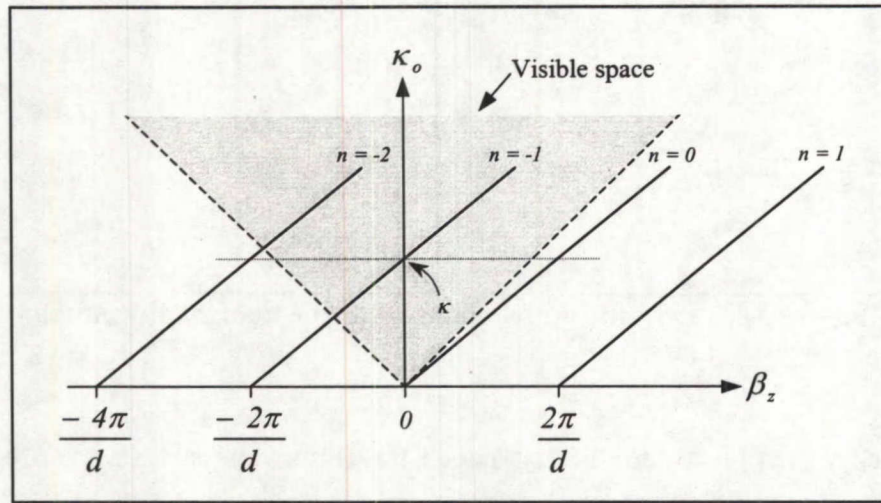


Figure 3.17.  $\kappa_o$  versus  $\beta_z$  for a periodically loaded traveling-wave structure.

The Floquet modes are denoted by  $n = 0, \pm 1, \pm 2, \dots$  where:

$$\beta_n = \beta_0 + \frac{2\pi}{d} n, \quad (3-28)$$

and  $\beta_0$  corresponds to the fundamental mode ( $n = 0$  in Figure 3.17).

Note that the curves in Figure 3.17 are plotted as straight lines. In general this need not be the case, but based on the results obtained with the surface wave analysis and for the region of interest, this approximation is valid. The number of observable beams in the far field is equal to the number of Floquet modes in the fast wave region known as the radiating region (also called

the visible space). Based on [25] (and also on array theory), the peak of the radiation lobe measured from broadside, due to an essentially radiating  $n^{\text{th}}$  mode, is approximated by:

$$\sin \theta_n = \frac{\beta_n}{\kappa_o}, \quad (3-29)$$

where  $\theta_n$  is measured from broadside. Therefore from Figure 3.17, at frequency  $\kappa_o = \kappa$  ( $\beta_z = 0$ ) the  $n = -1$  mode will be radiating at  $\theta_n = 0^\circ$  (corresponding to broadside) and  $\theta_n = 180^\circ$ . Other modes should not be observed at the desired frequency since they do not appear in visible space. However, one must be careful with this last statement. The  $n = -2$  and  $n = 0$  modes are very close to the visible space boundary at  $\kappa_o = \kappa$ . Due to the beamwidth of the lobe at these two modes, some spillover into the visible space will occur and a side lobe will be observable at  $\beta_z = \kappa$  ( $\theta_n = 90^\circ$ ) and  $\beta_z = -\kappa$  ( $\theta_n = -90^\circ$ ). In the case where the fundamental mode follows the visible space boundary ( $\lambda_g = \lambda_o$ ), the level of the side lobes is equal to the level of the main lobe. But for the above case, the side lobe levels will be slightly suppressed since only a portion of the energy is in the fast wave region.

Since the mode of interest is the  $n = -1$  harmonic, from (3-28),

$$\beta_{-1} = \beta_o - \frac{2\pi}{d}. \quad (3-30)$$

Substituting  $\frac{2\pi}{\lambda_g}$  for  $\beta_o$ , (3-30) becomes:

$$\beta_{-1} = \frac{2\pi}{\lambda_g} - \frac{2\pi}{d} = 2\pi \left[ \frac{1}{\lambda_g} - \frac{1}{d} \right]. \quad (3-31)$$

At broadside,  $\beta_{-1} = 0$  and from (3-31),

$$d = \lambda_g. \quad (3-32)$$

This implies at a certain frequency that, in order to obtain broadside radiation, the condition described by (3-32) must be met. In the visible space, by substituting (3-31) into (3-29) it is now possible to express the beam peak for the mode of interest as:

$$\sin \theta_{-1} = \frac{\beta_{-1}}{\kappa_o} = \lambda_o \left[ \frac{1}{\lambda_g} - \frac{1}{d} \right]. \quad (3-33)$$

Since in the design of the holographic antenna the distance  $d$  between the elements is chosen to be one free-space wavelength, (3-33) becomes:

$$\sin \theta_{-1} = \frac{\beta_{-1}}{\kappa_o} = \left[ \frac{\lambda_o}{\lambda_g} - 1 \right]. \quad (3-34)$$

Therefore, at the desired frequency  $f_o$  the antenna will have a beam squint. Based on this beam peak angle the value of the guided wavelength is:

$$\lambda_g = \frac{\lambda_o}{(\sin \theta_{-1} + 1)}. \quad (3-35)$$

Notice that (3-35) is the same as (3-14) found in Section 3.1.2 using array theory with the exception that broadside is located at  $0^\circ$  instead of  $90^\circ$  because ' $\theta$ ' is measured differently. Again, the beam peak is to be measured experimentally. Also note that it would be possible to predict the beam peak value  $\theta_{-1}$  based on the guided wavelength found theoretically with the surface wave analysis described in Section 3.2.1.

It would be practical based on the  $n = -1$  curve of Figure 3.17 to determine the beam scan  $\theta_2$  at other frequencies ( $\kappa_2$ ). This analysis can simply be carried out using the set of points



$P_1 = (\beta_1, \kappa_1)$  and  $P_2 = (\beta_2, \kappa_2)$  shown in Figure 3.18, where  $\kappa_1$  and  $\beta_1$  are known from an experimentally measured or theoretically known  $\theta_1$  value, and  $S = \frac{2\pi}{d}$ .

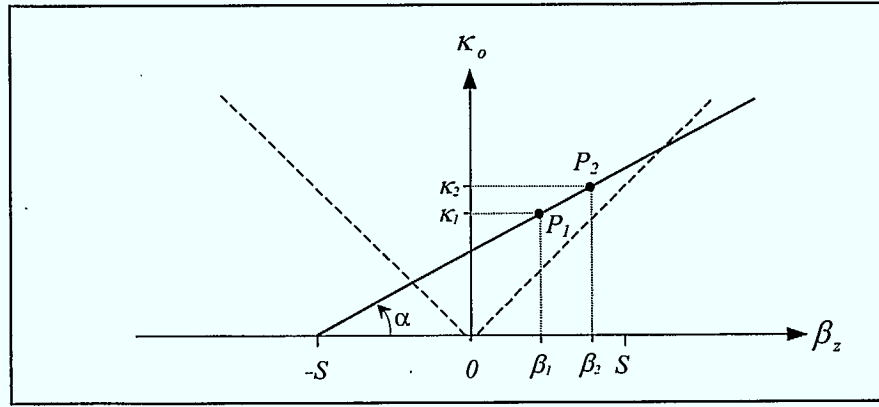


Figure 3.18. Beam squint at two different frequencies.

Again it is assumed that the  $n = -1$  curve is linear. Therefore, based on the graph,

$$\tan(\alpha) = \frac{\kappa_1}{\beta_1 + S} = \frac{\kappa_2}{\beta_2 + S}. \quad (3-36)$$

From (3-29),  $\sin(\theta_1) = \frac{\beta_1}{\kappa_1}$  and  $\sin(\theta_2) = \frac{\beta_2}{\kappa_2}$ , so that the above equation becomes:

$$\left[ \sin(\theta_1) + \frac{S}{\kappa_1} \right] = \left[ \sin(\theta_2) + \frac{S}{\kappa_2} \right]. \quad (3-37)$$

Rearranging (3-37), the beam peak at an alternative frequency is found to be:

$$\theta_2 = \arcsin \left[ \sin(\theta_1) + S \left( \frac{1}{\kappa_1} - \frac{1}{\kappa_2} \right) \right], \quad (3-38)$$

where  $\kappa_1$ ,  $\theta_1$ , and  $\kappa_2$  are known values.

Equation (3-38) will be useful to predict the behavior of the holographic antenna and to compare the experimental results with theory in Chapters 4 and 5. Also note that the periodic structure analysis agrees with array theory for approximating the guided wavelength of the hologram. However, because the dielectric sheet is so thin, its effect on the guided wavelength is minimal. Therefore, using the free-space wavelength as a first order approximation is good enough to validate the hologram theory at microwave frequencies.

### 3.3 Incident Plane Wave on a Dielectric Sheet

The different guided wavelength analyses done in the previous sections showed how the spherical wave's velocity is affected by a dielectric slab. In this section the effects of the dielectric sheet on a plane wave are evaluated. Figure 3.19 illustrates the top view of the holographic antenna in the receiving mode where it is treated as a dielectric slab of thickness  $t$  infinite along the  $x$  and  $y$  axes. Again the effect of the conducting strips is neglected and the plane wave, illustrated as  $i$  in the figure below, is normally incident on the slab and propagating in the positive  $z$  direction with its electric field linearly polarized along the  $x$  axis.

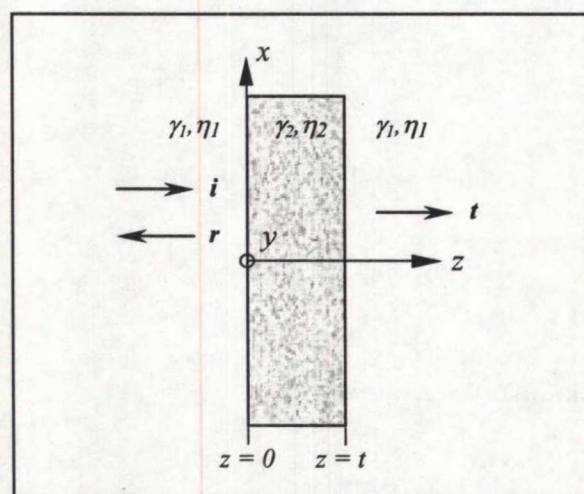


Figure 3.19. Incident wave on dielectric sheet.

Once the plane wave reaches the dielectric interface a percentage of the wave is reflected back ( $r$ ) towards the  $-z$  direction while the rest of the wave is transmitted ( $t$ ) onto the other side of the slab. Both the reflected and transmitted wave are linearly polarized and along with the incident wave they can be expressed in the different regions as:

for  $z < 0$ :

$$\begin{aligned}\vec{E}^i &= \hat{x}E_o e^{-\gamma_1 z} & \vec{E}^r &= \hat{x}\Gamma_s E_o e^{+\gamma_1 z} \\ \vec{H}^i &= \hat{y} \frac{E_o}{\eta_1} e^{-\gamma_1 z}, \text{ and } & \vec{H}^r &= -\hat{y}\Gamma_s \frac{E_o}{\eta_1} e^{+\gamma_1 z},\end{aligned}\quad (3-39)$$

for  $0 < z < t$ :

$$\begin{aligned}\vec{E}^s &= \hat{x}(Ae^{-\gamma_2 z} + Be^{+\gamma_2 z}) \\ \vec{H}^s &= \hat{y} \frac{1}{\eta_2} (Ae^{-\gamma_2 z} - Be^{+\gamma_2 z}),\end{aligned}\quad (3-40)$$

and for  $z > t$ :

$$\begin{aligned}\vec{E}^t &= \hat{x}T_s E_o e^{-\gamma_1(z-t)} \\ \vec{H}^t &= \hat{y}T_s \frac{E_o}{\eta_1} e^{-\gamma_1(z-t)},\end{aligned}\quad (3-41)$$

where,  $\Gamma_s$  corresponds to the reflection coefficient at  $z = 0$ , and  $T_s$  the transmission coefficient at  $z = t$ . Applying the boundary conditions on either side of the discontinuities by matching the tangential fields at  $z = 0$  and  $z = t$ , expressions for  $\Gamma_s$  and  $T_s$  can be obtained. Based on the derivations by [26, Section 4.5], the coefficients become:

$$\begin{aligned}\Gamma_s &= \frac{\Gamma_{12}(1 - e^{-2\gamma_2 t})}{1 - \Gamma_{12}^2 e^{-2\gamma_2 t}}, \\ T_s &= \frac{(1 - \Gamma_{12}^2) e^{-\gamma_2 t}}{1 - \Gamma_{12}^2 e^{-2\gamma_2 t}},\end{aligned}\quad (3-42)$$

where  $\Gamma_{12} = \frac{\eta_2 - \eta_1}{\eta_2 + \eta_1}$ ,  $\eta_1 = \sqrt{\frac{\mu_o}{\epsilon_1}}$ , and  $\eta_2 = \sqrt{\frac{\mu_o}{\epsilon_2}}$ . Also, for the lossless case  $\gamma_2 = j\beta_2$ .

With Poynting's theorem it is possible to derive the time-average power density of the three waves. For TEM waves, the complex Poynting vector is defined as:

$$P = \frac{1}{2} \text{Re}(\vec{E} \times \vec{H}^*) = \frac{1}{2} \text{Re}(\hat{x}E_x \times \hat{y}H_y^*) = \hat{z} \frac{1}{2\eta_1} |E_x|^2. \quad (3-43)$$

Applying (3-43) on both sides of the dielectric slab, the time-average power density of each wave is:

$$\begin{aligned} P_i &= \hat{z} \frac{1}{2\eta_1} |E_o|^2, \\ P_r &= \hat{z} \frac{1}{2\eta_1} |E_o \Gamma_s|^2, \\ P_t &= \hat{z} \frac{1}{2\eta_1} |E_o T_s|^2. \end{aligned} \quad (3-44)$$

Using (3-44), the percentage of the incident wave that is reflected and transmitted has been evaluated with Mathcad<sup>®</sup>. For a dielectric slab with a dielectric constant of 3.38 and a thickness of 20mils (0.0508cm) 11.4% of the incident plane wave is reflected while 88.6% is transmitted to the other side. Assuming that the holographic antenna focuses all the energy it receives into the feed, then only 88.6% of the transmitted wave will be captured by the feed horn, which corresponds to approximately a 0.5dB loss. It is possible to reduce this loss by decreasing the thickness of the slab or using another material with a lower dielectric constant. Also, in the lossless case, the slab can be matched with  $\Gamma_s = 0$  by setting  $t = \frac{\lambda_2}{4}$  and  $\eta_2 = \sqrt{\eta_1 \eta_3}$ , where the medium at the right of the slab (referring to Figure 3.14) has a dielectric constant of  $\epsilon_{r3}$ .

## CHAPTER 4

### Holographic Antenna Concept Validation and Design Procedure

Based on the theory previously described in Chapters 2 and 3, holographic antenna prototypes are designed and measured experimentally. The objective is to validate the concept that a hologram can function as an antenna. This chapter describes the antenna parameters along with the test setup used to properly measure the radiation patterns. Discussion includes radiation efficiency and beam squint issues. Guidelines will be established for the efficient design of holographic antennas

#### 4.1 Validation of a Holographic Antenna

##### 4.1.1 Prototype and test setup

In order to validate the hologram concept at microwave frequencies and verify the results obtained in [5], several prototypes with the dimensions illustrated in Figure 4.1 were fabricated and tested. The novelty of this antenna is the frequency of operation which is at Ka-band (26-40GHz) instead of X-band (8.2-12.4GHz). The design parameters of the three prototypes are listed in Table 4.1. The width  $w$  of the microstrip lines is chosen to be as small as possible in order to approach the ideal condition based on the interference pattern of infinitely narrow strips. The thickness  $t$  of the dielectric slab is also very thin to reduce the effects of the dielectric on the surface wave, resulting in a very low profile antenna. The aperture size of the holograms is selected such that the antennas can be compared to other currently available LMCS in-house antenna candidates such as lenses and reflectors.



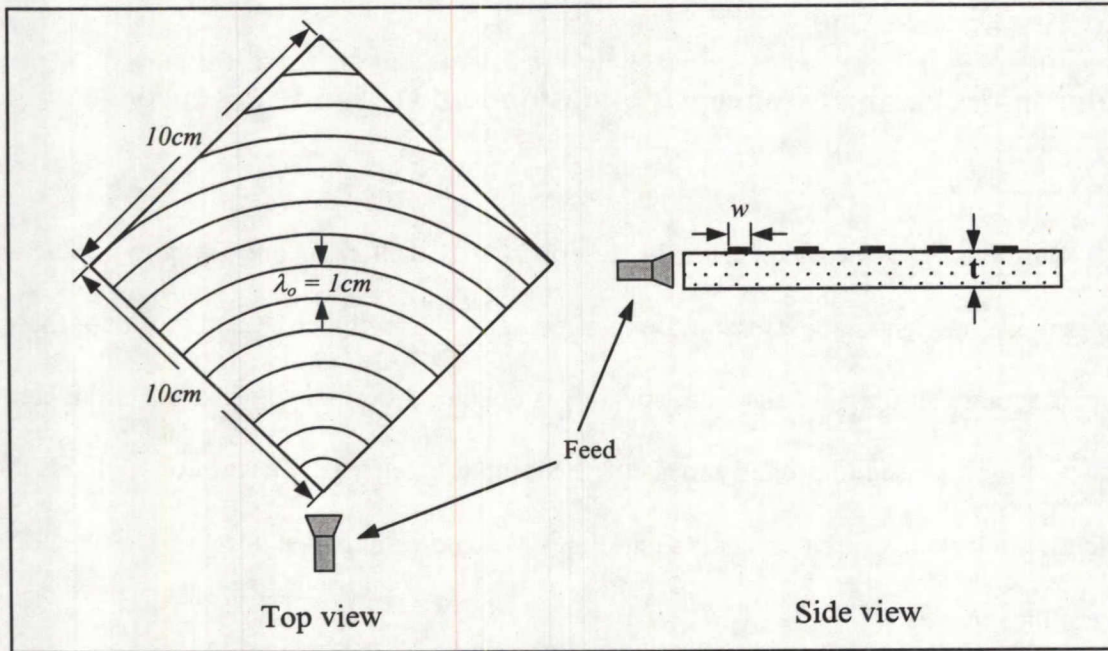


**Figure 4.1. Holographic Antenna.**

**Table 4.1 General properties of holographic antenna**

Prototype	Dielectric	Dielectric Constant	Dielectric thickness	Frequency of operation	Width of microstrip lines
1	Duroid 3003	$\epsilon_r = 3$	$t = 20\text{mils}$	$f_o = 30\text{GHz}$	$w = 10\text{mils}$
2	FR4	$\epsilon_r \approx 4$	$t = 30\text{mils}$	$f_o = 30\text{GHz}$	$w = 10\text{mils}$
3	Duroid 4003	$\epsilon_r = 3.38$	$t = 20\text{mils}$	$f_o = 30\text{GHz}$	$w = 10\text{mils}$

The directivity  $D$  of these antennas with a uniform aperture distribution is calculated based on the aperture area  $A$  (at  $f_o = 30\text{GHz}$ ) using the following equation [19]:

$$D = \frac{4\pi A}{\lambda_o^2} \approx \frac{4\pi(10\text{cm} \cdot 10\text{cm})}{(1\text{cm})^2} \approx 31\text{dB} \quad (4-1)$$

This value will be used to evaluate the efficiency of the holographic antennas from the measured gain value.



An accurate test setup is required for the measurement. A special frame, described in Appendix B, was developed which allows an accurate and an easy alignment of the antenna and a feed horn for proper hologram illumination. The frame encloses a piece of foam on which the holographic antenna is attached and allows measurements in both the E and H-plane. For validation purposes, only the H-plane is considered since this is the plane in which the four lobes should be present. Also if a beam scan occurs, the E-plane cut will miss the beam peak and therefore does not provide the appropriate pattern and the maximum gain value. For the tests at this stage, the focal point  $f_p$  was not optimized to obtain maximum gain. Instead, for each prototype the feed was placed at the tip of the antenna, i.e.  $f_p = 0$ , as shown in Figure 4.2. This is equivalent to assuming that the feed phase center is in the plane of the horn aperture.

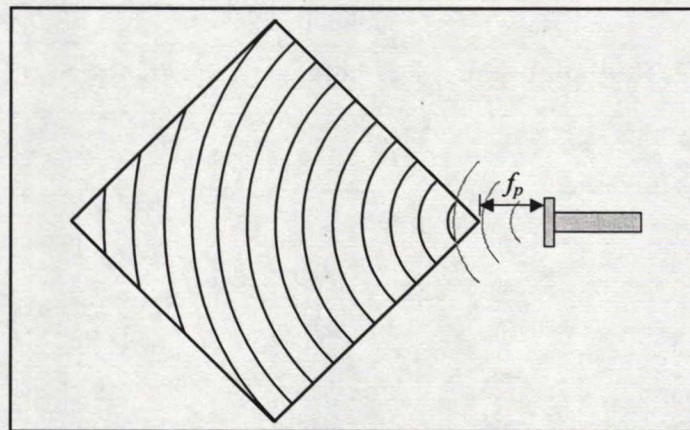


**Figure 4.2. Focal point with respect to hologram.**

The measured H-plane patterns of the prototypes described in Table 4.1 are illustrated in Figure 4.3. Based on these initial results, one can see that four beams are present in the radiation patterns, denoted by **F** for the front lobe, **B** for the back lobe, **S** for the lobe towards the feed and **T** for the lobe on top of the antenna. Figure 4.4 shows the four lobes with respect to the antenna. The results also agree with the results in [5] in terms of the radiation pattern.



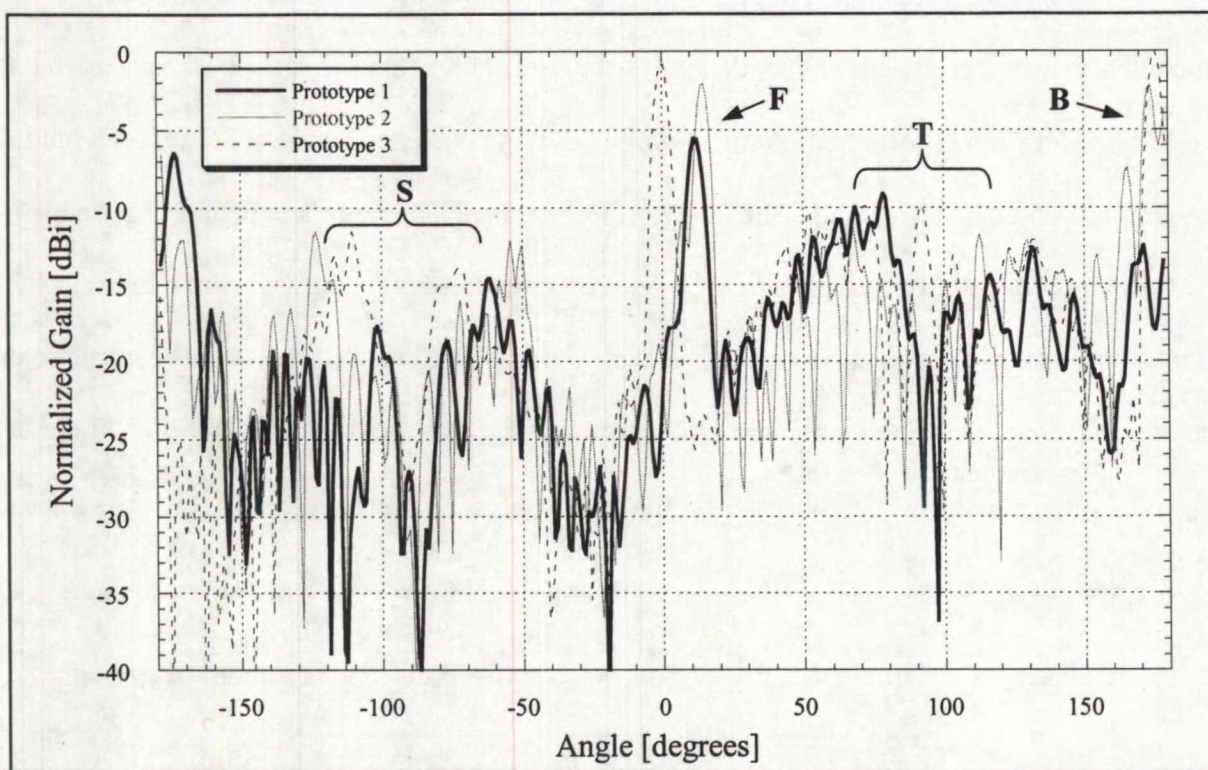


**Figure 4.3. Radiation pattern of holographic antenna at  $f_o = 30\text{GHz}$ .**

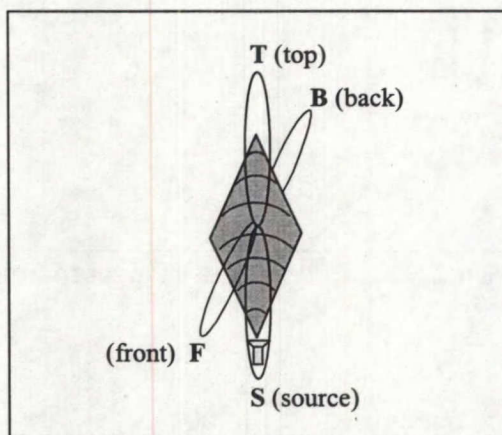


**Figure 4.4. Radiation lobes with respect to the hologram.**

The efficiency of these holograms is less than 5%, which was expected since the focal point was not optimized for gain and only a portion of the interference pattern (the destructive

one) reconstructs the object wave. Also, these antennas fall into the thin phase hologram category which is renowned for its relatively low efficiency (see [12] for more details on this topic). A second important observation is the level of the **S** and **T** side lobes. The lobe towards the feed **S** is significantly reduced due to the feed blockage. This lobe will interfere with the open waveguide and probably affect the return loss of the feed. If the return loss degradation is significant, the gain of the antenna will drop. As for the **T** lobe, the pattern is not uniform and is similar to the radiation pattern of an open waveguide. It is possible at this location that the fields generated by the hologram interfere with some spillover from the feed. Also, the frame reflects some of the transmitted fields which introduces the null around  $90^\circ$ .

The most important observations are the beam squint noticeable in all cases (observed for the **B** lobe for prototype #3) and the phase errors in the first two prototypes (beam width is wider than for the last prototype). The beam squint was expected because the element spacing is  $\lambda_o$  instead of  $\lambda_g$ , resulting in a linear phase progression over the hologram. As for the other phase errors, their existence can be observed from the beam deformation and unequal sidelobes of the **F** and **B** lobes. Since the first prototype consists of a very soft dielectric (Duroid 3003) with aberration on the surface of the hologram, these surface deformities translate into phase problems. The FR4 antenna is a lossy anisotropic substrate and is thicker than the other dielectrics. Therefore some phase errors and a gain reduction are expected with the second prototype. Finally an unfocused feed and a non-ideal spherical wave generated by the open waveguide will strongly contribute to the phase errors. Based on these observations, future antennas will be designed on the more rigid Duroid 4003 with a thickness of *20mils*. The FR4 can also be considered for low cost and rigidity but if a microstrip feed is to be used and



integrated directly onto the hologram instead of the open waveguide, the complexity of the design will significantly increase with the anisotropic substrate.

The third prototype was tested a second time where the focal point  $f_p$  was optimized for maximum gain. It was noticed when adjusting the feed's position that a  $2mm$  offset from the focal point of the hologram can reduce the gain by about  $3dB$ . This focusing effect was also explored in [5] where a gain reduction of  $6dB$  was observed when the feed is moved by  $0.6\lambda$  away from the hologram. The H-plane co-polarization and cross-polarization of the optimized antenna are shown in Figure 4.5 along with the pattern of the array of circular arc antennas described in Section 3.1.3 of Chapter 3 for comparison. The tip of the antenna is inside the open waveguide.

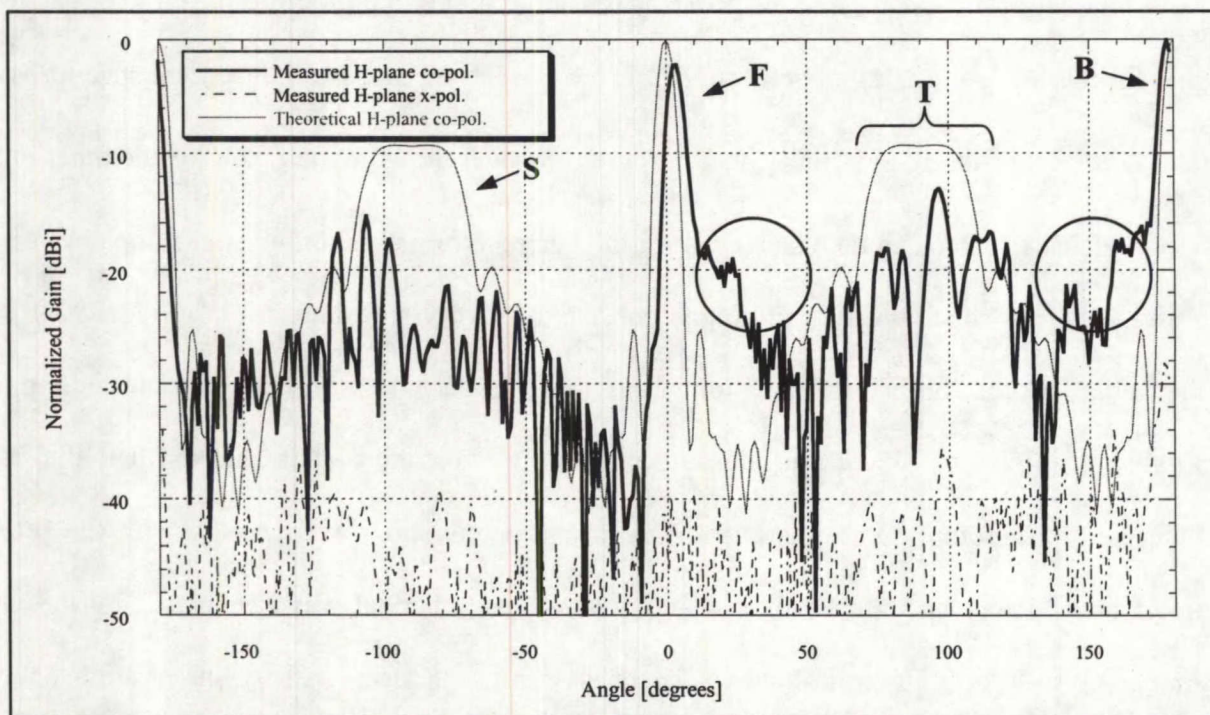
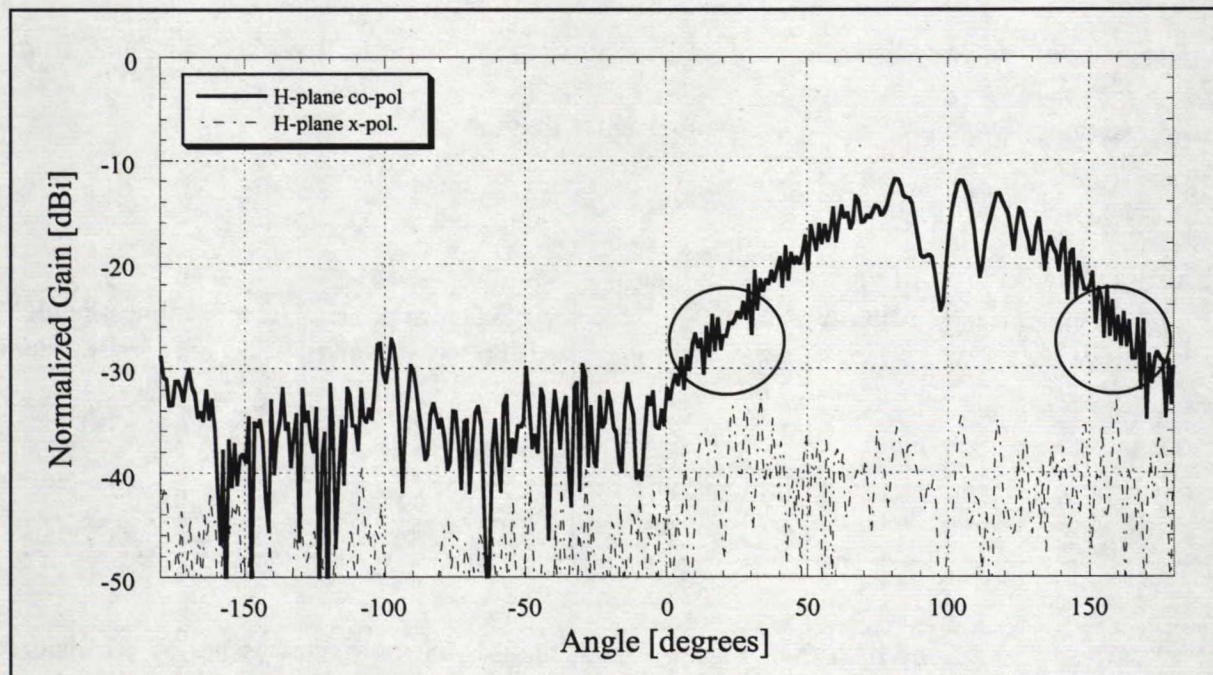


Figure 4.5. Radiation pattern of the optimized single-layer holographic antenna at  $f_o = 30GHz$ .



By properly focusing the feed, a gain of  $19\text{dB}$  was achieved, which translates to an efficiency of  $6.3\%$ . The insertion loss of the single-layer hologram, which is the difference between the  $S_{12}$  of the antenna with and without the conducting strips, measured by inserting the hologram between two waveguides, was also evaluated and the maximum efficiency was found to be approximately  $10\%$ . This measurement does not take into account the effects of aperture tapering and the phase errors which explains why the antenna measurement results show an efficiency less than  $10\%$ . As mentioned before, based on the above figures the lobe levels of S and T are significantly less than the theoretical value due to some interference and blockage from the feed. To verify the contribution of the feed on the radiation pattern of the holographic antenna, the feed's antenna pattern (using the same setup as in Figure 4.2 without the hologram) was measured and is plotted in Figure 4.6.



**Figure 4.6. H-plane radiation pattern of feed without holographic antenna.**

The pattern in Figure 4.6 was normalized to the maximum gain value of the optimized single layer (or continuous-strip) holographic antenna. Note that the null at  $90^\circ$  is caused by partial blockage from the frame. It is clear from Figures 4.5 and 4.6 that what appears to be side lobes with some phase errors (inside the circled regions) does not come from the hologram itself but from the feed. These observations show indeed that the feed's spillover highly interferes with the hologram. At  $-90^\circ$  the lobe is mainly due to some scattering from the hologram onto the feed since the radiation from the feed contributes little to the S lobe.

Returning to Figure 4.5, the theoretical and measured beamwidths are quite similar ( $\approx 6^\circ$ ) and the cross-polarization level is better than  $28dB$ . Similar to the previous measurements the pattern shows a beam squint that changes with frequency since the holographic antenna behaves like a traveling wave antenna. The beam peak location for different frequencies is listed in Table 4.2 along with the theoretical values calculated from (3-38) in Chapter 3 using  $f_1 = 30GHz$  as the center frequency.

**Table 4.2 Beam peak at various frequencies**

Frequency $f$ [GHz]	Beam peak of F lobe [Experimental results]	$\Delta$ Beam peak [BP( $f_2$ ) - BP(30GHz)]	Beam peak [Theoretical values]
28.0	2.00°	-1.68°	-4.10°
29.0	3.00°	-0.68°	-1.98°
30.0	3.68°	0°	0°
31.0	5.69°	2.01°	1.85°
32.0	7.37°	3.69°	3.58°

Even though the measured beam peak at the desired frequency is not at broadside, the above results are still useful in comparing the experimental scan rate versus frequency with the theoretical values. The measured beam peak values can be normalized from the center frequency



result as shown in the  **$\Delta$ Beam peak** column. For example, at  $29.0\text{GHz}$ ,  $\Delta\text{Beam peak} = \text{BP}(29) - \text{BP}(30) = 3^\circ - 3.68^\circ = -0.68^\circ$ . By looking at the  **$\Delta$ Beam peak** column, for frequencies less than  $f_i$  the scan rate is less than the predicted one shown in the last column. However, for the frequencies greater than  $f_i$  the measured and theoretical scan rates are quite similar. Note that the front lobe and the back lobe have a slightly different scan angle. This effect can be attributed to the dielectric slab on which the microstrip lines are etched as shown in Figure 4.7. The front lobe is probably less affected by the dielectric and thus squints differently than the back lobe.

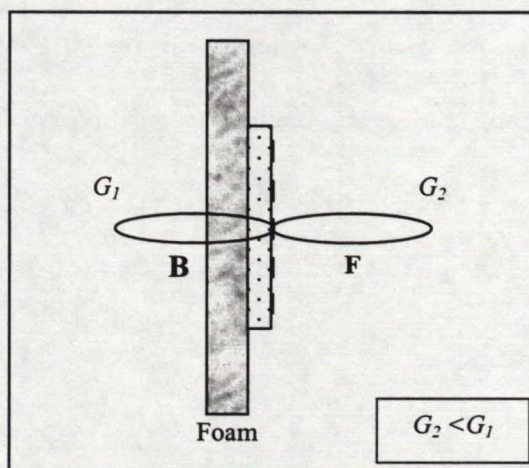


**Figure 4.7. Antenna setup.**

Furthermore, by closely looking at the main and back lobe levels, one can notice a gain difference of about  $2\text{dB}$ . Because the hologram's backside is facing the foam on the frame (again referring to Figure 4.7) it is possible that the fields on this side are better captured due to the higher dielectric constant. The dielectric slab of the antenna on the backside probably contributes to a greater extent to this gain increase than the foam because of its higher dielectric constant. Nevertheless the dielectric constant of the foam was evaluated to make sure it is close

to that of air and that its effect on the radiation pattern is minimal. The evaluation is explained in detail in Appendix C and the dielectric constants of the foam at different frequencies are summarized in Table 4.3.

**Table 4.3 Dielectric constant of foam**

Frequency $f$ [GHz]	Dielectric constant $\epsilon_r^f$
28.000	1.04
29.008	1.03
30.016	1.03
31.000	1.04
32.000	1.04

From the above results, the foam is virtually transparent to the antenna and should not affect its performance. Therefore it can be concluded that the gain increase on the backside of the hologram is attributed to the antenna substrate only. This issue will be discussed in more detail in the next chapter. Now in the following section, the first prototype of the dipole hologram is evaluated.

#### 4.1.2 Dipole hologram

The dipole hologram shown in Figure 3.7 (a) of Chapter 3, is first tested. The elements are spaced by  $d = \lambda_o$  and each dipole has a length of  $0.5\lambda_o \approx 0.5cm$  at  $f_o = 30GHz$ . The dielectric on which the strips are etched is again Duroid 4003 with a thickness of 20mils. The measured H-plane patterns are shown in Figure 4.8. Based on these H-plane patterns, the dipole hologram is seen to behave similarly to the continuous-strip hologram analyzed in Section 4.1.1. However, the gain drops by about 2dB compared to the continuous-strip case, which is expected due to the gaps between the elements resulting in less energy interception. The co-polarization



pattern shows somewhat more phase errors than with the **ARPS** simulation and the continuous-strip case (shown in Figure 4.5). These phase errors can be attributed to the fact that the phase on each element is more difficult to control than the phase on a continuous-strip (the current on the dipoles located on the same radius as a continuous strip should ideally be equal). Also, the different phases on the dipoles contribute to a greater beam scan than for the continuous-strip hologram. Note that **ARPS** does not take into account the mutual coupling between the elements, although this coupling does exist in the real structure and therefore introduces some phase errors.

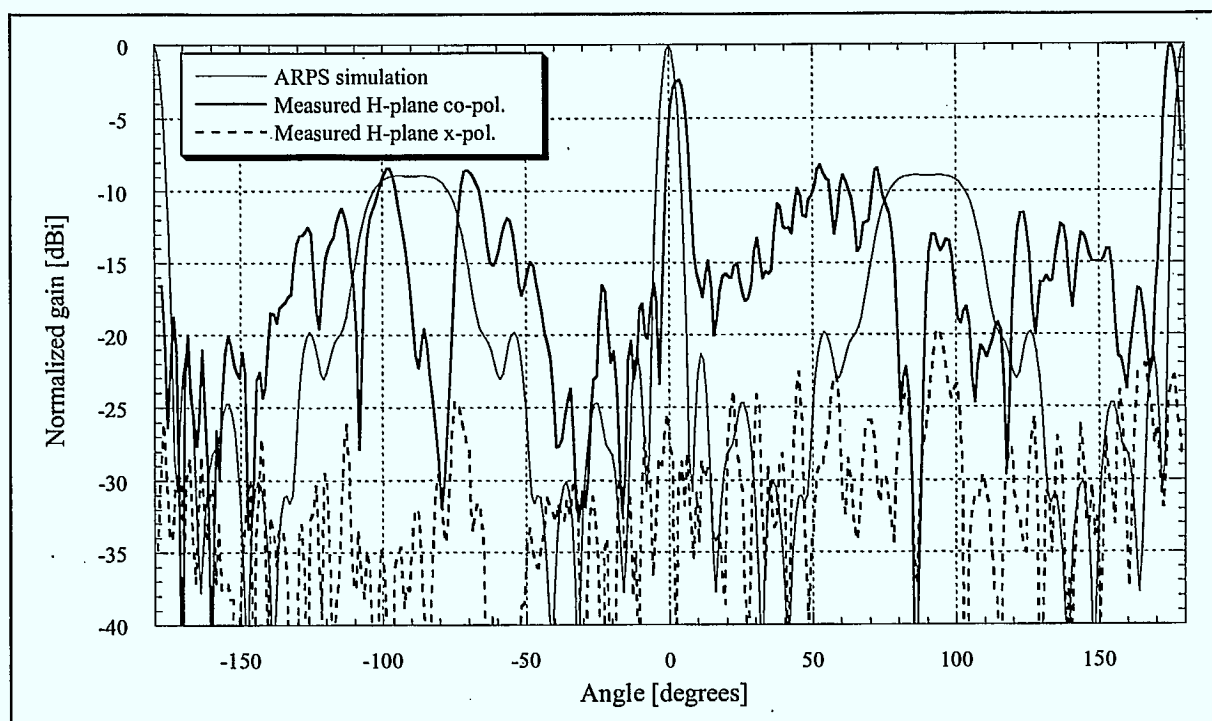
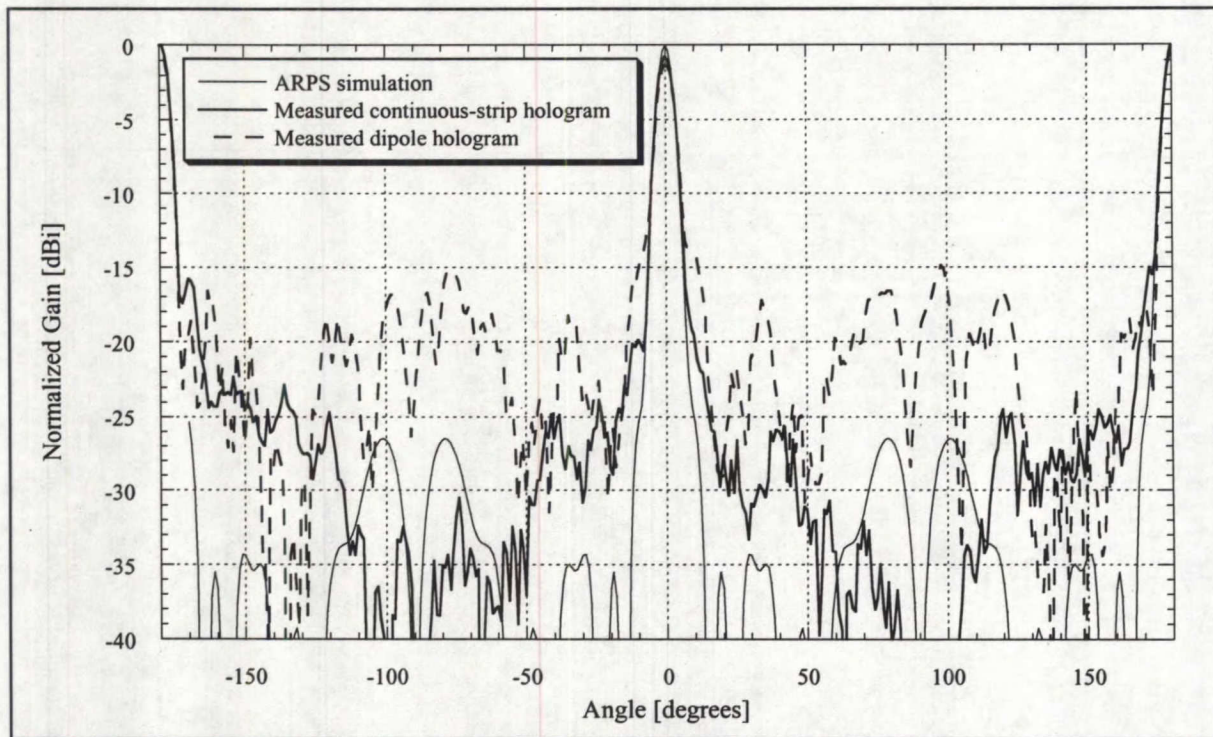


Figure 4.8. H-plane radiation patterns of the dipole hologram for  $d = \lambda_0$ .

As mentioned before, the cross-polarization in the H-plane cut is quite low due to the symmetry of the structure. In the E-plane, however, the cross-polarization will be significantly

greater with the continuous-strip hologram but should be suppressed with the dipole hologram. Because of the large beam squint at  $f_o = 30\text{GHz}$  the measured E-plane patterns are generally not very informative. Therefore the patterns at  $f = 28\text{GHz}$  where the beam peak is almost at broadside are considered. The E-plane co-polarization and cross-polarization of the continuous-strip hologram and the dipole hologram for  $d = \lambda_o$  are illustrated in Figure 4.9 and Figure 4.10 respectively.



**Figure 4.9. E-plane co-polarization patterns at  $f = 28\text{GHz}$ .**

The E-plane co-polarization of the dipole hologram is similar to the **ARPS** prediction but with some phase errors (observed from the main beam). The side lobe levels are also higher. Note that for the continuous-strip case, the level of the side lobes around  $-90^\circ$  and  $90^\circ$  are zero. This is in agreement with the **ARPS** simulations (see Figure 3.9 in Chapter 3) showing that as



the number of elements increases in the array of dipoles (or as the antenna gets closer to the continuous-strip case), the side lobes disappear. Therefore the results agree with theory. The front and back lobe beam widths of both the continuous-strip and dipole hologram are slightly wider than the simulated results.

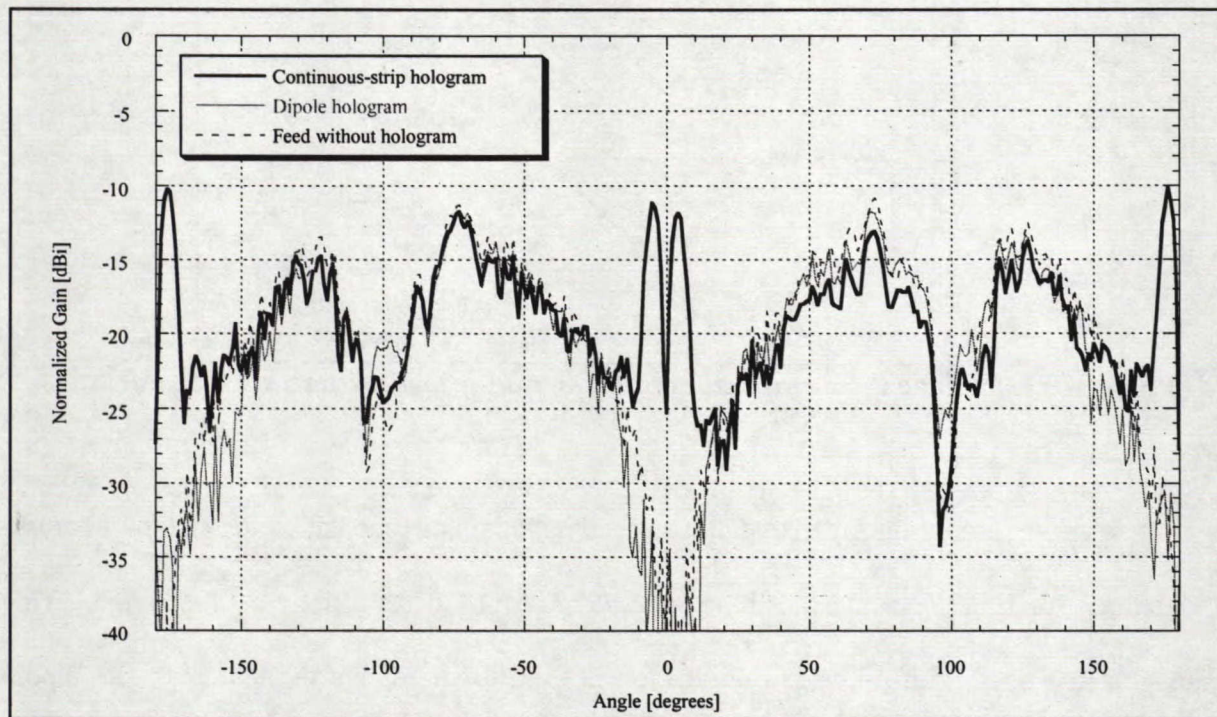


**Figure 4.10. Measured E-plane cross-polarization patterns at  $f = 28\text{GHz}$ .**

From Figure 4.10, the cross-polarization of the continuous-strip hologram is better than  $11\text{dB}$  at broadside. With the dipole hologram, there is a significant improvement where the cross-polarization is better than  $30\text{dB}$  at broadside. Both the continuous-strip and the dipole hologram show a significant high cross-polarization level at  $\pm 90^\circ$ . Because this pattern is similar to the H-plane pattern of the feed illustrated in Figure 4.6, the pattern of the feed without the antenna (but in the same setup used to evaluate the cross-polarization of the holograms) was



measured. This last measurement is given by the dotted line in Figure 4.10, while the setup is shown in Figure 4.11.

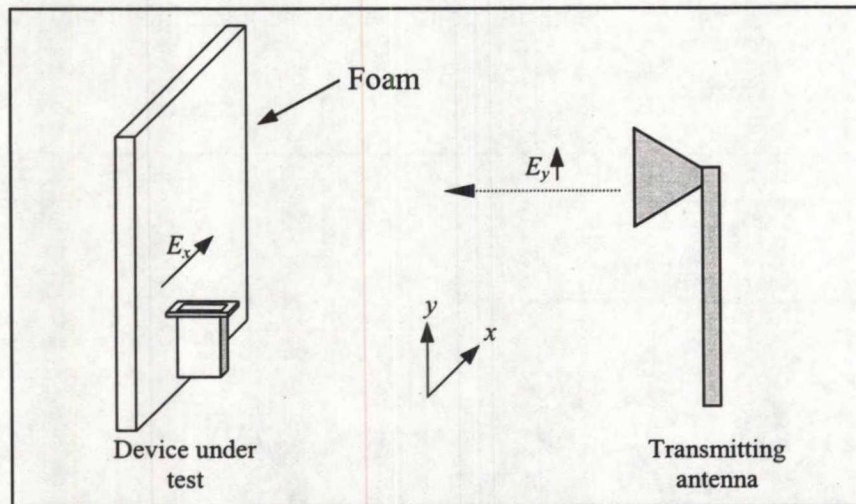


**Figure 4.11. E-plane cross-polarization test setup for feed pattern measurement.**

It is clear from Figure 4.10 that the feed is mainly responsible for the high cross-polarization around  $\pm 90^\circ$ , while the nulls at  $\pm 100^\circ$  are due to reflections on the frame. This implies that if a feed with no cross-polarization is used to illuminate the antennas, the dipole hologram would have a very low cross-polarization level.

Even though the dipole hologram has less gain than the continuous-strip case, it performs significantly better in terms of cross-polarization. The gain can be improved by increasing the number of dipole elements in the array, thereby reducing the gaps. Another great advantage over the continuous-strip case is the possibility to simulate quickly the H and E-plane pattern with **ARPS**. Nevertheless, the continuous-strip hologram is a very good antenna to work with in terms of characterizing this class of antenna's properties. Some efficiency considerations regarding this antenna are discussed in the following section.

## 4.2 Efficiency and Beam Squint Considerations

Even though the holographic antenna does not yet meet the high gain requirements, the results obtained so far validate the hologram concept and help to identify the areas that require further improvements, such as antenna efficiency. Various techniques can be used to increase the overall efficiency and these are summarized in the following paragraphs.

The first logical approach to increase the efficiency is to use an array of holograms. With this method, it is possible to increase the gain, eliminate the **B** and **S** lobes, and simultaneously intercept more energy from the feed with a corresponding reduction of spillover.

The efficiency can also be considerably improved with feeds other than the open waveguide. Before designing these new feeds, two issues must be considered: spillover and illumination efficiency. For instance the open waveguide has an H-plane half-power beamwidth of about  $60^\circ$ . Therefore, the spillover can be reduced using a horn with an H-plane beamwidth less than the open waveguide so as to focus all the energy onto the surface of the holographic antenna.

Regarding the illumination efficiency, the hologram requires a feed that can uniformly illuminate the entire surface of the antenna in the E-plane. The open waveguide has an E-plane half-power beamwidth of at least  $100^\circ$  which is more than enough for the  $90^\circ$  flared holographic antenna. However, by looking at the E-plane radiation pattern (and the H-plane also) of the open waveguide in Figure 4.12, the pattern is not quite uniform in the  $90^\circ$  beamwidth required for the



hologram. The bumps seen at broadside are probably a result of scattering on the metal edges outside the open aperture of the waveguide, shown in Figure 4.13.

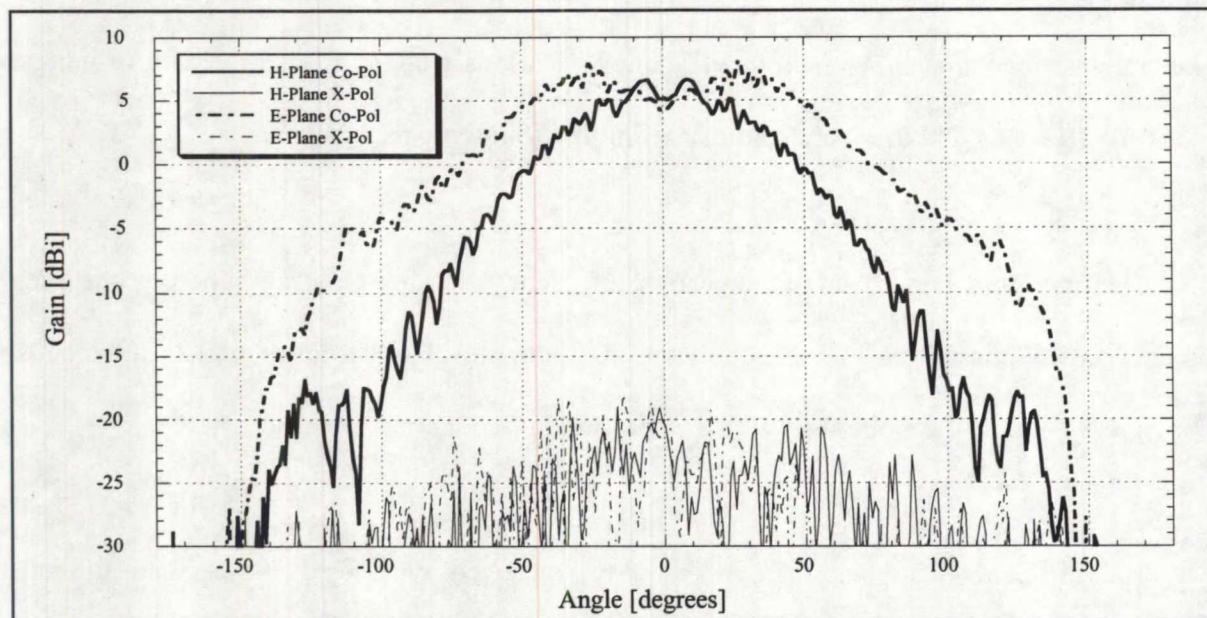


**Figure 4.12. Radiation pattern of the open waveguide.**

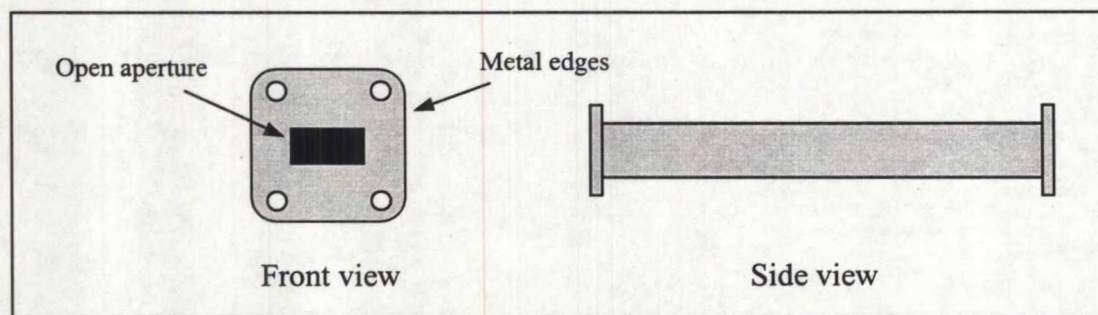


**Figure 4.13. Open waveguide.**

With other feeds, such as a pyramidal or sectoral horn, it is possible to get a smoother pattern and properly illuminate the hologram. Thus the feed must be designed such that it offers a uniform pattern in the E-plane cut and a narrow beamwidth in the H-plane. Note that although the pattern may be smooth within a certain beamwidth in the far-field, this may not be the case in

the near-field. The effect of the phase errors and the side lobe towards the feed on the near-field radiation pattern is unknown for either the open waveguide or the feed horns. Remember that the hologram is in the near-field region of the open waveguide and that the feed pattern in this region is not necessarily as shown in Figure 4.12. However, as a first order approximation, it can be assumed that if the far-field is uniform, so will be the near-field.

A second way to improve the illumination efficiency is by changing the shape of the antenna. The holographic antenna used so far has a flared angle of  $90^\circ$ , as shown in Figure 4.14 (a). It is possible to reduce this angle such that the gain variation of the illumination across the surface is reduced. However, to properly compare this new antenna with the previous case, the aperture size must be maintained by extending the height of the hologram resulting in a diamond-shaped holographic antenna illustrated in Figure 4.14 (b).

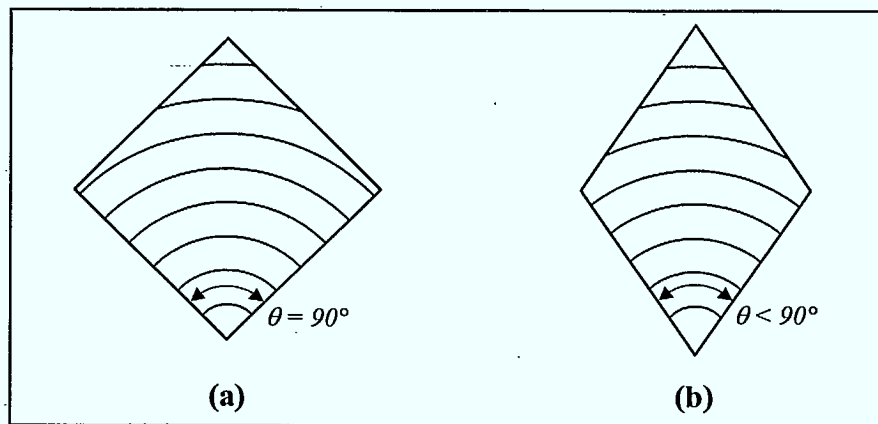


**Figure 4.14. Illumination efficiency**  
**(a) Square hologram (b) Diamond-shaped hologram.**

The diamond-shaped hologram should also offer a lower cross-polarization than the square one because fewer vertical components are reflected by the strips. Note that the number of rings in both antennas is the same.

Apart from the efficiency, the beam squint issue is also an important factor to consider. Based on the results, the beam scans further away from broadside in the positive direction (towards top of antenna) as the frequency increase. This implies the distance between the elements is too large or, equivalently, that at the desired frequency  $f_o = 30GHz$ , the guided wavelength is less than the free-space wavelength ( $\lambda_g < \lambda_o$ ). Because the microstrip lines are etched onto a dielectric surface, it is tempting to define the guided wavelength as:

$$\lambda_g = \frac{\lambda_o}{\sqrt{\epsilon_{r,eff}}}, \quad (4-2)$$

where  $\epsilon_{r,eff} = \epsilon_r$ . But because the dielectric slab is so thin, the effective dielectric constant is very close to air and therefore the guided wavelength will be slightly less than the free-space wavelength as described in section 3.2.1. The guided wavelength can be evaluated theoretically or from measured results using the beam peak value at the desired frequency. One must remember that even if the distance between the elements is correct at the desired frequency for broadside radiation, the antenna will still scan with frequency since the hologram behaves in the same manner as a traveling wave antenna.

Note that with **ARPS** it is possible to look at the effect of the beam squint on the radiation pattern by phasing each element in the dipole hologram appropriately. At the desired frequency, the phase of each element can be derived from (3-6) in Chapter 3 for a known beam peak angle  $\theta_s$ . Since for a large number of elements this analysis can be time consuming (phase changes with frequency), it is often convenient to simulate a linear array of 14 elements (the number of strips) instead of an array of 94 dipoles (the number of elements in the dipole hologram).

### 4.3 Design Procedure of a Holographic Antenna

Based on the validation of the holographic antenna and the efficiency considerations, the antenna is indeed functional but requires some improvements in order to satisfy the Ka-band specifications described in Chapter 1. From the discussion in the previous sections, it is now possible to establish a design procedure for the fabrication of holographic antennas. These design guidelines can be summarized by the following four steps:

- 1) Construct the hologram from the destructive interference pattern derived in Chapter 2. Note that the material must be properly selected such that loss, simplicity, and environmental issues are considered.
- 2) Select the size of hologram that would generate the desired gain.
- 3) Select a feed with the proper polarization (in this case the E-field must be parallel to the plane of the hologram) and that will efficiently illuminate the hologram.
- 4) Determine the focal point and set the distance between feed and hologram appropriately.

These design guidelines will be useful in the following chapter where various antennas are constructed based on the efficiency and beam squint considerations discussed in the previous section. Note that the different antennas will often be compared to the continuous-strip (or single-layer) hologram on Duroid 4003 tested in this chapter. Also, now that the hologram concept has been verified at microwave frequencies, the goal is now to increase the efficiency of holographic antennas.

## **CHAPTER 5**

### **Holographic Antenna Enhancement Techniques**

The holographic antenna concept has been validated at microwave frequencies in the previous chapter with little consideration for its operational efficiency. However, the efficiency issue cannot be disregarded if a holographic antenna is to be employed in any practical application. In this chapter, various techniques of efficiency enhancement will be presented. Other important issues including beam squint, return loss and antenna radiation characteristics will also be considered.

#### **5.1 Efficiency Enhancement Techniques**

As discussed in Chapter 4, there are several factors which affect the operational efficiency of a holographic antenna. These factors include: spillover and tapering losses, feed losses, and losses due to the radiation of the holographic antenna at other directions than broadside. Techniques that can be used to control the above factors are investigated in the following sections.

##### **5.1.1 Two-layer hologram for back lobe suppression**

The first technique considered for efficiency enhancement is the two-layer hologram described in Section 3.1.5 of Chapter 3. By properly phasing the two-layer hologram, radiation loss in undesired directions can be suppressed. Moreover, the two-layer hologram will reduce spillover loss by intercepting more energy from the feed. The two configurations illustrated in Figure 3.10 are investigated with the material characteristics described in Table 5.1.



**Table 5.1 General properties of two-layer holographic antennas**

Prototype	Dielectric	Dielectric constant	Dielectric thickness	Frequency of operation	Distance between plates
Two-layer hologram	Duroid 4003	$\epsilon_r = 3.38$	$t = 20\text{mils}$	$f_o = 30\text{GHz}$	$d_2 \approx 0.25\text{cm}$
Double-sided hologram	Duroid 3003	$\epsilon_r = 3.0$	$t = 60\text{mils}$	$f_o = 30\text{GHz}$	$d_2 = 0.14\text{cm}$

In the two-layer hologram, nylon spacers with a thickness of  $s = 0.2\text{cm}$  separate the two holograms (or plates). The thickness  $s$  was selected such that the distance between the strips is  $d_2 = \frac{\lambda_o}{4} \approx 0.25\text{cm}$  as shown in Figure 5.1 ( $t$  is the thickness of the dielectric). Note that to have a relative phase (defined in Section 3.1.1 of Chapter 3) of  $\beta_p = 90^\circ$ , the distance between the strips with respect to the feed must also be equal to  $d_1 = 0.25\text{cm}$ . The scattering fields of the two-layer hologram are in phase in the upper and right directions and are  $180^\circ$  out of phase in the down and left directions as described in Figure 3.11 of Chapter 3.

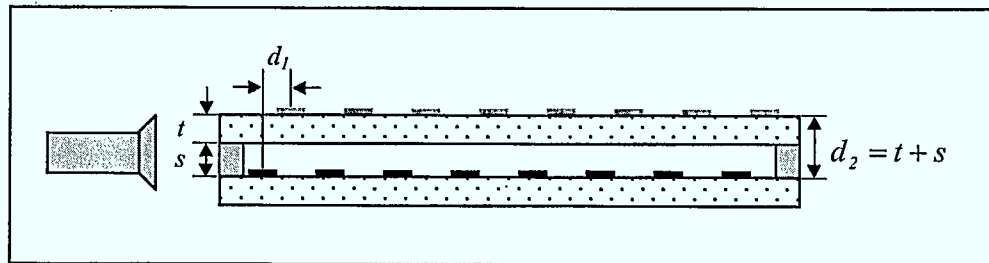


**Figure 5.1. Two-layer hologram with spacers.**

For the double-sided hologram, the dielectric was selected such that the distance between the strips is  $d_2 = \frac{\lambda_g}{4} = 0.144\text{cm} = 56.8\text{mils}$ , where  $\lambda_g = \frac{\lambda_o}{\sqrt{\epsilon_r}}$ . Based on Table 5.1 the dielectric's thickness  $t$  is  $60\text{mils}$ , which includes the thickness of the copper on both sides of the dielectric. Removing the copper (the antenna has no ground plane) reduces the dielectric's

thickness close to the desired value. For a relative phase of  $\beta_p = 90^\circ$ , the distance between the strips with respect to the feed was chosen as  $d_1 = 0.25\text{cm}$ . This second design offers less control compared to the two-layer structure since it is not possible to change the distance between the two layers once the strips are etched on the substrate.

The measured H-plane radiation patterns of both antennas are shown in Figure 5.2 for the two-layer hologram and Figure 5.3 for the double-sided case. The pattern of the single-layer hologram (prototype 3 in the previous chapter) is also included for comparison. It should be noted that the tip of the holograms is inside the open aperture of the open waveguide feed for all cases.

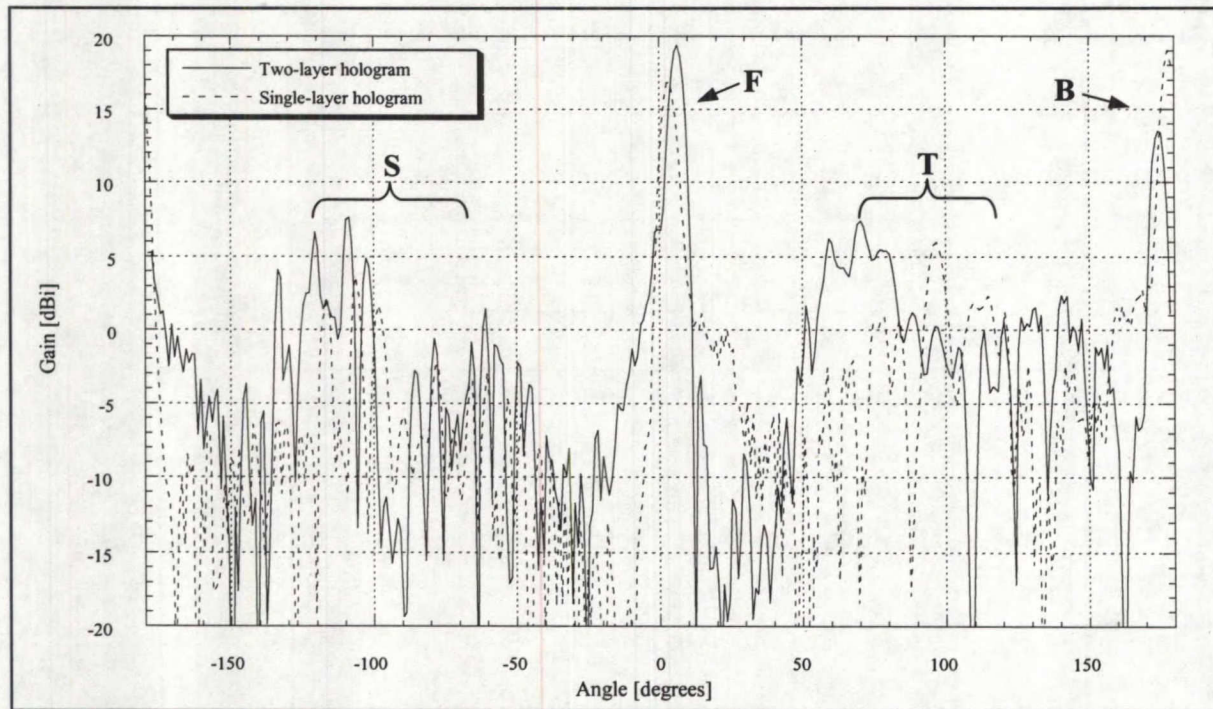


**Figure 5.2.** H-plane radiation pattern of the two-layer hologram ( $f = 30\text{GHz}$ ).



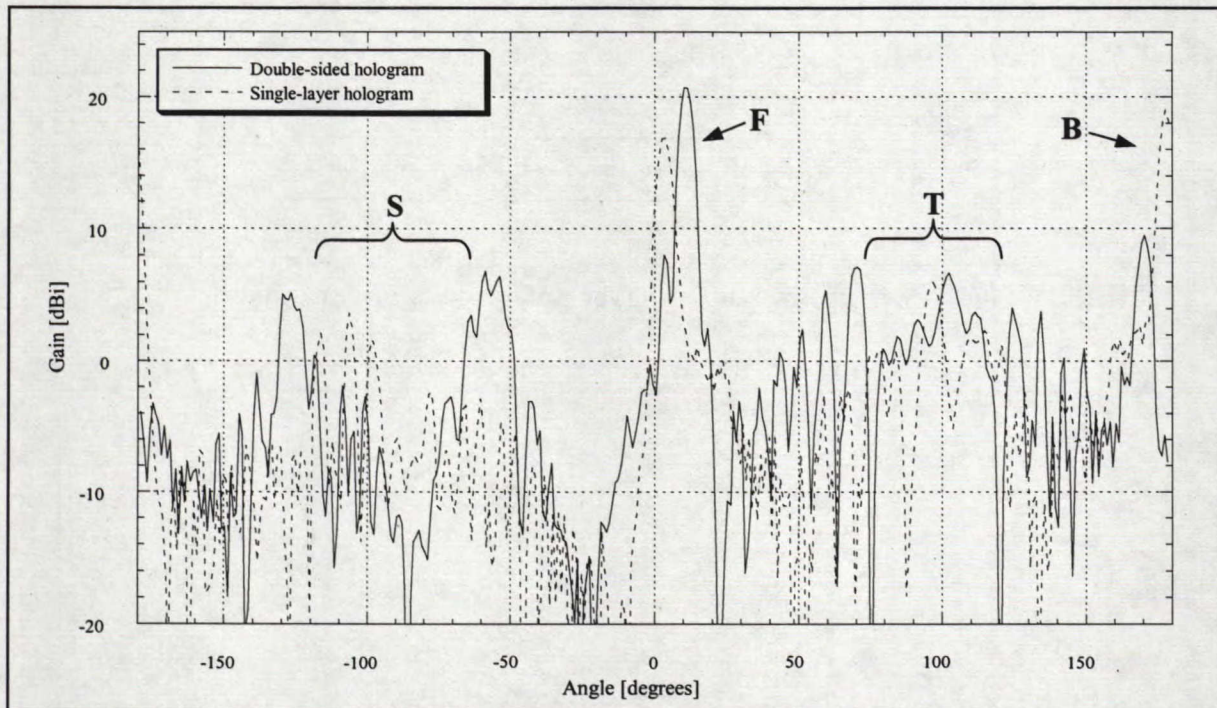


**Figure 5.3. H-plane radiation pattern of the double-sided hologram ( $f = 30\text{GHz}$ ).**

For the two-layer case separated by spacers, a gain increase less than  $0.5\text{dB}$  is observed at the desired frequency and the back lobe is suppressed by about  $5.5\text{dB}$ . With the double-sided hologram the gain increased by  $1.7\text{dB}$  and the back lobe **B** is suppressed by more than  $10\text{dB}$  compared to the front lobe **F**. Also, the **S** lobe level (towards feed) at  $-90^\circ$  is reduced and the **T** lobe level (top of antenna) slightly increased compared to the single-layer hologram, as expected.

In the first configuration, the distance between the two holographic plates was varied and the patterns re-measured for the case illustrated in Figure 5.4 where the dimensions  $s$ ,  $t$  and  $d_1$  are approximately the same as in Figure 5.1. A gain increase of more than  $4\text{dB}$  was observed and the back lobe was completely suppressed at  $f = 28\text{GHz}$ . The radiation pattern is shown in Figure 5.5.



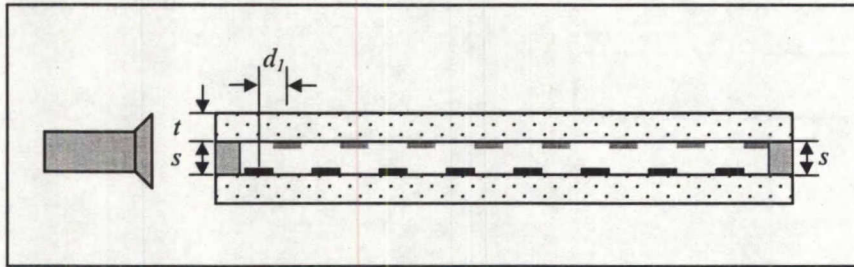


Figure 5.4. Optimized two-layer hologram configuration.

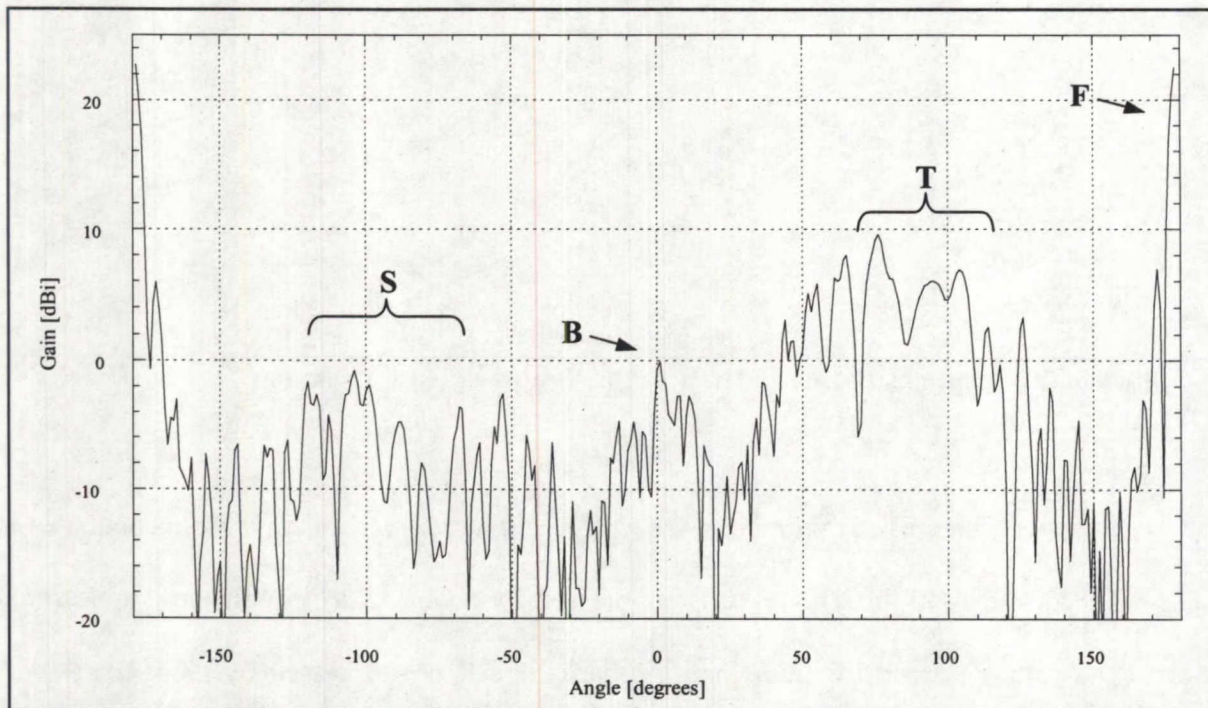
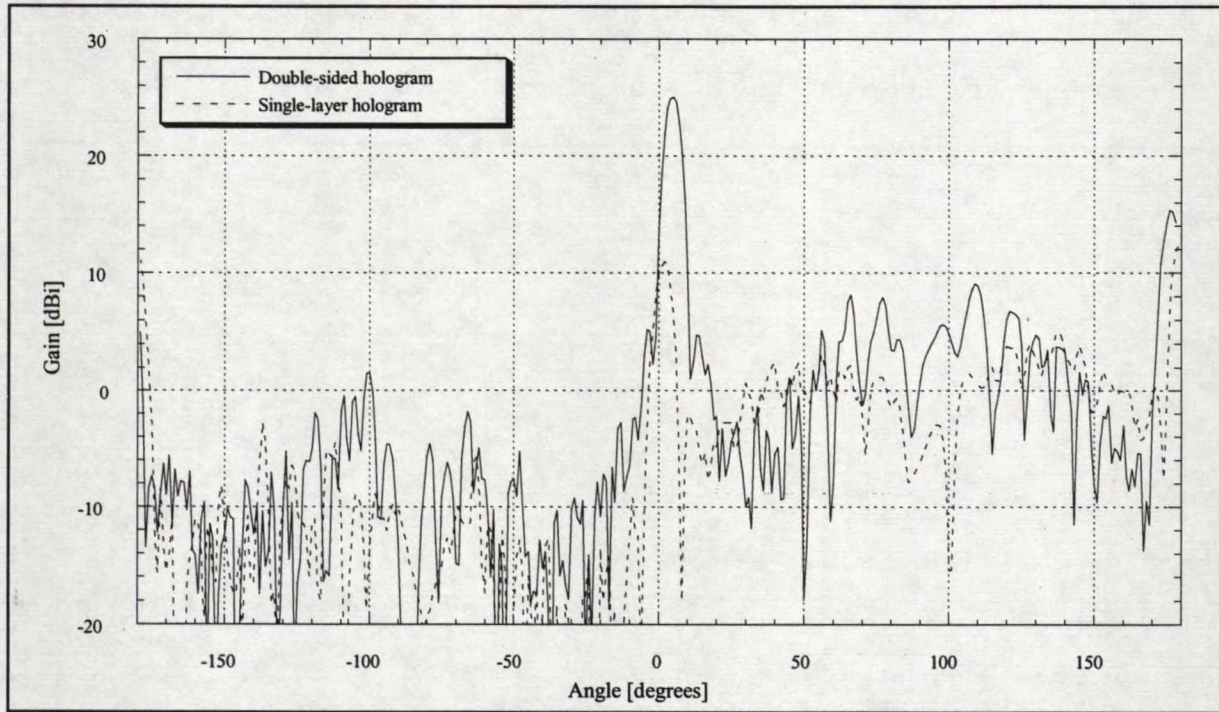


Figure 5.5. H-plane radiation pattern of optimized two-layer hologram ( $f = 28\text{GHz}$ ).

The measured gain of this antenna is  $23.5\text{dB}$  at  $f = 28\text{GHz}$  which corresponds to an efficiency of  $20.4\%$  as compared to less than  $5\%$  for the single-layer hologram. At  $f = 30\text{GHz}$  the gain is  $19.36\text{dB}$  ( $6.9\%$  efficiency) and the back lobe is suppressed by at least  $10\text{dB}$ . Note, from Figure 5.5, how low the S lobe level is compared to the previous cases illustrated in Figure 5.2. Since the two-layer hologram performs better at frequencies below the design frequency,



the radiation patterns for the double-sided structure were evaluated at other frequencies. The best case is shown in Figure 5.6.



**Figure 5.6. H-plane radiation pattern of double-sided hologram ( $f = 28\text{GHz}$ ).**

The gain at  $f = 28\text{GHz}$  for the double-sided hologram antenna is  $25.03\text{dB}$ , which corresponds to an efficiency of  $29.05\%$ . The back lobe, however, is only suppressed by  $9.6\text{dB}$ . Note that for the two-layer antennas (both configurations), the focal point (distance between feed and hologram) was not originally optimized for gain. Therefore, the double-sided structure was tested a second time where the focal point was moved slightly to another location and a gain of  $23.34\text{dB}$  at  $f = 30\text{GHz}$  was obtained which translates to an efficiency of  $17.15\%$  (the gain at  $f = 28\text{GHz}$  for this case is  $24.57\text{dB}$ ). This corresponds to a gain increase of  $2.64\text{dB}$  compared to the unfocused case in Figure 5.3.



To complete the above measurements, the return loss of the two-layer configuration and the single-layer hologram was measured and compared. As mentioned in the previous chapter, the lobe towards the feed (S lobe) in the single-layer hologram can affect the return loss. To verify this statement and show that indeed the two-layer structures suppress this undesired side lobe, the return losses for the three configurations are shown in Figure 5.7.

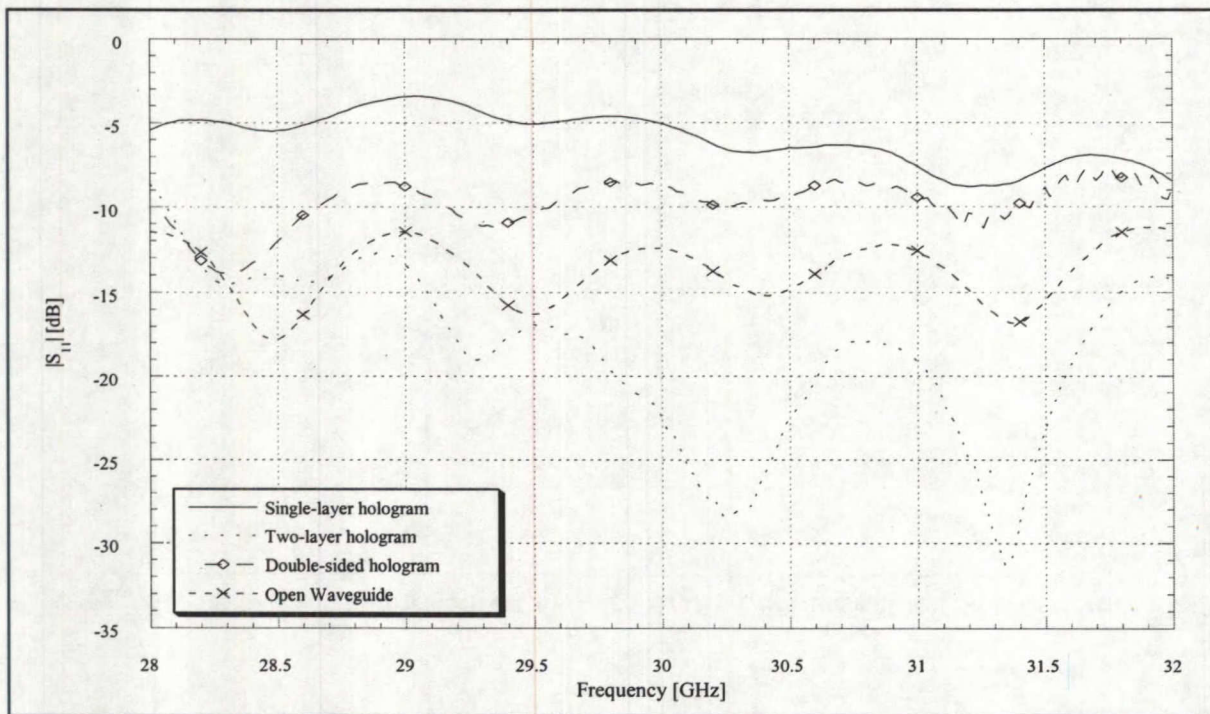


**Figure 5.7. Measured  $|S_{11}|$  of feed waveguide.**

For the return loss measurement, the feed was placed at the location which results in the maximum gain of the single layer hologram (tip of antenna is inside open aperture of the open waveguide). From Figure 5.7, the open waveguide by itself is well matched across the entire frequency range of interest. When the single-layer hologram is added, the return loss is degraded. However, the two-layer structure of Figure 5.4 significantly improves the return loss to a level which is a better match than the feed by itself. It is possible with the single-layer

hologram to obtain a return loss similar to the two-layer case by varying the distance between the open waveguide and the hologram. However, at this feed location, the hologram is not properly illuminated and the gain drops significantly. Therefore it would be interesting to investigate new feeds with different beamwidths than that of the open waveguide for a potential improvement of the gain and the return loss.

### 5.1.2 Feed horn integration for illumination efficiency improvement

As discussed in Chapter 4, to improve the spillover and the illumination efficiency, the requirements for a new feed are half-power beamwidths less than  $60^\circ$  in the H-plane and greater than  $90^\circ$  in the E-plane. To obtain this “fan-shaped” beam in the desired plane (and a broad beam in the other plane), the H-plane sectoral horn was considered as the feed. Three horns were fabricated and tested based on the design guidelines in [19]. The specifications along with the measured radiation patterns of each horn are discussed in Appendix D. A fourth horn, which is a pyramidal horn with H and E-plane beamwidths of  $30.88^\circ$  and  $30.53^\circ$ , was also investigated as a potential feed for the holographic antenna. The dimensions of the pyramidal horn along with the radiation patterns are also given in Appendix D.

The single-layer holographic antenna was tested with the H-plane sectoral horn #1 ( $20^\circ$  H-plane beamwidth), the H-plane sectoral horn #3 ( $37^\circ$  H-plane beamwidth), and the pyramidal horn. The measured H-plane radiation patterns at  $f = 30\text{GHz}$  are presented in Figures 5.8 to 5.10 and are summarized in Table 5.2 where the highest side lobe level for both the T and S lobes are included. The results also include the pattern of the single-layer holographic antenna with the open waveguide (OWG) feed for comparison purposes. The distance between the horns



and the hologram was kept the same as the distance between the open waveguide and the single-layer hologram. This means the feed location may not be optimal.

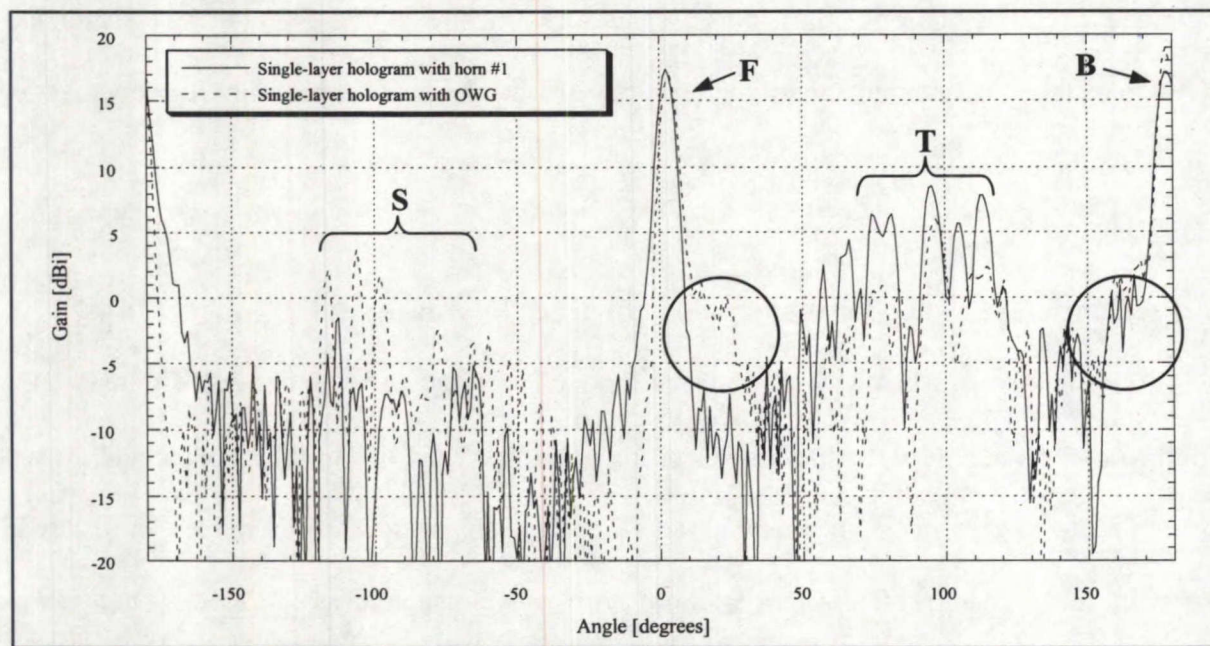


**Figure 5.8. Radiation pattern of the holographic antenna with feed horn #1.**

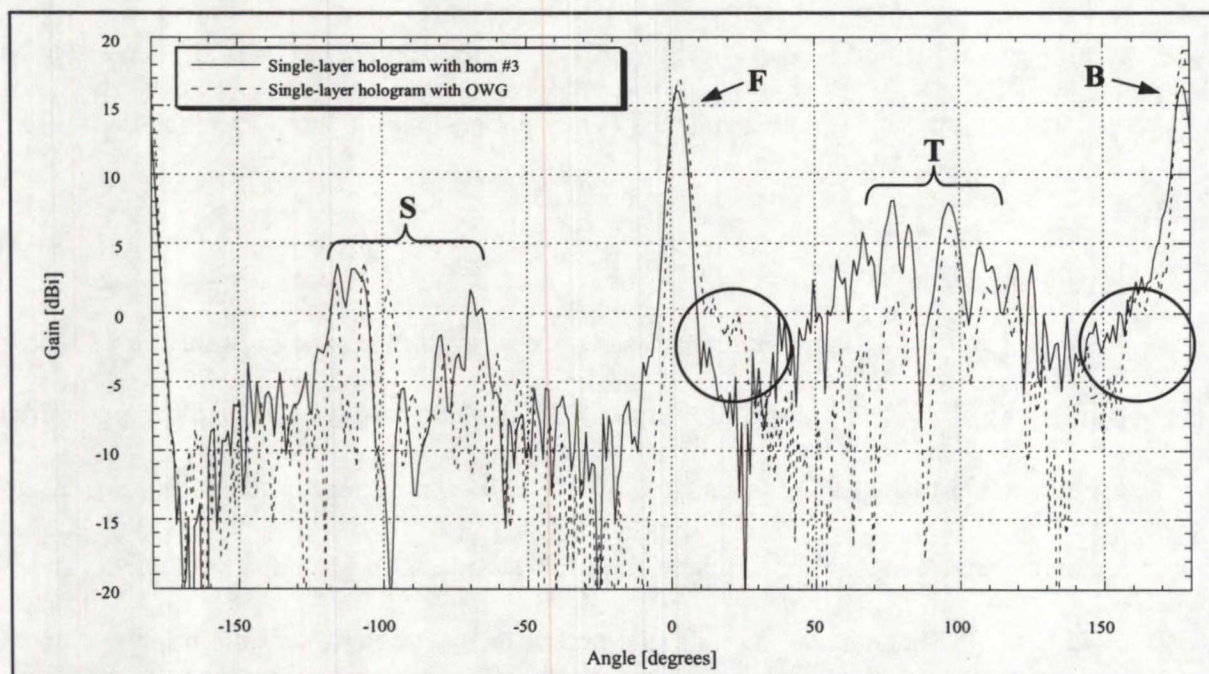


**Figure 5.9. Radiation pattern of the holographic antenna with feed horn #3.**



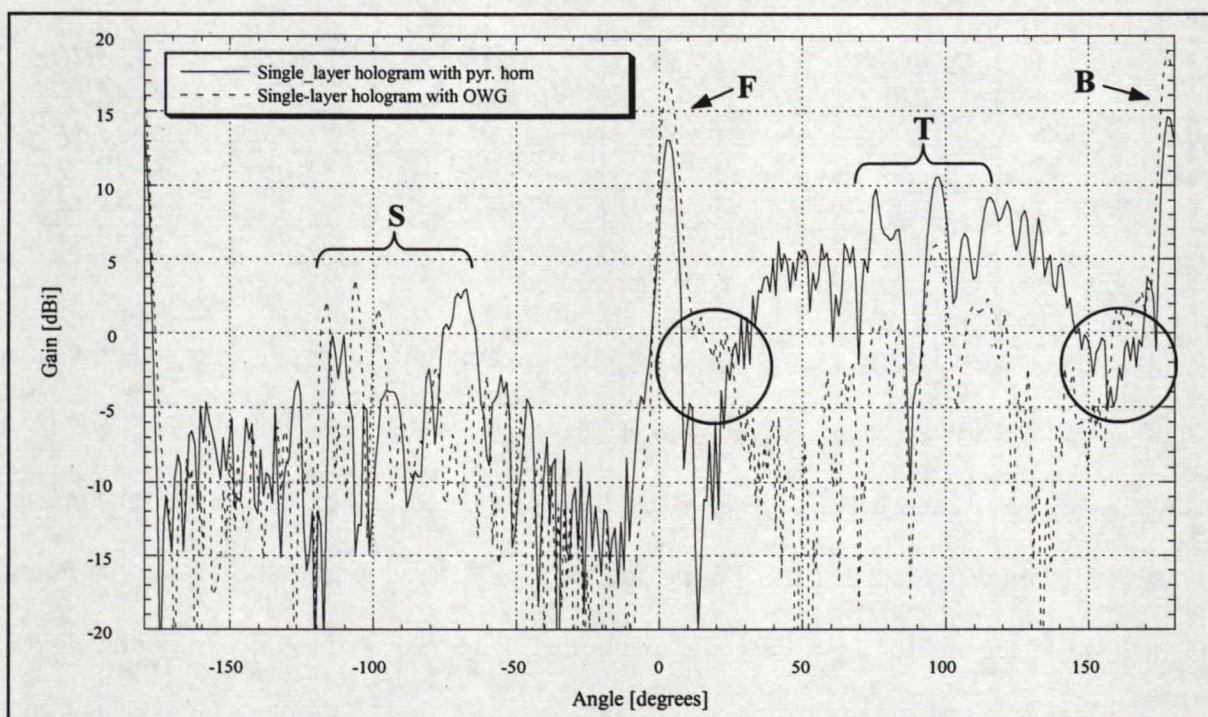


**Figure 5.10. Radiation pattern of the holographic antenna with pyramidal horn.**

**Table 5.2 Radiation pattern results at  $f = 30\text{GHz}$**

Feed	Gain [dB]	Beam peak [degrees]	T lobe level [dB]	S lobe level [dB]
Open waveguide	19.01	2.31°	5.99	3.66
Sectoral horn #1	17.37	2.61°	7.84	-1.47
Sectoral horn #3	16.42	2.61°	7.92	3.5
Pyramidal horn	14.57	2.38°	10.62	3.0

In general, the T lobe levels of the new feed horns are considerably higher than that of the open waveguide case. The phase errors, however, noticeable in the circled regions are usually not as dominant with the feed horns compared to the open waveguide. Since the gains illustrated in Table 5.2 are quite different from each other, Table 5.3 lists the gain at other frequencies to see whether the hologram with the new feed horns performs better.



**Table 5.3 Gain results**

Feed	28.0GHz [dB]	29.0GHz [dB]	30.0GHz [dB]	31.0GHz [dB]	32.0GHz [dB]
Open waveguide	12.24	10.96	19.01	18.36	18.81
Sectoral horn #1	11.29	13.02	17.37	18.06	19.29
Sectoral horn #3	10.44	11.86	16.42	17.09	18.44
Pyramidal horn	10.22	16.56	14.57	17.51	19.62

Based on Table 5.3, the holograms offer a better gain at higher frequencies where values are quite similar between the different feeds. At lower frequencies, however, there is a considerable gain variation between each case. It might be possible to establish a relationship between these gain differences, the matching and the type of feed used by observing the return loss which was measured for all of the cases mentioned. The measured return losses of a single-layer hologram using different feeds are illustrated in Figure 5.11. Again the location of the feed with respect to the holographic plate is the same as in the antenna pattern measurement tests (inside the horns).

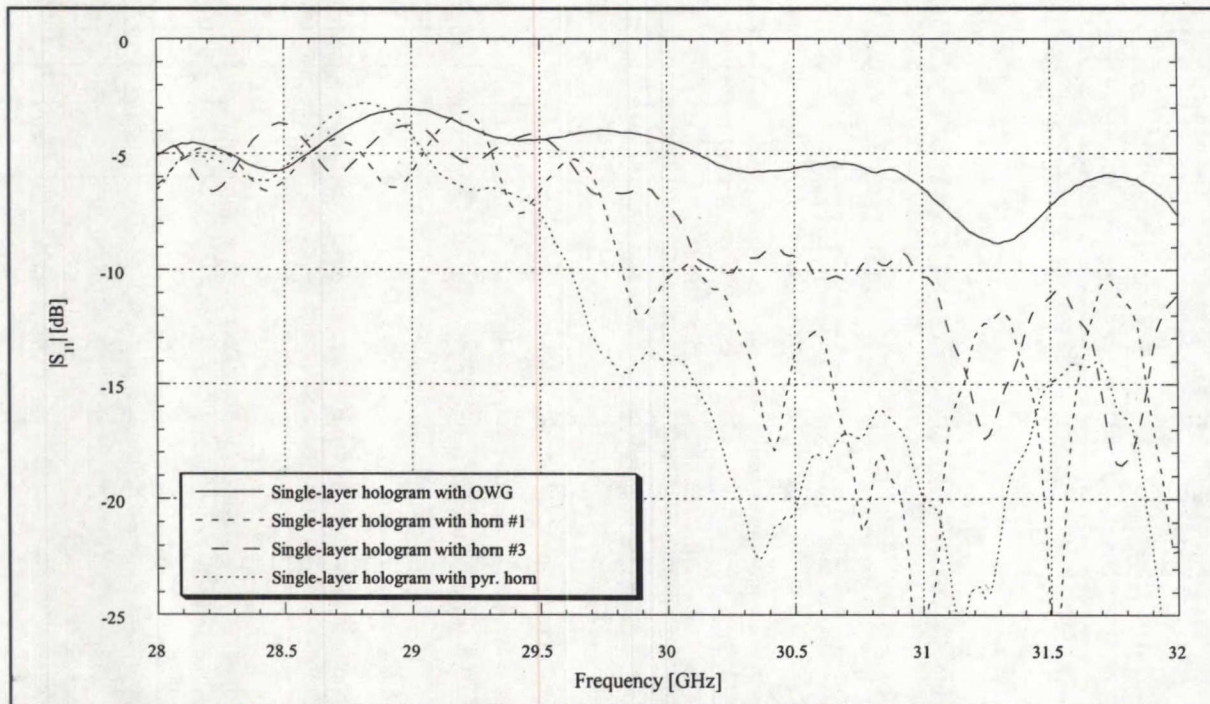


**Figure 5.11.  $|S_{11}|$  of single-layer hologram with different feeds.**

Over a wide frequency range the pyramidal horn offers a better match than the other feeds. As mentioned before, varying the feed's distance from the antenna changes the return loss. In fact this focusing effect is explored in more detail in the next section.

### 5.1.3 Evaluation of the focal points of a feed horn for phase error reduction

With the holographic antenna, it is very important that the feed is properly focused onto the hologram in order to reduce phase errors. With a feed horn it is difficult to establish a focal point since there exists two possible equivalent point sources from which the waves are generated. These two point sources are known as the apex (equivalent point source in the near-field) and the phase center (equivalent point source in the far-field) and are described in Appendix D for the pyramidal horn. To determine which point source the hologram should be focused on, two holograms, one focused on the apex and the other on the phase center, were designed and tested.

The general concept is to generate two sets of holograms such that for each set the conducting strips on the dielectric matches the rings of the spherical wave generated by the corresponding point sources. Because the holographic plate is oriented in the E-plane, only the E-plane apex and phase center listed in Table D.4, in Appendix D, are considered. The radius of the first conducting strips is found based on the position of the point source with respect to the hologram plate as shown in Figure 5.12.

Based on Figure 5.12 (a) the first ring has a radius of  $L_a$  and from Figure 5.12 (b) the radius is  $L_p$ . The conducting strips following the first strip have for the first case a radius of

$L_{a,n} = L_a + (n - 1)\lambda_o$  and for the second case  $L_{p,n} = L_p + (n - 1)\lambda_o$ , where  $n = 2, \dots, N$ , and  $N$  is the number of strips on the antenna.

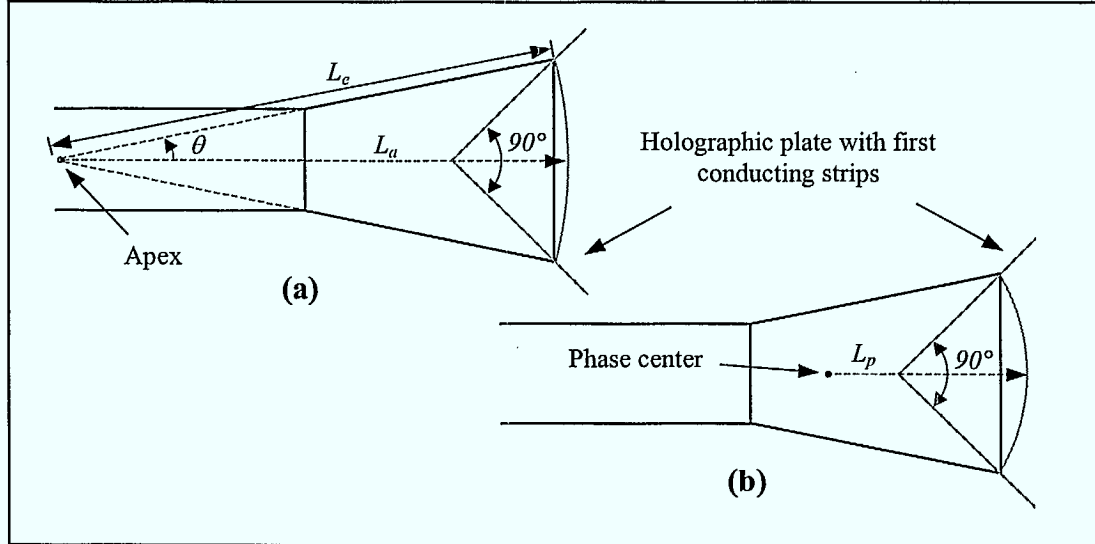


**Figure 5.12. Hologram generated from two point sources**  
**(a) E-plane apex (b) E-plane phase center.**

When testing the antennas, the pyramidal horn feed's position with respect to the holograms must be exactly as illustrated in Figure 5.12. Note that for the pyramidal horn,  $L_a = 1.56cm$  and  $L_p = 0.9cm$ .

On Figure 5.13 are plotted the radiation patterns at  $f = 30GHz$  of the holographic antenna focused at two different locations of the pyramidal horn along with a non-focused case. The non-focused case is simply the holographic plate used in all the previous tests where the tip of the antenna is at the edge of the open aperture of the pyramidal horn.



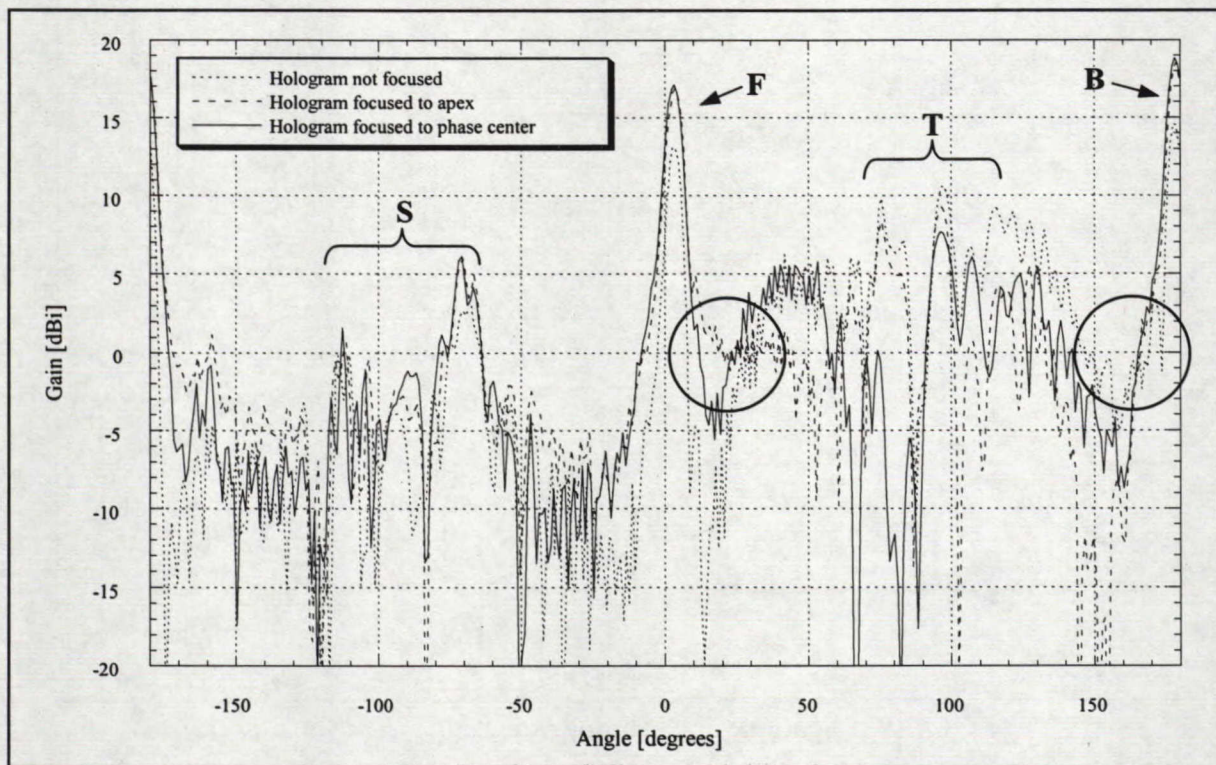


**Figure 5.13. Radiation pattern of single-layer hologram at different focal points.**

The radiation pattern results are summarized in Table 5.4 where the highest side lobe level for both the T and S lobes are included. The return loss was also measured and is shown in Figure 5.14. All the antennas were fabricated on Duroid 4003 with a dielectric thickness of 20mils.

**Table 5.4 Radiation pattern results**

Pyramidal horn	Gain [dB]	Beam peak [degrees]	T lobe level [dB]	S lobe level [dB]
Non-focused	14.57	2.47°	10.62	3.00
Focused on apex	18.51	1.44°	9.27	5.97
Focused on phase center	18.83	1.76°	7.67	6.1



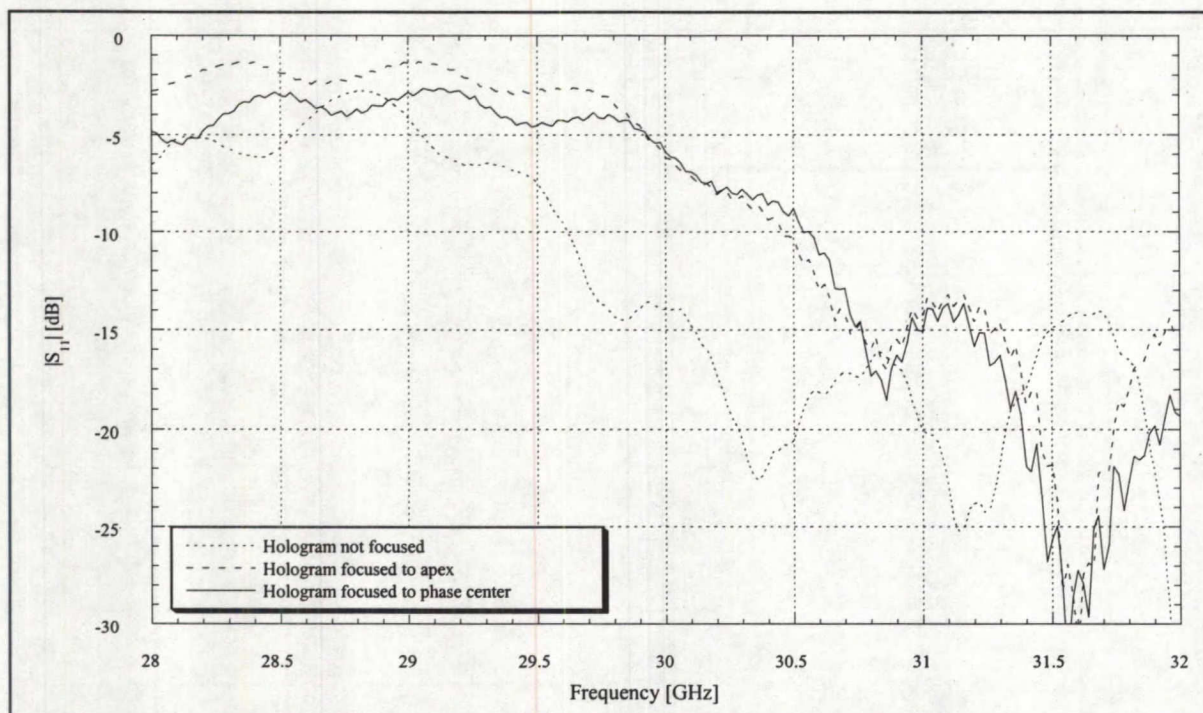


**Figure 5.14.**  $|S_{11}|$  of single-layer hologram at different focal points.

In general the radiation patterns are similar except for the gain level and the beam width of the front and back lobes. The holograms focused on the apex and the phase center show slightly less spillover at the tip of the antenna compared to the non-focused case by looking at the T lobe. With the hologram focused on the two new point sources, the tip of the hologram is about  $0.85\text{cm}$  inside the open aperture of the horn. Also, the non-focused hologram generally offers a better return loss than the apex and the phase center cases.

#### 5.1.4 Diamond-shaped hologram

As discussed in Section 4.2 of Chapter 4, the illumination efficiency can potentially be improved by changing the shape of the holographic plate instead of changing the feed. Referring to Figure 4.14 in Chapter 4, a diamond-shaped hologram with an angle of  $\theta = 70^\circ$  was



constructed on Duroid 4003 with a thickness of 20mils. This angle value was selected based on the E-plane beamwidth of the sectoral horns. The position of the feed with respect to the holographic plate was not optimized for gain but rather positioned at the same location as the square-shaped hologram (referred to also as the single-layer or continuous-strip hologram) for comparison. The radiation patterns of both the square and diamond-shaped holograms are plotted in Figure 5.15 where the feed is the open waveguide.

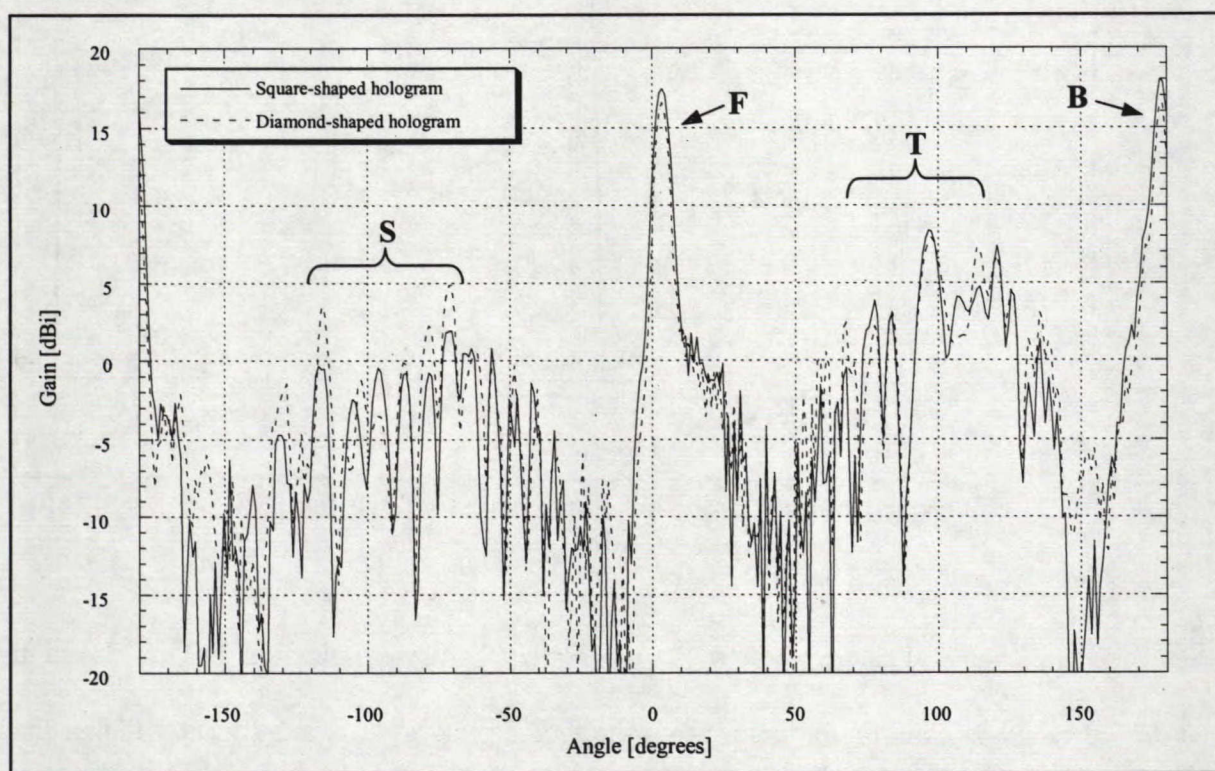


**Figure 5.15. H-plane radiation pattern of diamond-shaped hologram with open waveguide feed ( $f = 30\text{GHz}$ ).**

Based on the above figure, the two patterns are quite similar except for a slight increase of the S lobe with the diamond-shaped antenna. The gain of the diamond-shaped hologram is about 1.4dB less than the square-shaped hologram. Since the diamond-shaped hologram should provide a better cross-polarization than the square one, the E-plane cross-polarization was



measured and is shown in Figure 5.16. Because the beam peak scans with frequency and it is near broadside at  $28\text{GHz}$ , the cross-polarization is shown at this frequency only.

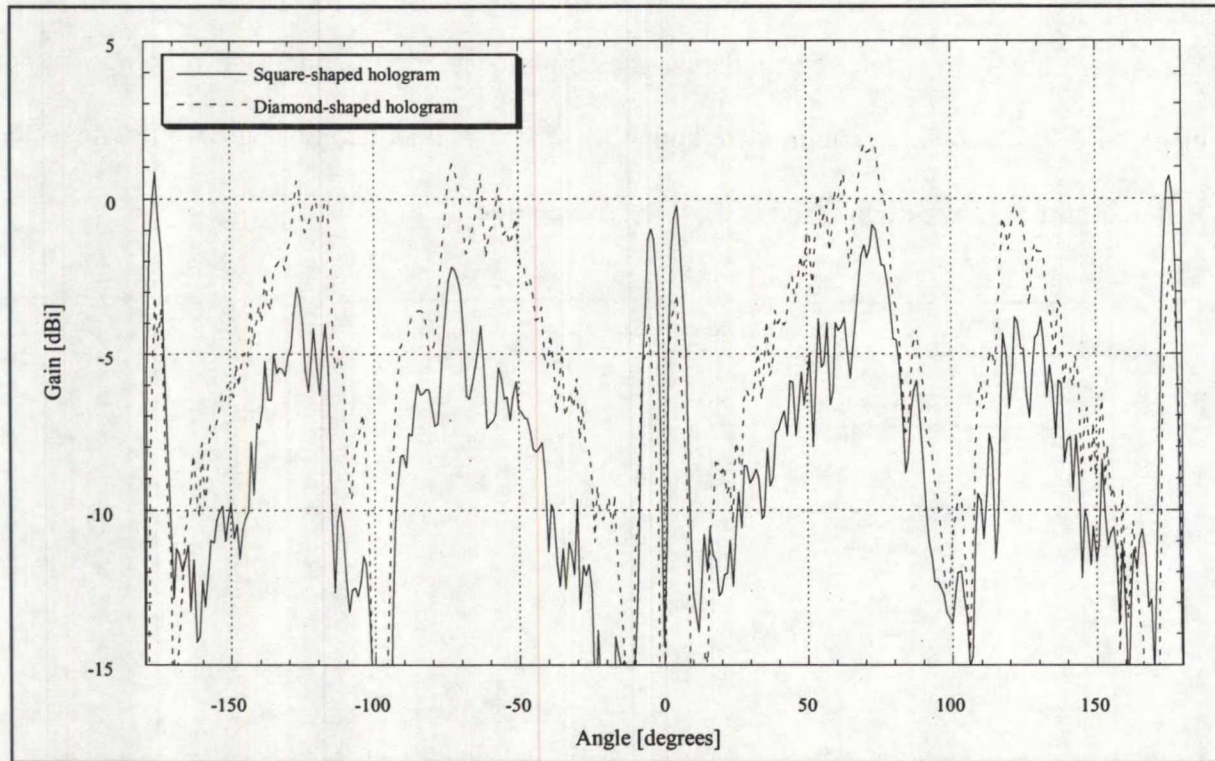


**Figure 5.16. E-plane cross-polarization radiation pattern of diamond-shaped hologram with open waveguide feed ( $f = 28\text{GHz}$ ).**

With the diamond-shaped hologram, the E-plane cross-polarization has improved by about  $3\text{dB}$  at broadside, but the radiation from the feed around  $\pm 90^\circ$  is significantly higher than the square-shaped antenna which indicates that less energy is intercepted. The effects of the illumination of the diamond-shaped hologram and the square antenna are also compared with the sectoral horn #3 as a feed. This horn has a smaller beamwidth than the open waveguide and is less effective in illuminating the square-shaped hologram. The H-plane patterns are shown in Figure 5.17.



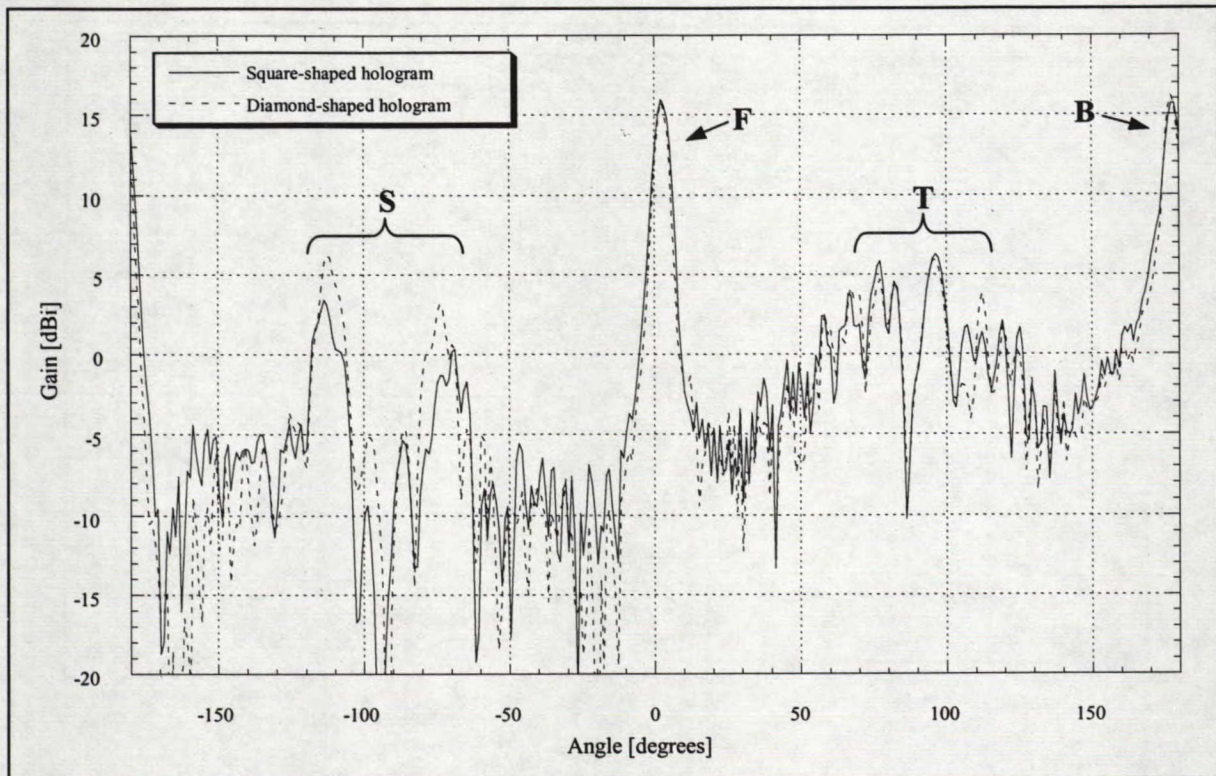


**Figure 5.17. H-plane radiation pattern with horn #3 ( $f = 30\text{GHz}$ ).**

Again, the patterns are quite similar and the gain of the diamond-shaped hologram is only  $0.25\text{dB}$  less than the square-shaped antenna. However, for frequencies greater than  $30\text{GHz}$ , the diamond-shaped hologram offers a gain increase between  $0.5\text{dB}$  and  $1\text{dB}$  compared to the square-shaped hologram. Also, it can be observed that smaller phase errors are present in the front and back lobes with the diamond-shaped antenna, as seen from better collimated patterns. Since the diamond-shaped hologram usually shows higher sidelobes (the S lobes) than the square antenna indicating more reflected energy to the feed horn, one should expect a worse return loss with this antenna. The return losses were measured and are compared in Figure 5.18 where the tips of the holograms are inside the open waveguide feed aperture.



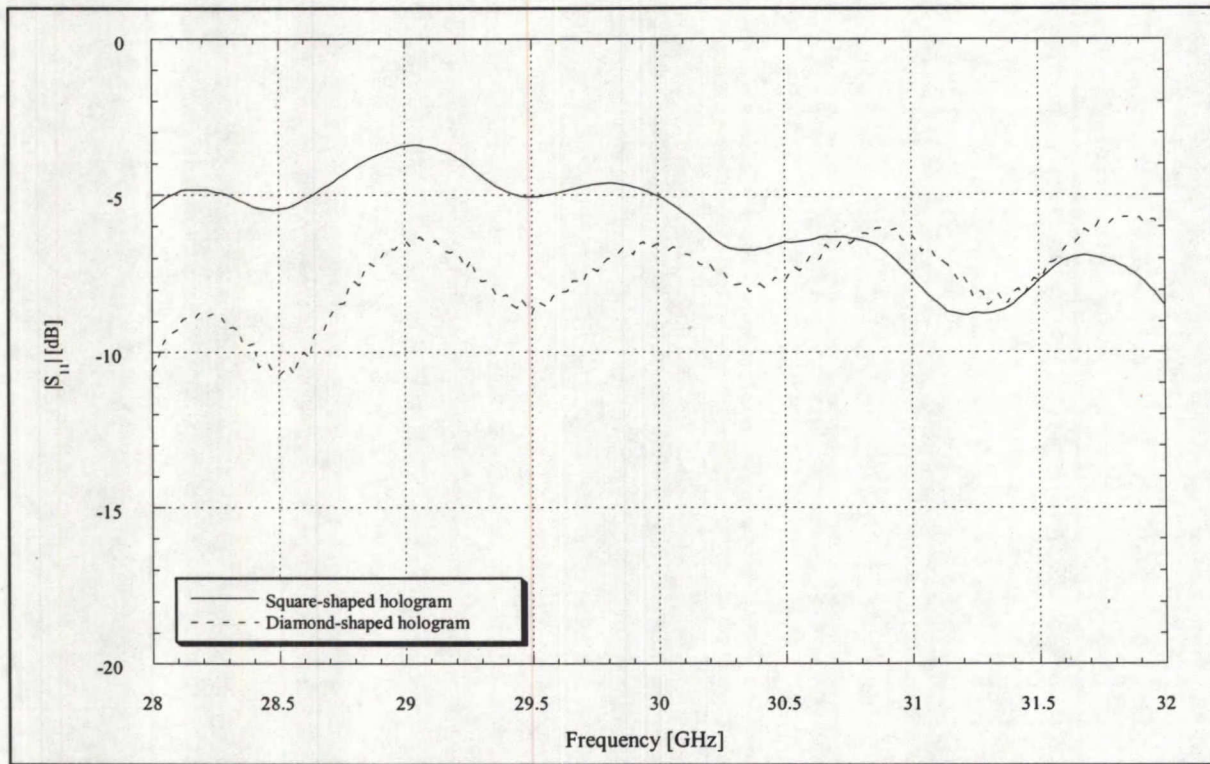


**Figure 5.18.  $|S_{11}|$  of the diamond-shaped and square-shaped hologram.**

At lower frequencies ( $f < 30.7\text{GHz}$ ), the diamond-shaped hologram offers a better return loss than the square-shaped antenna implying that the tapered tip of the diamond-shaped hologram is more effective in reducing the mismatch. The return loss was also evaluated in the case where the tip of the hologram is located at the tip of the open aperture instead of inside the feed. As the feed gets further away from the hologram, the return loss improves as shown in Figure 5.19. Generally, the square-shaped hologram offers a better match than the diamond-shaped antenna since it has a lower S lobe. Note that even if the return loss is better, the gain of the antennas decreases as the feed gets further away from the holographic plates as a result of more phase errors arising from an off-focal point feed. In the next section, the effects of



changing the width of the conducting strips on the radiation pattern, the return loss, and illumination efficiency are investigated.

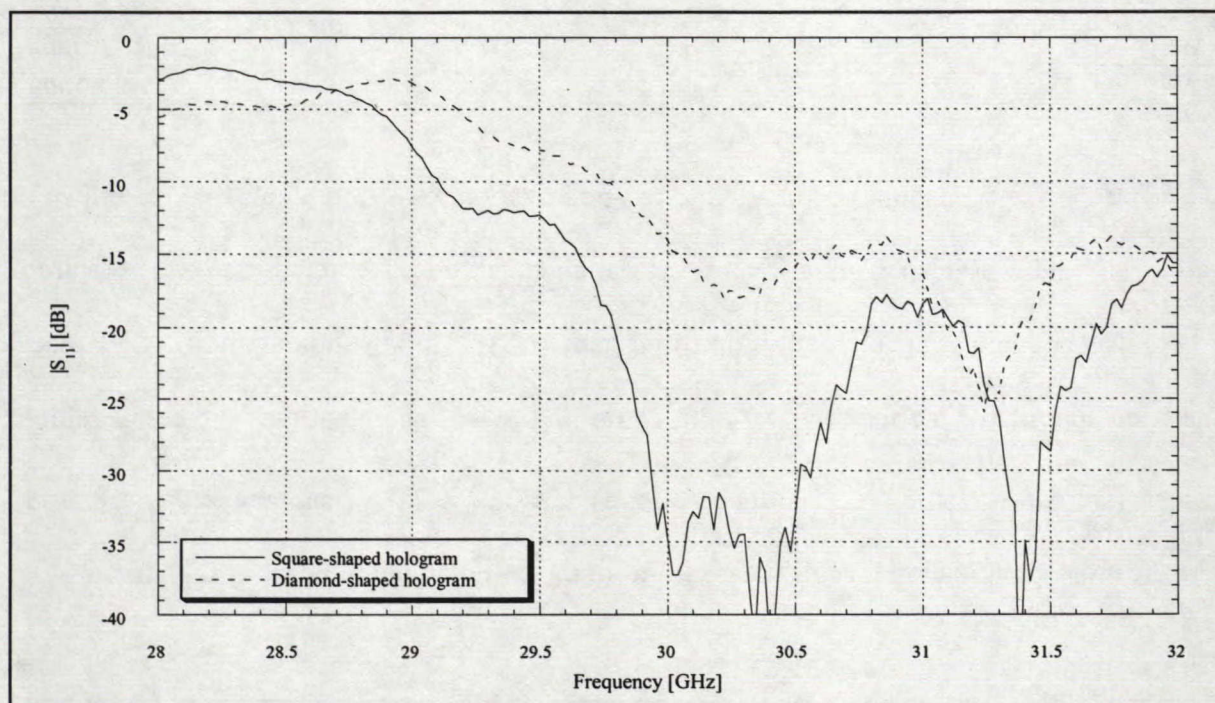


Figure 5.19.  $|S_{11}|$  of diamond-shaped and square-shaped holograms at second focal point.

### 5.1.5 Microstrip line width investigations

As mentioned in Chapter 4, the width of the conducting strips on the holographic antenna was selected to be as thin as possible. This choice was based on the destructive pattern derived in Chapter 2. Due to fabrication limitations, the narrowest width is *10mils* which corresponds to *0.254mm*. Because the width cannot be etched any smaller (unless a more expensive process is used to etch the lines onto the dielectric) the effect of wider strips on the performance of the antenna was investigated. Three other holographic antennas with the conducting strip widths described in Table 5.5 were designed and tested. The conducting strips are still separated from centre to centre by a distance of  $d = \lambda_o$ .



**Table 5.5 Holographic antenna with different strip widths**

Prototype	Dielectric	Dielectric constant	Dielectric thickness	Frequency of operation	Width of microstrip lines
W1	Duroid 4003	$\epsilon_r = 3.38$	$t = 20\text{mils}$	$f_o = 30\text{GHz}$	$w = 0.254\text{mm}$
W2					$w = 0.5\text{mm}$
W3					$w = 1.0\text{mm}$
W4					$w = 1.5\text{mm}$

The H-plane co-polarization and cross-polarization radiation patterns are shown in Figures 5.20 and 5.21 respectively. Note that the antennas' location relative to the aperture of the open waveguide was again not optimized for gain. Instead, all the hologram tips were placed at the open aperture of the feed ( $f_p = 0$  based on Figure 4.2) such that they are comparable in terms of gain and pattern. The results of Figures 5.20 and 5.21 are summarized in Table 5.6 where the cross-polarization level is measured from the co-polarization beam peak value.

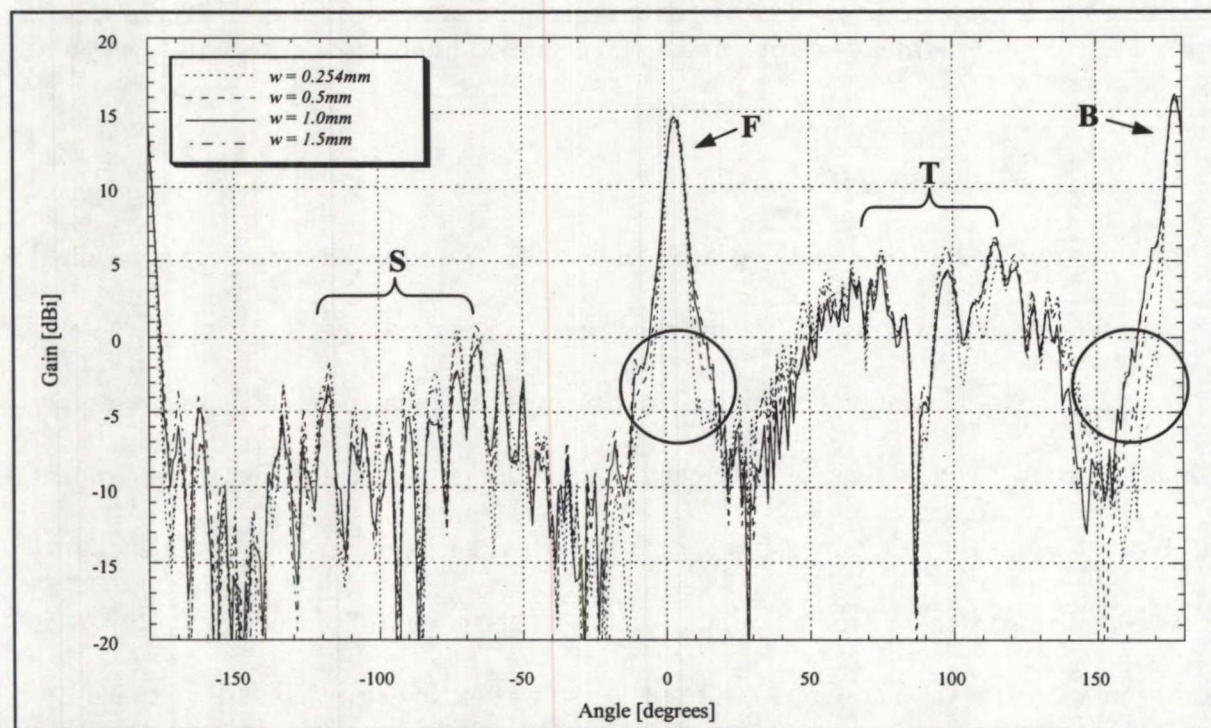


**Figure 5.20. H-plane co-polarization radiation pattern for varying the hologram strip widths ( $f = 30\text{GHz}$ ).**



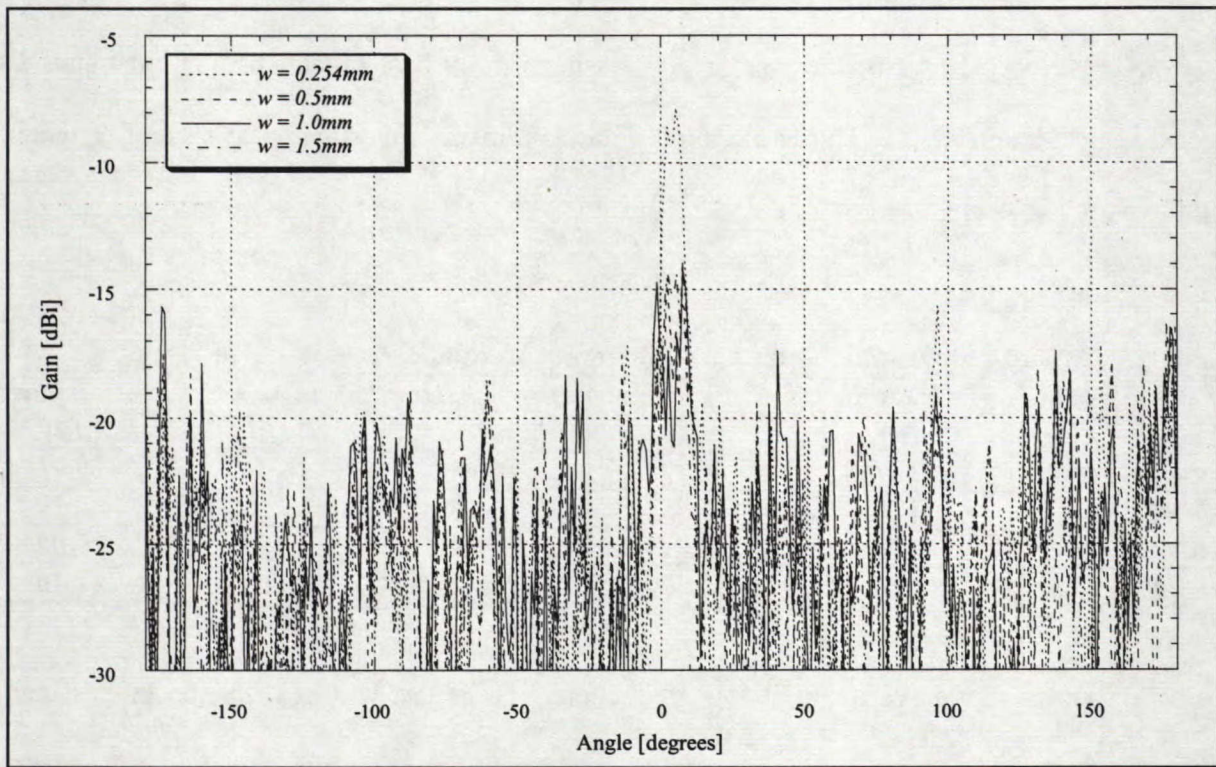


Figure 5.21. H-plane cross-polarization radiation pattern for varying the hologram strip widths ( $f = 30\text{GHz}$ ).

Table 5.6 Varying the hologram strip widths test results at  $f = 30\text{GHz}$

Prototype	Gain [dB]	Beam peak [degrees]	Cross-polarization [dB]
$w = 0.254\text{mm}$	16.15	$2.40^\circ$	-23.97
$w = 0.5\text{mm}$	16.16	$2.40^\circ$	-30.72
$w = 1.0\text{mm}$	15.92	$2.62^\circ$	-30.10
$w = 1.5\text{mm}$	16.12	$2.63^\circ$	-30.00

In general the radiation patterns are quite similar and all three antennas offer approximately the same gain. The gain could have been higher if the antennas were focused properly. The only noticeable difference at the desired frequency is the beamwidth of the front and back lobes indicated in the circled region of Figure 5.20. As the width of the strips increases, the beamwidth increases also, a result which can be attributed to larger phase errors. The H-plane cross-polarization patterns are basically the same except for the first prototype

( $w = 0.254mm$ ) which is about  $7dB$  higher than the other cases at broadside. Also note that the cross-polarization patterns of all four prototypes have no null at broadside. These issues are discussed in Section 5.3.1. The H-plane co-polarization was investigated at other frequencies and the gain values are listed in Table 5.7.

**Table 5.7 Gain of holographic antennas at different frequencies**

<b>Prototype</b>	$f = 28GHz$ [dB]	$f = 29GHz$ [dB]	$f = 30GHz$ [dB]	$f = 31GHz$ [dB]	$f = 32GHz$ [dB]
$w = 0.254mm$	10.61	15.47	16.15	16.56	16.91
$w = 0.5mm$	10.60	14.83	16.16	16.20	16.39
$w = 1.0mm$	13.96	13.53	15.92	15.25	15.03
$w = 1.5mm$	14.35	13.39	16.12	15.03	14.46

Based on the above table, at low frequencies the largest widths offer the highest gain. But as the frequency increases, the narrowest conducting strips offer higher gains. This reversal effect is observed around  $28.4GHz$ . The phenomenon is likely explained by the return loss behavior illustrated in Figure 5.22, where the open aperture of the feed is placed at the tip of the antenna (same setup as in radiation pattern measurements).

Based on these return loss results, as the width of the conducting strips increases, the return loss decreases for frequencies greater than  $28.4GHz$ . This probably explains the gain variations observed in the radiation patterns. Note that even if the return loss indicates a match for the case where the tip of the hologram is at the open aperture, this does not mean that the gain of the antenna is maximized. Usually the gain is higher due to better focusing with the tip of the hologram inside the open waveguide, although this results in a return loss response similar to Figure 5.18.



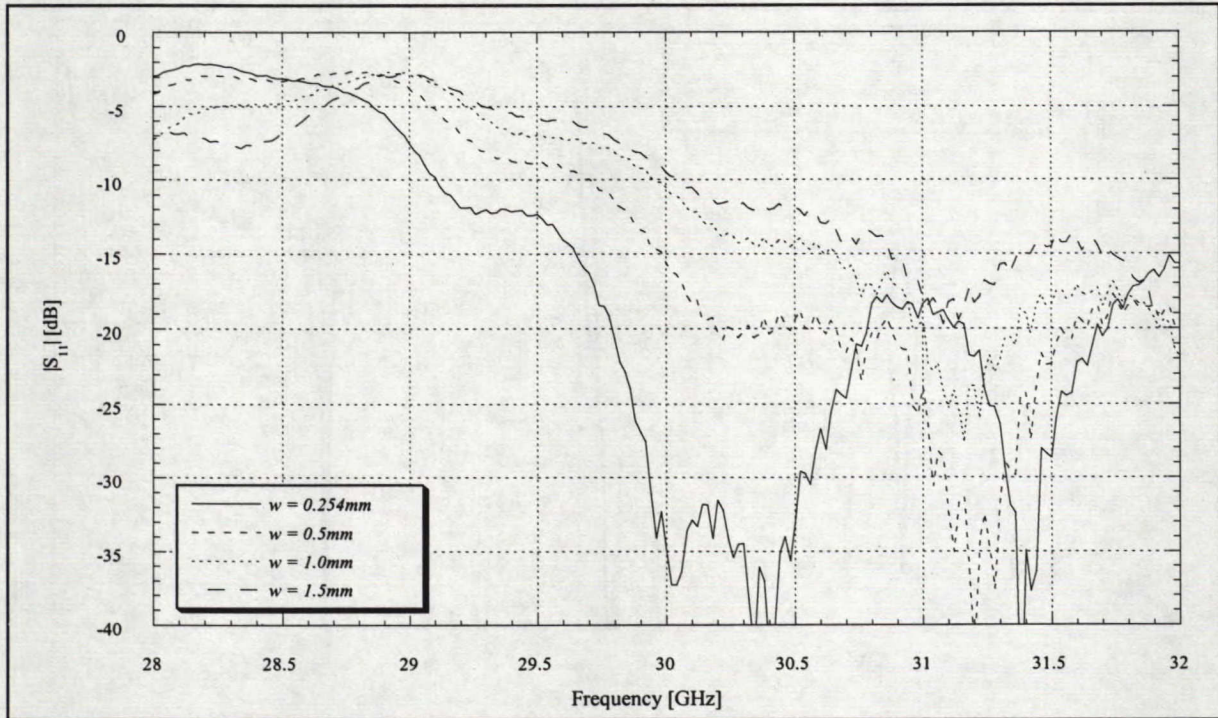
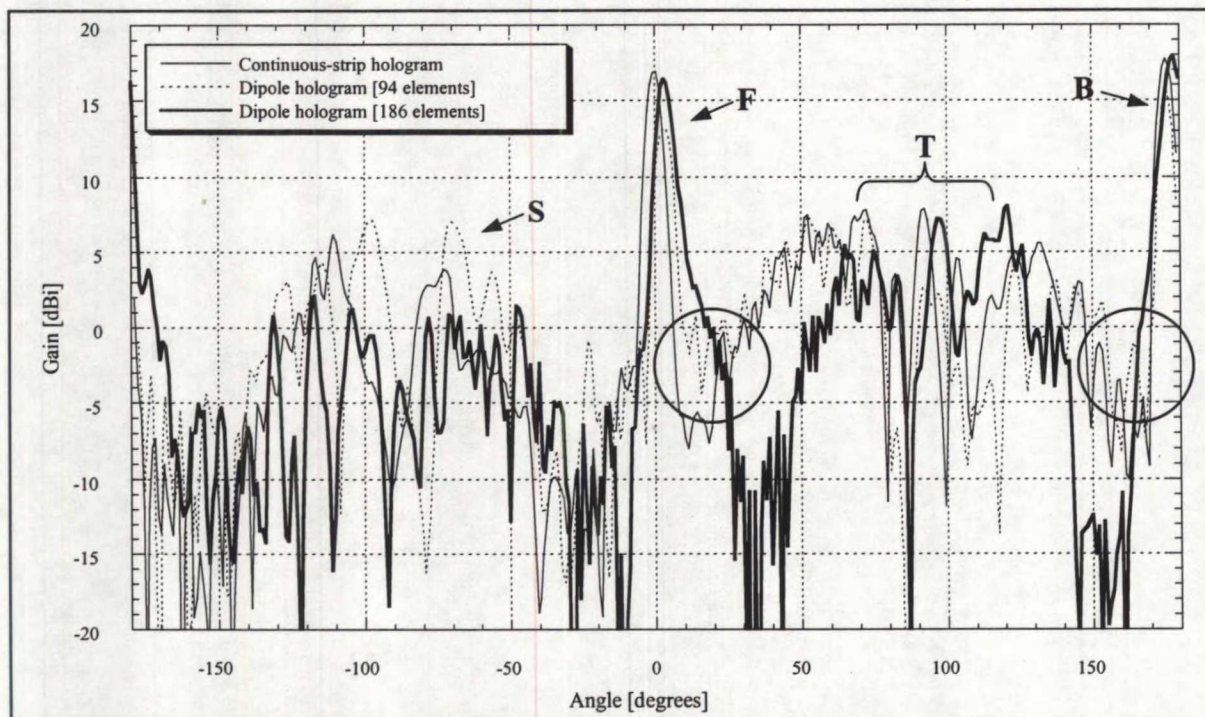


Figure 5.22.  $|S_{11}|$  of holographic antenna with varying strip widths.

### 5.1.6 Dipole hologram: second design

Since the first dipole hologram had a gain reduction of about  $2dB$  compared to the continuous-strip case, the second configuration, illustrated in Figure 3.7 (b) of Chapter 3, was designed and tested. This second dipole hologram has 186 elements (instead of 94) which are spaced by  $d = 0.5\lambda_o \approx 0.5cm$ . With this hologram, the gaps between the elements are significantly reduced, thus reducing the spillover loss. The H-plane radiation pattern of the second dipole hologram is illustrated in Figure 5.23 along with the continuous-strip hologram and the first dipole hologram results.





**Figure 5.23. H-plane radiation pattern of dipole holograms ( $f = 30\text{GHz}$ ).**

Compared to the first dipole hologram, the gain has increased by about  $2.3\text{dB}$  and is comparable to the continuous-strip hologram. Note that the location of the feed with respect to the hologram was not optimized for gain. The T lobe of the second configuration is narrower and the S lobe level is lower than for the first dipole hologram with fewer elements. However, the front and back lobe beamwidths are wider than with the 94-element dipole hologram which seems to indicate more phase error. The crucial test is the E-plane cross-polarization shown in Figure 5.24. Because of the beam scan, only the pattern at  $f = 28\text{GHz}$  is considered. The cross-polarization level of the two dipole holograms are basically the same. The high side lobes at  $\pm 90^\circ$  are due to the feed. Since the second dipole hologram generally behaves in the same fashion as the continuous-strip antenna (except for the E-plane cross-polarization improvement), the return losses should be similar. Because the dipole hologram with 186 elements performed



better than the first design, the return loss was measured for this case only. Figure 5.25 illustrates the return loss for both the continuous-strip and the dipole hologram where the tip of the antenna is at the open aperture of the feed.

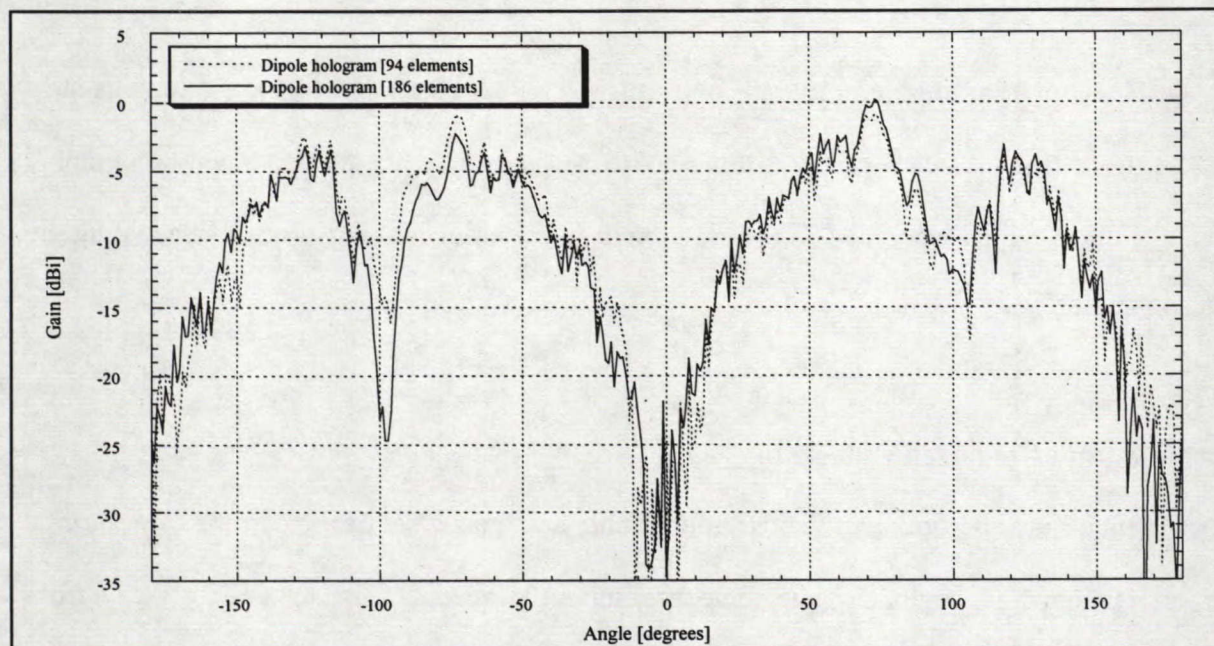


Figure 5.24. E-plane cross-polarization pattern of dipole holograms ( $f = 28\text{GHz}$ ).

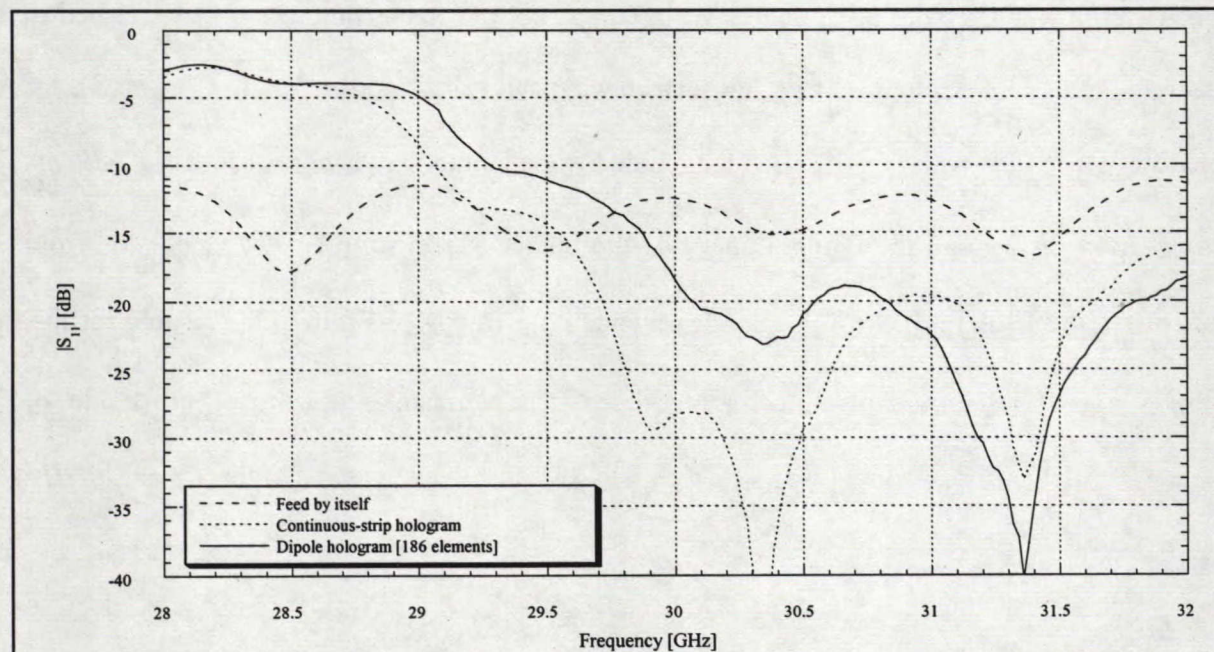


Figure 5.25.  $|S_{11}|$  of feed, continuous-strip and dipole holograms.

In general, the return loss of both holograms is not well matched at low frequencies but significantly improves for frequencies greater than  $29.5GHz$ . Placing the tip of the hologram plate closer to the open aperture of the feed drastically degrades the return loss.

Even though the dipole hologram performs very well compared to the continuous-strip case, it suffers from a beam squint similar to that observed with all the other holographic antennas of the previous section. The next section deals with this issue by properly designing the antenna using the guided wavelength.

## 5.2 Beam Squint Corrected Hologram

As mentioned before, because the holographic antennas were designed based on the free space wavelength and neglecting the dielectric surface waves, the beam squints away from broadside. To solve this problem, the elements are spaced by a new guided wavelength which must be determined at the desired frequency. In Chapter 3 various techniques were described to evaluate the guided wavelength. From the surface wave analysis (Section 3.2, in Chapter 3), for a dielectric of  $20mils$  with  $\epsilon_r = 3.38$ , the guided wavelength  $\lambda_g$  is found to be  $0.939cm$ . Based on array theory and the Floquet analysis, the guided wavelength can be calculated from the measured beam squint of the holographic antenna with  $d = \lambda_o$ . From the measured results, the single-layer hologram showed on many occasions a beam squint from broadside of  $\theta_{-1} = 2.39^\circ$ . Therefore, using (3-35) of Chapter 3, the guided wavelength at  $f = 30GHz$  ( $\lambda_o \approx 1cm$ ) is:

$$\lambda_g = \frac{\lambda_o}{\sin(2.39^\circ) + 1} \approx 0.959cm. \quad (5-1)$$



This explains why the antennas waving the elements spaced by  $\lambda_o$  performed better and have a beam peak closer to broadside at frequencies lower than  $30\text{GHz}$ . Thus, in order to obtain a broadside radiation, the distance between the elements must be smaller than the free-space wavelength.

A new holographic antenna was designed on Duroid 4003 with a thickness of  $20\text{mils}$  based on the guided wavelength evaluated experimentally ( $\lambda_g \approx 0.959\text{cm}$ ). The H-plane radiation pattern is shown in Figure 5.26. The first design ( $d = \lambda_o$ ) was re-tested as well where the tip of the hologram is inside the open waveguide.

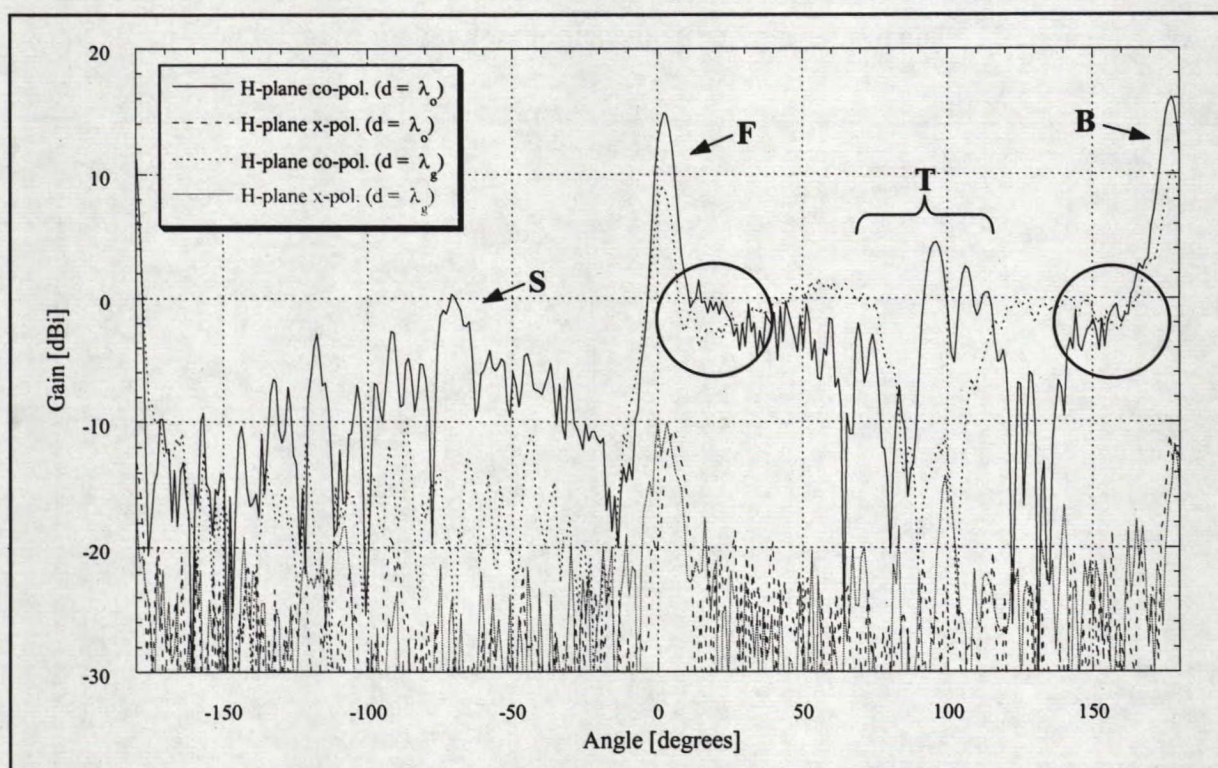
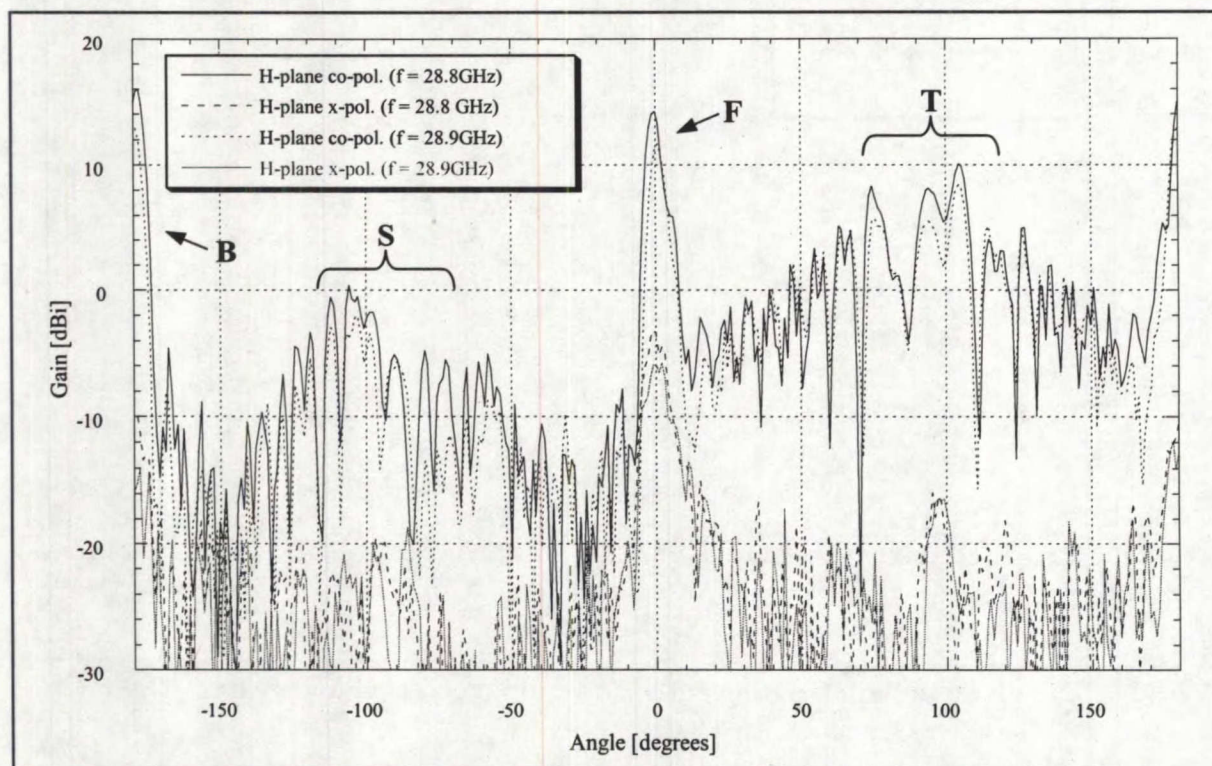


Figure 5.26. H-plane radiation pattern of beam squint corrected hologram ( $f = 30\text{GHz}$ ).



The gain of the beam squint corrected hologram is  $5.8\text{dB}$  less than that of the first single-layer hologram. The beam peak, however, squinted  $0.15^\circ$  less than in the first design. Note that the gain of both antennas is relatively low and the cross-polarization is high compared to the measurements obtained previously. Also the S and T lobe levels of the beam squint corrected hologram are lower than the first design and the phase error of both antennas illustrated in the circled regions of the figure, is considerably higher compared to the antennas tested in the previous sections. In fact, the T lobe does not appear to arise from the feed pattern as seen in the other results. Since a positive beam squint is observed at the desired frequency, this means the spacing between the elements is again too large. Therefore the patterns at other frequencies were evaluated and a beam peak close to broadside was observed around  $28.8\text{GHz}$  and  $28.9\text{GHz}$  as shown in Figure 5.27. The results at other frequencies are summarized in Tables 5.8 and 5.9.



**Figure 5.27. H-plane radiation patterns of beam squint corrected hologram.**

**Table 5.8 Beam squint from broadside for two holographic antennas**

Distance between Elements	28.0GHz [degrees]	28.8GHz [degrees]	28.9GHz [degrees]	29.6GHz [degrees]	30.0GHz [degrees]
$\lambda_o$	1.01°	2.18°	2.22°	2.35°	2.44°
$\lambda_g$	-3.90°	-1.76°	0.14°	2.42°	2.52°

**Table 5.9 Gain results for two holographic antennas**

Distance between elements	28.0GHz [dB]	28.8GHz [dB]	28.9GHz [dB]	29.6GHz [dB]	30.0GHz [dB]
$\lambda_o$	9.25	9.34	10.77	12.91	16.83
$\lambda_g$	16.43	15.98	12.95	10.18	10.22

Based on these results, the main beam scans in the positive direction with frequency and in the beam squint corrected case, it scans from a negative angle value to a positive one. At the same frequency, the gains of the two holograms are quite different. In the  $d = \lambda_o$  case, the gain increases with frequency for the frequency range shown in the above table, but decreases with frequency for the  $d = \lambda_g$  case. From the radiation pattern illustrated in Figure 5.27, looking at the front and back lobes, some phase error is present which results in a wider beamwidth. The spillover at the top of the antenna (T lobe level) is also significantly higher compared to the one at 30GHz. A last important observation to mention is the cross-polarization, which again is not as good as expected since it should be zero at broadside.

Because the gains of both antennas are quite different, the return loss was measured in order to establish some explanations. The return loss was evaluated at two feed locations,  $P_1$  and  $P_2$ , with respect to the hologram plate. At  $P_1$  the tip of the hologram is at the open aperture and at  $P_2$  the tip is inside the feed. Figure 5.28 illustrates the return losses along with the results of the first design where  $d = \lambda_o$  between the strips.



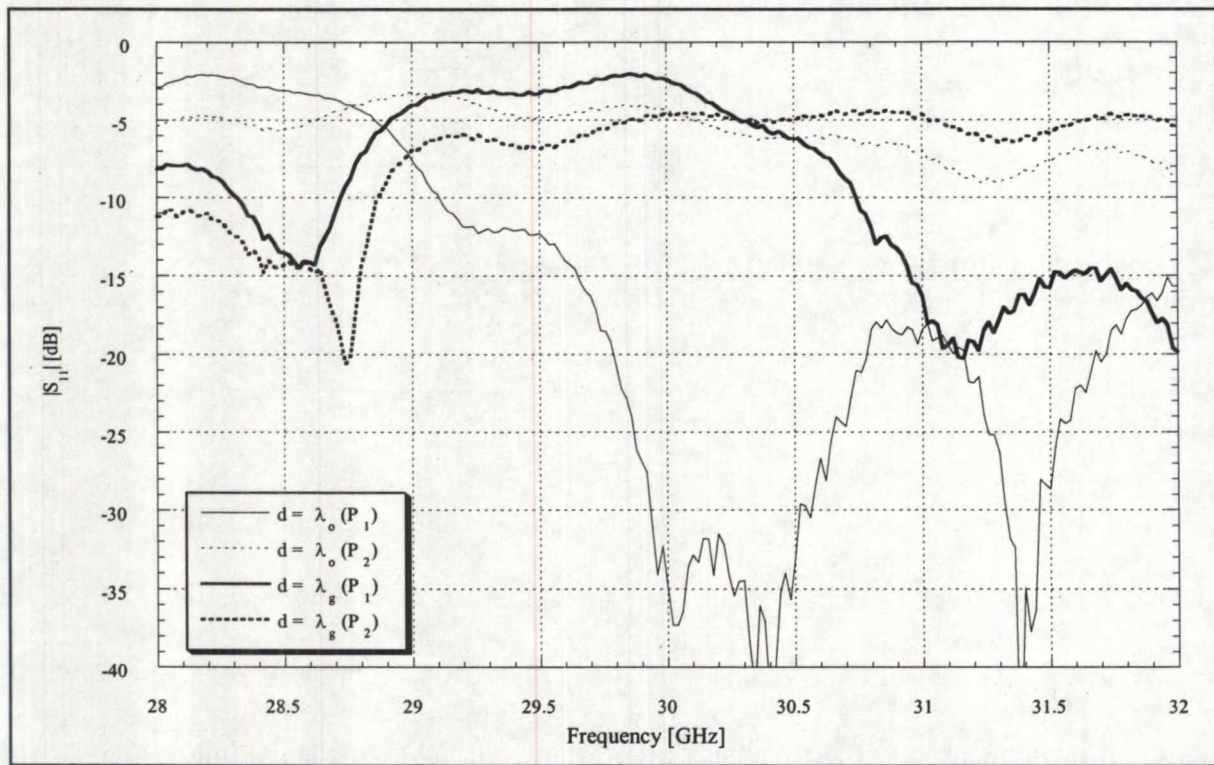


**Figure 5.28.  $|S_{11}|$  of beam squint corrected and non-corrected holograms.**

As with the previous results, an increase of the distance between the feed and the antenna improves the return loss at high frequencies. Notice that the beam squint corrected hologram offers a better match for frequencies less than  $28.8\text{GHz}$  compared to the first design. Also, at  $P_1$  the matching of the beam squint corrected antenna between  $29.0\text{GHz}$  and  $30.5\text{GHz}$  is very poor compared to the first design.

Since most of the major issues have been investigated, it is now possible to analyze in greater detail the results obtained with the above holographic antennas. A full discussion along with some conclusions is presented in the next section.

## 5.3 Discussion

### 5.3.1 Efficiency considerations

#### *Two-layer hologram:*

Based on the results obtained in the above sections, the most promising technique in terms of increasing the efficiency is the two-layer hologram covered in Section 5.1.1. With the double-sided case, a gain increase of at least  $4dB$  was obtained at the desired frequency and more than  $6dB$  at lower frequencies. The antenna operates better at lower frequencies because the spacing between the conducting strips is too large for center frequency operation ( $30GHz$ ). Theoretically, because there are two antennas and because the back lobe is reflected to the front, a gain increase of at least  $6dB$  was expected at the design frequency. But in order to obtain such an improvement, the distance must be selected so that the phase between the elements meets certain conditions as discussed in Chapter 3 and in Section 5.1.1. Mutual coupling between the elements and the effects of the dielectric slab must be included for the accurate determination of the spacing between the two layers. Neglecting these effects, the back lobe will still be present at  $30GHz$  and it will be impossible to obtain the desired  $6dB$  because not all the fields are reflected towards the front lobe.

It was noticed that by varying the distance between the two layers, some phase interaction occurred because the beam peak value and the gain changed. There exists some mutual coupling between the two plates and some surface waves on the two dielectric slabs which affect the wavelength. Therefore, a more rigorous analysis is required for the accurate determination of layer spacing. Nevertheless, array theory is an acceptable approach to quickly

design a more efficient and low profile antenna. It also has the advantage of illustrating operating principles of two-layer holograms.

An attractive feature of the two-layer hologram is that it not only improves the efficiency of the antenna but it suppresses the back lobe as well. With the two-layer structure, by properly spacing the two holograms and phasing the conducting strips, it was possible to completely suppress the back lobe and obtain an efficiency of up to 20% at 28GHz. At  $f = 30\text{GHz}$  (and other frequencies), it is very difficult to reduce the back lobe by more than 10dB because the two holograms require a perfect alignment and the correct separation in order to obtain the appropriate phases. An offset of 1mm at 30GHz can significantly reduce the gain which means a more accurate control is required. This control can be obtained by modifying the frame such that a special holder would control the spacing between the two sets of rings with respect to the feed. Placing pieces of foam of different thicknesses could vary the distance that separates the two layers. Also note that, because the spacing between the two plates for the proper phase is valid at one frequency only, the back lobe can only be suppressed completely at this frequency.

In addition to reducing the back lobe, the two-layer hologram also reduces the S lobe as well, that is, the lobe returning towards the feed. It is difficult to see this lobe in the radiation patterns because of the feed blockage. However, it is possible to observe the effect of the S lobe by measuring the feed's return loss. In fact, the return loss of the two-layer structures was significantly improved when the back lobe was completely suppressed. There is every indication that if the back lobe is suppressed, so is the S lobe. This could explain why the return loss of the structure at 28GHz is similar to the open waveguide by itself. Assuming the S lobe is completely



suppressed across the entire frequency range, then the two-layer hologram should be virtually transparent to the open waveguide and the measured return loss would be exactly the same as the open waveguide by itself.

It was mentioned in Section 5.1.1 that by increasing the distance between the feed and the single layer hologram, a return loss similar to the two-layer case was obtained. However, as the distance increases, the feed is out of focus and the gain decreases. The best gain is in fact obtained when the tip of the hologram is inside the open waveguide where the return loss is the poorest. Dielectric loading is possibly the reason why the matching is very bad with the tip inside the feed. It is therefore very important in future designs that the feed be properly focused such that the tip of the hologram is not inside the feed. This implies changing the radius of the first conducting arc. However, it is also possible that the dielectric loading helps to launch the surface wave onto the surface of the hologram plate. This issue requires further investigation.

To improve the efficiency, more layers can be used but this technique requires more phase control. It is also possible to design a two-layer (or multi-layer) hologram based on hologram theory where various holograms are recorded by varying the location of the recording media (or holographic plates). However, such a technique neglects the effect of the mutual coupling that would result from the conducting strips and the effect of the dielectric slabs on which are etched the strips. Fortunately, certain microwave analysis techniques such as modeling and surface wave analysis help to predict the behavior of the antenna and mitigate the above drawbacks.

### *Holographic antenna illuminated by feed horns:*

Changing the feed to illuminate the hologram was the second method to improve the efficiency of the antenna by controlling spillover and tapering losses. Sectoral horns with the narrowest and widest H-plane beamwidths, along with a pyramidal horn, were selected as possible feeds to improve the spillover efficiency. In all three cases, at the desired frequency, the antennas have a lower gain and more spillover at the top of the antenna than the hologram illuminated by the open waveguide. The holograms with the new feeds, however, have more focused back and front lobes and less phase errors compared to the open waveguide case. The more uniform patterns of the horns could explain their better focusing capabilities. Also, as it was explained in Section 4.1.1, the spillover from the feed is mainly responsible for the distortion of the **F** and **B** lobes, which increases the beamwidth of the main beams. With the sectoral horns and the pyramidal horn, the interference between the horns' pattern and the hologram pattern near the main beams are reduced because these feeds have a smaller beamwidth than that of the open waveguide.

The increase in spillover is quite surprising because the feed horns all have H-plane and E-plane beamwidths less than the open waveguide beamwidths. Based on the reduction in gain, the hologram probably does not properly intercept the fields coming out of the new feed horn because it is out of focus, which results in more spillover from the feed. To focus the hologram onto the two sectoral horns, the tip of the holographic plate must be pushed further inside the open aperture of the horns. This is impossible because the aperture is too narrow, thereby limiting the focusing capabilities of the sectoral horns. It was also noticed from the results summarized in Table 5.3 that the gain varied with frequency and the type of feed. In general, the

gain is higher for frequencies greater than  $30\text{GHz}$  because the aperture size appears bigger. However, in terms of the feed itself, it is possible that at certain frequencies the radius of the spherical wave generated from the feed matches closely the radius of the conducting strips, and therefore increases the gain of the antenna. Because the feeds are different, the matching between the spherical wave and the conducting strips radii, which is related to the focal point, will occur at different frequencies. This could explain why at times one feed horn performs better at a certain frequency than at another. Since the focal point was not optimized for gain, it is possible that the hologram illuminated with the new feed horns offers more gain than with the open waveguide under perfect focusing conditions. The return loss was measured to possibly explain the relationship between the gain, the feed horns and the frequency. In general, the pyramidal horn offers a better return loss but has the lowest gain. Although it may seem contradictory, the possibility exists that the dielectric loading from the tip of the hologram affects positively or negatively the return loss, but does not vary the gain of the overall antenna. It is also possible that the beam of the pyramidal horn is too narrow to effectively illuminate the holograms.

The focusing aspect of the holographic antenna was further explored with the pyramidal horn, where the hologram is focused onto the apex and the phase center of the feed horn. This horn was selected for the test because it was possible to place the tip of the hologram more than  $5\text{mm}$  inside the open aperture. The best response was obtained when the hologram was focused onto the phase center of the pyramidal horn. A gain increase of  $4.25\text{dB}$  was observed compared to the non-focused case, and the spillover at the top of the antenna was reduced by almost  $3\text{dB}$ . For the hologram focused on the apex, the gain improved by about  $3.9\text{dB}$  and the S lobe was



reduced by  $1.3\text{dB}$ . The gain increase could have been attributed to the improved return loss, but generally the matching of the hologram focused onto the apex and the phase center was found to be worse than the unfocused case. Note that for the unfocused hologram the tip was outside the open aperture. Therefore the return loss is very sensitive to the dielectric loading of the feed when the hologram is focused. Another important observation is that the phase errors which appear in the front and back lobe increase when the hologram is focused. The resulting increase in beamwidth could be attributed to the fact that when the tip of the hologram is further inside the open aperture of the horn, there exists more interference between the feed and the hologram.

Since return loss and gain improvement are not related for the holograms focused onto the apex and the phase center, the focal point could then be the determining factor. Basically, when the antenna is properly focused the radii of the generated spherical wave match those of the conducting strips providing greater interception, less spillover and more gain. If the antenna intercepts more fields, then the S lobe level (lobe towards feed) is also higher and interferes with the feed, which could explain the degradation of the return loss in the phase center and apex focused cases. From these observations it is tempting to establish the phase center of the horn as the focal point or the point source from which the fields emanate. However it is possible that the optimal focal point is elsewhere inside the horn, because the rectangular horn has an H-plane and E-plane phase center (and apex) which do not necessarily coincide. Having two different phase centers basically means that the wave generated by the horn is elliptical instead of spherical, which results in phase errors in the radiation pattern of the holographic antenna. To obtain a better spherical wave, a square aperture can be considered, but this issue will have to be further investigated. At present, the first order approximation of focusing on the phase center or apex

helps to understand the behavior of the antenna and establish an additional technique to optimize the gain.

Based on the above discussion, the only advantage in varying the H-plane beamwidth of the feed is the reduction of the beamwidth (or the phase errors) of the main beam through reduced interference between the feed and antenna patterns. A smaller beamwidth does not reduce the spillover as expected. In fact, it seems that the amount of energy the hologram captures is closely related to the focal point of the feed and the quality of the spherical wave emerging from the open aperture. It is possible that the wider the H-plane beamwidth, the better will be the spherical wave. Many aspects of the holographic antenna feed will need more study.

#### *Diamond-shaped hologram:*

To improve the illumination efficiency the diamond-shaped hologram was considered to be a promising technique. However, other than having better focusing abilities (reduced phase errors) due to a more uniform illumination, the diamond-shaped hologram did not perform appreciably better than the square-shaped hologram in terms of gain. In fact, the H-plane patterns are very similar except for a slight increase of the S lobe level in the diamond-shaped case. This S lobe level increase did not seem to affect the matching because the tapering at the tip of the diamond-shaped hologram generally results in a better return loss than in the square-shaped case. However, even with the better return loss the gain was not improved. Also, it is very difficult to observe gain improvement when the return loss is less than  $10\text{dB}$ .

It is interesting to see that the E-plane cross-polarization at broadside was improved by  $3\text{dB}$  compared to the square-shaped antenna. This was expected since the diamond-shaped antenna reflects less the vertical components of the electric field. The high sidelobes in the E-plane cross-polarization at  $\pm 90^\circ$  are basically due to some spillover from the feed. The spillover of the diamond-shaped hologram is greater than the square-shaped hologram because the shape of the antenna favors a uniform illumination rather than a tapered one. There is always a tradeoff between the illumination efficiency and the spillover efficiency, and a uniform illumination results in higher side lobes than a tapered distribution. It would be possible to determine the proper shape (or angle) for the hologram such that the illumination and the spillover efficiencies are optimal. Also worth investigating is the focal point (or the distance between the feed and the hologram) of the diamond-shaped hologram, which was not optimized in this work.

#### *Microstrip width test:*

The width of the microstrip lines on the single-layer antenna was varied to see how the hologram would behave. Other than the beamwidth, at the desired frequency no significant differences were observed. All the antennas offer a relatively higher gain at frequencies greater than  $30\text{GHz}$  because the aperture size appears to be larger at these frequencies. Also the antennas have a better impedance match at these frequencies. For frequencies less than  $28.4\text{GHz}$ , the antenna with the widest strip offers the best match, which could explain the higher gain compared to the other antennas when referring to Table 5.7. Note, however, that it is possible at the same frequency that the gain varies slightly from one case to the other because it is very difficult to align the four antennas in exactly the same way during measurements. In fact, from the cross-polarization patterns in Figure 5.21, one can clearly see that some co-polarized



fields are present, especially in the narrowest microstrip case, which means that the antennas were not properly set up. These misalignments basically result in a higher cross-polarization and a lower gain for beams with very narrow beamwidths.

In general, the four antennas behaved in almost exactly the same way with varying frequency. The beam peak value is similar for all cases, which was expected since the conducting strips have the same spacing between each other. The scan rate as the frequency increases was also similar and the  $3dB$  beamwidths are quite comparable. The major difference between the four prototypes is the beamwidth for gain values around the  $0dB$  level (in both the front and back lobes) which increases with the strip's width. With wide microstrip lines, the fields do not radiate uniformly like on the thin lines, which results in a greater phase error and a wider beamwidth (or merging sidelobes with the main lobe).

It is therefore desirable to design future holographic antennas with very narrow conducting strips since they offer better focusing capabilities. However, it would be possible to design antennas with wider microstrip lines if a scattering and current analysis is conducted in order to properly space the strips and minimize the phase errors.

#### *Dipole hologram:*

The final efficiency optimization test involved redesigning the dipole hologram with more elements to increase the efficiency. The gain increased by  $2.3dB$  compared to the first dipole hologram, but had more phase errors than the continuous-strip hologram. This side effect was expected since it is very difficult to control the phase of  $186$  dipoles. It would be possible to

determine the location of each dipole in the array such that once illuminated by the feed they are all in phase. This would require analyzing the current and the scattering on each element. Note that the coupling effects should also be taken into account in the analysis. Again the cross-polarization was greatly improved at broadside such as in the first dipole hologram. This feature makes the dipole hologram very appealing since in general it behaves in the same manner as the continuous-strip hologram.

#### *General issues:*

Even though the major issues have been covered, there remain other aspects of the holographic antenna that should be mentioned. For instance, it was assumed in the recording of the hologram that the plane wave had a uniform amplitude and phase distribution across the entire recording medium. However, in a real operating environment, the plane waves incident on the hologram plate will often come from various directions with different amplitude levels due to multiple reflections on obstacles. These amplitude and phase variations will result in phase errors and a degradation of the radiation pattern. It was also assumed that the spherical wave generated by the feed was a uniform spherical wave. With the feeds used to illuminate the holograms (including the open waveguide), the amplitude distribution is not quite uniform and the radiated wave tends to be more elliptical than spherical, as mentioned earlier. Also, in the near-field region there is the radiating spherical wave and the reactive near-field component which does not propagate. This reactive part could significantly affect the radiation properties of the feed in the near-field region and change the radius of the spherical wave in an unexpected way. It is therefore crucial to further evaluate and understand the behavior of the feed in the near-field region.

The coupling between the conducting strips and the half-wave dipoles in the dipole hologram is another factor responsible for the phase errors. The mutual coupling can also change the gain and increase the level of the side lobes. It would be possible to evaluate the effect of mutual coupling between the elements by studying the scattering behavior of the waves on the conducting strips, and develop a better model for the holographic antenna. This model could also include the effects of varying the strips' width.

Another possible loss factor can be attributed to the dielectric slab on which the conducting strips are etched. It was seen in Section 3.3 of Chapter 3 that when a plane wave is incident on the dielectric slab with  $\epsilon_r = 3.38$  and a thickness of *20mils*, 11.4% of the power is reflected back and only 88.6% of the wave can be captured by the feed. Therefore, about *0.5dB* of gain is lost. The dielectric slab is also accountable for the gain difference between the back lobe and front lobe. In fact the slab slightly varied the beam squint of the back lobe compared to the front lobe. In general this beam squint difference is very minimal (less than  $2^\circ$ ).

As a comparison, the efficiency of microstrip fed arrays with the same aperture size as the holographic antenna is approximately evaluated at EHF frequencies to be 25% [27]. Therefore, both the holographic antenna and the microstrip phased array have a comparable efficiency.

### 5.3.2 Beam squint issues

The beam squint corrected hologram, designed using the experimentally measured beam peak to evaluate  $\lambda_g$ , operated at a lower frequency than the desired one (*30GHz*). It is therefore



clear that the guided wavelength is still too large. The next antenna should be designed from the guided wavelength calculated with the surface wave analysis, since it is less than the  $\lambda_g$  used to design the first beam squint corrected hologram. It is possible, however, that this theoretical value and the one evaluated from the Floquet analysis are not exactly the guided wavelength of the holographic antenna. This is because all of the analyses done in Chapter 3 assume that the conducting strips have no effect on  $\lambda_g$  and, therefore, in the periodic structure analysis, the characteristic curve of the fundamental Floquet mode is treated as being the fundamental mode of the slab without strips. Coupling effects between elements were also neglected along with the finite size of the hologram. Nevertheless, the beam squint corrected hologram showed that the beam peak scans with frequency from negative to positive values, as predicted by the theory.

From Table 5.9, it is noticed that the gain of the beam squint corrected hologram varies differently from the single layer hologram design based on  $\lambda_o$ . Based on the return loss curves (Figure 5.28) for the  $P_2$  case (tip inside feed), the beam squint corrected hologram offers a significantly better match for frequencies less than  $28.9GHz$ , which could explain the higher gain at these frequencies. For the  $\lambda_o$  antenna, the return loss and gain improve as the frequency increases. The reverse effect is observed with the beam squint corrected antenna. If the focal point is moved to  $P_1$  (tip at open aperture of open waveguide), then the beam squint corrected hologram performs better at lower frequencies in terms of return loss and therefore should offer a better gain at these frequencies than the  $\lambda_o$  antenna. The gain was not measured for the  $P_1$  case, but will be investigated in the future.

To complete the discussion of Chapter 4 on the beam squint issue, the guided wavelength was evaluated at  $28GHz$  based on the surface wave analysis done in Section 3.2.1. The guided wavelength was found to be  $\lambda_g \approx 0.99cm$  which is virtually the same as the distance between the conducting strips. This explains why the beam peak of the holographic antennas designed based on the free-space wavelength is near broadside at this frequency.

Finally, it was noted from the radiation patterns in Section 5.2 that the T and S lobe levels, the cross-polarization level and the phase errors were worse than expected. When the beam squint corrected hologram was tested, the antenna chamber suffered from many problems such as unreliable cables, alignment problems, and inconsistencies between the H-plane and E-plane gain values. It is possible that all these issues may have corrupted the results shown in Section 5.2, thereby explaining the low gain observed in the patterns compared to the holographic antennas tested in Chapter 4. The focal point, which was not optimized, and the alignment problems could explain the phase errors and the high cross-polarization level at broadside. Also it was noticed that the power amplifier used to increase the transmitted power level lost about  $0.3dB$  of gain after a few hours of use.

## CHAPTER 6

### Conclusions and Future Work

In this thesis, the application of optical hologram theory at microwave frequencies to design holographic antennas has been investigated. Some design procedures have been established and various techniques to increase the efficiency of the holographic antennas have been studied. Holographic antennas have been successfully demonstrated with an operational efficiency comparable to a conventional microstrip phased array.

Some background on optical hologram theory was first presented for a better understanding of the concept. The review on holography gives the mathematical tools necessary to generate the interference pattern between a reference and an object wave. It also helps to visualize how the object wave is reconstructed once the hologram is illuminated by the reference wave. The optical holographic concept was then applied at microwave frequencies to design holographic antennas. From the destructive interference pattern, the construction of the holographic plate with a dielectric sheet and the behavior of the radiated fields from the conducting strips were studied. These issues were then considered in the selection of the aperture size of the antenna and the prediction of the theoretical far-field radiation pattern.

Following the hologram theory, a microwave analysis of the hologram was undertaken. The holographic antenna was treated as an array of conducting strips, a traveling wave antenna, and a periodic structure to evaluate the guided wavelength and the beam scan versus frequency. The theoretical guided wavelength was also evaluated based on a surface wave analysis. The H-



plane far-field radiation pattern was then calculated by treating the holographic antenna as an array of loop antennas. The pattern has four main lobes  $90^\circ$  apart, which is in agreement with the prediction of holographic theory. For the cross-polarization reduction of the antenna, a new hologram, which consists of an array of horizontally polarized half-wave dipoles, was introduced. This dipole hologram could be used to design dual-polarized, circular polarized, and multi-beam holograms. Array theory was also applied to the design of multi-layer holograms. A two-layer holographic antenna was considered for operational efficiency improvement, with the phase between the layers being selected such that undesirable beams are suppressed.

Measurement of various prototypes on different materials validated the holographic antenna concept. Based on these results, it was suggested that future holographic antennas be fabricated on the dielectric which offers the best performance in terms of gain, phase error and rigidity. The radiation patterns of the prototypes all had four beams separated approximately by  $90^\circ$  as predicted by theory. The level of the side lobes was not exactly as predicted theoretically because of scattering and interference caused by the feed and the antenna support structure. By carefully locating the feed at the focal point, it was possible to increase the efficiency of the single-layer hologram to 6.3%. Since the prototypes were designed based on the free-space wavelength, the radiation patterns suffered from a shift in the beam peak at the desired frequency. Therefore, future antennas should be designed based on the guided wavelength predicted by theory. It is also interesting to note that the beam scans with frequency since the hologram behaves as a traveling wave antenna. Improvement of the cross-polarization at broadside was confirmed with the dipole hologram. A reduction in gain, however, suggests that dipole holograms should have more elements to increase the interception efficiency.

As a result of the initial measurement results, a general procedure for the design of holographic antennas was established and some efficiency and beam squint improvement techniques were considered. These techniques include the two-layer hologram, new feed horns, and a diamond-shaped hologram to increase the illumination efficiency.

Following the above guidelines, new prototypes were designed to increase the efficiency. With the two layer holograms, an efficiency greater than 25% was obtained with the double-sided configuration and the back lobe was completely suppressed with the two-plate structure separated by spacers. The return loss of the holographic antenna was significantly improved using the two-layer structure by reducing the effects of the side lobe directed towards the feed. The second goal, which was to increase the spillover efficiency by changing the feed, is still inconclusive. It did, however, establish a relationship between the feed and the focal point. The antenna must be properly focused to properly intercept the fields generated by the horn to reduce the spillover. Also, it was determined that the hologram performs better when the antenna focal point is at the phase center rather than the apex of the horn. The diamond-shaped hologram did not improve the illumination efficiency as expected. It did, however, decrease the cross-polarization level at broadside compared to the square-shaped hologram. Nevertheless, the best technique to improve the cross-polarization level is the dipole hologram which was re-designed with more elements. This antenna is promising because it suppresses the cross-polarization at broadside, while at the same time, offering a gain similar to the continuous-strip hologram. The last important issue is the beam squint seen in the radiation patterns of the holographic antennas. A new antenna, where the conducting strips are spaced by one guided wavelength, was designed and showed that it is possible to obtain a broadside radiation in the frequency band of interest.

The main goals and objectives of this thesis have been achieved; however, other issues regarding holographic antennas and the application of optical hologram theory at microwave frequencies still need to be investigated and improved upon. For instance, because the antenna operates at Ka-band, a more accurate control of the feed location at the focal point of the antenna, and the separation distance of the hologram plates in multi-layer structures, is required. A better understanding of how the fields are generated by the feed and how one can efficiently capture these fields with the hologram is another area that needs further investigation. There is also the issue of guided wavelength prediction that requires a more rigorous evaluation to allow complete elimination of the beam shift at the desired frequency.

Based on the above conclusions, future work should be directed towards the development of a more accurate theoretical model based on periodic structures and gratings. This means the Floquet mode analysis done in Chapter 3 needs to be extended. The mutual coupling between the elements and the scattering effects on the strips should be included in the model to complete the analysis. A more accurate model of the current distribution on the strips is also necessary and could be used in the calculation of the far-field radiation pattern. In terms of feeds it would be interesting to measure the near-field radiation pattern of the feed and use this pattern as the reference wave to generate the hologram. Also, feeds other than horns should be investigated such as end-fire microstrip antennas etched on the same plane as the holographic plate to reduce the profile of the antenna. Other investigations could include the design of dual-polarized, circular polarized, multi-beam, and scanned beam holographic antennas. Finally, better hologram designs consisting of interleaved holograms and thick holograms for efficiency improvement should be studied. Some interleaved holograms, which are multiple holograms



etched on the same layer, have been designed and tested, but the results are not yet conclusive. As for thick holograms, they provide more phase and amplitude control of the interference patterns (or the grating) inside the recording medium. However, reproducing such a hologram with dielectric materials and conducting strips is quite a challenge since there is no equivalent optical recording process at microwave frequencies for this type of antenna.

Holographic antennas are an area worth investigating since they can offer low profile structures and can be designed simply by evaluating the destructive pattern between a plane wave and a spherical wave. They are also part of a family of antennas in which parabolic antennas, flat reflectors, and Fresnel lenses are members. Therefore, the techniques used to evaluate and increase the efficiency of the holographic antenna could be applied to these other antenna technologies and vice versa. Finally, with the improvement techniques developed in this thesis, holographic antennas designed to date can offer efficiencies comparable to those of Ka-band microstrip phased arrays with conventional micro-strip feeds, making this a very promising technology for future LMCS and EHF SATCOM applications.

## APPENDIX A

### Point Matching Approach

The following MATLAB program computes the  $\kappa_o$  versus  $\beta_z$  curve for the  $TE_x^{11}$  mode supported by a dielectric waveguide based on the Point Matching Approach, fully described in [22]. The dielectric constant of the waveguide is  $\epsilon_r = 3.38$  and its dimensions are  $a = 10\text{ cm}$  and  $b = 0.0508\text{ cm}$ . For simplicity and since the results are scalable, the dimensions of the slab were treated in meters ( $a = 10\text{ m}$  and  $b = 0.0508\text{ m}$ ) in the code.

```
%%%%%%%%%%%%%%%%%%%%%%%%%%%%%%%%%%%%%%%%%
% Kathia Lévis                          %
% Main Program                          %
%%%%%%%%%%%%%%%%%%%%%%%%%%%%%%%%%%%%%%%%%

% This program uses the fzero function to find the value of BETAz that will
% yield a null det(G) By calling the function that calculates the det(G) for
% a given BETAz and frequency.

clear all;
close all;

% Define global variables
Co = 2.99792458e8;           % Speed of light
Uo = (4*pi)*1e-7;           % Permeability
Eo = 1/(Co*Co*Uo);          % Permittivity
Er1 = 1;                     % Dielectric constant cladding
Er2 = 3.38;                  % Dielectric constant core
E1 = Er1*Eo;
E2 = Er2*Eo;
n1 = sqrt(Er1);              % Index of refraction for medium 1
n2 = sqrt(Er2);              % Index of refraction for medium 2
nr = n2/n1;                  % relative index of refraction
b = 0.0508;                  % Dimensions of structure in m
a = 10;                      % Dimensions of structure in m
counter = 0;
X = [1e-11 1e-11];          % Initialize vector

% Find b/lambdao for various betaz
for Bz_Bo = n1+0.002:0.002:1.20,
    counter = counter + 1;
    Bz_Bo
    P(counter) = Bz_Bo;
    if Bz_Bo >= n1+0.002*3
        X(2) = X(1);
    else
```

```

        X(2) = X(1) + 1e-11;
    end
    % Find upper interval point such the det sign is inverse of first point
    if Bz_Bo >= n1+0.002*3
        temp1 = PMM_f2(X(1),P(counter));    % Calculate det(G) of guess
        while temp1*PMM_f2(X(2),P(counter)) >= 0,
            X(2) = X(2)+0.01;
        end
    end
    % Find the D value that gives a det(G) = 0
    D(counter) = fzero('PMM_f2',X,1e-16,0,P(counter))

    % Calculate free space wave number
    ko(counter) = D(counter)*2*pi/b;
    Bz(counter) = P(counter)*ko(counter);    % Calculate Betaz
    % Set next guess to the valued of Psquare found
    X(1) = D(counter);
end

% Plot the betaz/betao vs b/lambdao curve
plot(D,P);
xlabel('b/lambda_o');
ylabel('beta_z/Betao');
title(['Dispersion Curve for Dielectric Waveguide where e_r = ',num2str(Er2),', a = ',num2str(a),'m & b = ',num2str(b),'m.']);
grid;
axis([0 0.5 n1 n2]);

% Plot the betaz/betao vs b/lambdao curve
figure;
plot(Bz,ko);
xlabel('beta [rad/m]');
ylabel('K_o [rad/m]');
title(['K_o versus beta_z for dielectric waveguide where e_r = ',num2str(Er2),', a = ',num2str(a),'m & b = ',num2str(b),'m.']);
grid;
axis([0 1000 0 1000]);

%%%%%%%%%%%%%%%%%%%%%%%%%%%%%%%%%%%%%%%%%%%%%%%%%%%%%%%%%%%%%%%%%%%%%%%%
% Kathia Lévis    %
% Function        %
%%%%%%%%%%%%%%%%%%%%%%%%%%%%%%%%%%%%%%%%%%%%%%%%%%%%%%%%%%%%%%%%%%%%%%%%

% This function calculates the determinant of the G matrix for a given BETAZ
% using the Point Matching Approach
% The function takes the values of B (normalized frequency) and P square
% (normalized phase constant)

function det_G = PMM_f2(B,Bz_Bo)    % Defining the function

% Define global variables
Co = 2.99792458e8;    % Speed of light
Uo = (4*pi)*1e-7;    % Permeability
Eo = 1/(Co*Co*Uo);    % Permittivity
Er1 = 1;    % Dielectric constant in cladding
Er2 = 3.38;    % Dielectric constant core
E1 = Er1*Eo;

```



```

E2 = Er2*Eo;
n1 = sqrt(Er1); % Index of refraction for medium 1
n2 = sqrt(Er2); % Index of refraction for medium 2
nr = n2/n1; % relative index of refraction
b = 0.0508; % Dimensions of structure in m (100 times
% greather than real structure)
a = 10; % Dimensions of structure in m (100 times
% greather than real structure)
phi_c = atan(b/a); % Critical angle
P = 11; % Number of matching points
flag = 0;

% Loop to calculate the angles at each matching points
while flag == 0,
    for p = 1:1:P,
        phi_p(p) = (p-1/2)*pi/(2*P); % Angle between each matching
points
        if phi_p(p) ~= phi_c
            flag = 1;
        else
            flag = 0;
            P = P + 1;
            break;
        end
    end
end

H = P; % Number of space harmonics
M = 2*H-1; % For the summation (from m to M)
w = (2*pi)*(Co*B)/b; % Frequency
BETA2 = w^2*Uo*Er2*Eo; % Propagation constant squared of medium
2
BETA1 = w^2*Uo*Er1*Eo; % Propagation constant squared of medium
1
BETAo = w*sqrt(Uo*Eo); % Propagation constant in free space
BETAz = BETAo*Bz_Bo; % Calculate BETAz from P square
BETAp2 = sqrt(BETA2-BETAz^2); % Calculate BETArho2
ALPHAp1 = sqrt(-BETA1+BETAz^2); % Calculate ALPHArho1

% We want to find the Ex11 fields
THETAe = pi/2; % For mw in Horizontal and
THETAh = 0; % For ew in Vertical

% We want to find the Ey11 fields
%THETAe = 0; % For ew in Horizontal and
%THETAh = pi/2; % For mw in Vertical

% Must determine the radius for each matching points
for m = 1:2:M,
    if phi_p((m+1)/2) < phi_c
        rho((m+1)/2) = (a/2)/cos(phi_p((m+1)/2));
    else
        rho((m+1)/2) = (b/2)/sin(phi_p((m+1)/2));
    end
end

% Must start to generate the submatrices of the G matrix

```

```

% The matrices are scaled in order to reduce the magnitude of the DET(G)
% Generate E_LA, E_LC, H_LB, and H_LD (longitudinal fields)
for p = 1:1:P,
    for m=1:2:M,
        E_LA(p, (m+1)/2) = (BETAp2^2*((a+b)/2)/abs(besselj(m, BETAp2*b))) * besselj(m, BETAp2*rho(p)) * sin(m*phi_p(p)+THETAe);
        E_LC(p, (m+1)/2) = (ALPHAp1^2*((a+b)/2)/besselk(m, ALPHAp1*b)) * besselk(m, ALPHAp1*rho(p)) * sin(m*phi_p(p)+THETAe);
        H_LB(p, (m+1)/2) = (BETAp2^2*((a+b)/2)/abs(besselj(m, BETAp2*b))) * besselj(m, BETAp2*rho(p)) * sin(m*phi_p(p)+THETAh);
        H_LD(p, (m+1)/2) = (ALPHAp1^2*((a+b)/2)/besselk(m, ALPHAp1*b)) * besselk(m, ALPHAp1*rho(p)) * sin(m*phi_p(p)+THETAh);
    end
end

% Generate E_TA1, E_TA2, E_TB1, E_TB2, E_TC1, E_TC2, E_TD1, E_TD2 (transverse E)
for p = 1:1:P,
    for m=1:2:M,
        if phi_p(p) < phi_c
            E_TA1(p, (m+1)/2) = (BETAp2^2*((a+b)/2)/abs(besselj(m, BETAp2*b))) * (cos(phi_p(p))/rho(p)) * (1/(BETAz^2-
            BETA2)) * (BETAz/(w*Uo)) * (m*besselj(m, BETAp2*rho(p)) * cos(m*phi_p(p)+THETAe));
            E_TA2(p, (m+1)/2) = (BETAp2^2*((a+b)/2)/abs(besselj(m, BETAp2*b))) * (sin(phi_p(p))/(BETAz^2-
            BETA2)) * (BETAz/(w*Uo)) * BETAp2 * (besselj(m-1, BETAp2*rho(p)) - (m/(BETAp2*rho(p))) * besselj(m, BETAp2*rho(p))) * sin(m*phi_p(p)+THETAe);
            E_TB1(p, (m+1)/2) = (BETAp2^2*((a+b)/2)/abs(besselj(m, BETAp2*b))) * (-cos(phi_p(p))/(BETAz^2-
            BETA2)) * BETAp2 * (besselj(m-1, BETAp2*rho(p)) - (m/(BETAp2*rho(p))) * besselj(m, BETAp2*rho(p))) * sin(m*phi_p(p)+THETAh);
            E_TB2(p, (m+1)/2) = (BETAp2^2*((a+b)/2)/abs(besselj(m, BETAp2*b))) * (sin(phi_p(p))/rho(p)) * (1/(BETAz^2-
            BETA2)) * (m*besselj(m, BETAp2*rho(p)) * cos(m*phi_p(p)+THETAh));
            E_TC1(p, (m+1)/2) = (ALPHAp1^2*((a+b)/2)/besselk(m, ALPHAp1*b)) * (cos(phi_p(p))/rho(p)) * (1/(BETAz^2-
            BETA1)) * (BETAz/(w*Uo)) * (m*besselk(m, ALPHAp1*rho(p)) * cos(m*phi_p(p)+THETAe));
            E_TC2(p, (m+1)/2) = (ALPHAp1^2*((a+b)/2)/besselk(m, ALPHAp1*b)) * (sin(phi_p(p))/(BETAz^2-
            BETA1)) * (BETAz/(w*Uo)) * ALPHAp1 * (-besselk(m-1, ALPHAp1*rho(p)) -
            (m/(ALPHAp1*rho(p))) * besselk(m, ALPHAp1*rho(p))) * sin(m*phi_p(p)+THETAe);
            E_TD1(p, (m+1)/2) = (ALPHAp1^2*((a+b)/2)/besselk(m, ALPHAp1*b)) * (-cos(phi_p(p))/(BETAz^2-BETA1)) * ALPHAp1 * (-
            besselk(m-1, ALPHAp1*rho(p)) - (m/(ALPHAp1*rho(p))) * besselk(m, ALPHAp1*rho(p))) * sin(m*phi_p(p)+THETAh);
            E_TD2(p, (m+1)/2) = (ALPHAp1^2*((a+b)/2)/besselk(m, ALPHAp1*b)) * (sin(phi_p(p))/rho(p)) * (1/(BETAz^2-
            BETA1)) * (m*besselk(m, ALPHAp1*rho(p)) * cos(m*phi_p(p)+THETAh));
        else
            E_TA1(p, (m+1)/2) = (BETAp2^2*((a+b)/2)/abs(besselj(m, BETAp2*b))) * (-sin(phi_p(p))/rho(p)) * (1/(BETAz^2-
            BETA2)) * (BETAz/(w*Uo)) * (m*besselj(m, BETAp2*rho(p)) * cos(m*phi_p(p)+THETAe));
            E_TA2(p, (m+1)/2) = (BETAp2^2*((a+b)/2)/abs(besselj(m, BETAp2*b))) * (cos(phi_p(p))/(BETAz^2-
            BETA2)) * (BETAz/(w*Uo)) * BETAp2 * (besselj(m-1, BETAp2*rho(p)) - (m/(BETAp2*rho(p))) * besselj(m, BETAp2*rho(p))) * sin(m*phi_p(p)+THETAe);
            E_TB1(p, (m+1)/2) = (BETAp2^2*((a+b)/2)/abs(besselj(m, BETAp2*b))) * (sin(phi_p(p))/(BETAz^2-
            BETA2)) * BETAp2 * (besselj(m-1, BETAp2*rho(p)) - (m/(BETAp2*rho(p))) * besselj(m, BETAp2*rho(p))) * sin(m*phi_p(p)+THETAh);
            E_TB2(p, (m+1)/2) = (BETAp2^2*((a+b)/2)/abs(besselj(m, BETAp2*b))) * (cos(phi_p(p))/rho(p)) * (1/(BETAz^2-
            BETA2)) * (m*besselj(m, BETAp2*rho(p)) * cos(m*phi_p(p)+THETAh));
            E_TC1(p, (m+1)/2) = (ALPHAp1^2*((a+b)/2)/besselk(m, ALPHAp1*b)) * (-sin(phi_p(p))/rho(p)) * (1/(BETAz^2-
            BETA1)) * (BETAz/(w*Uo)) * (m*besselk(m, ALPHAp1*rho(p)) * cos(m*phi_p(p)+THETAe));
            E_TC2(p, (m+1)/2) = (ALPHAp1^2*((a+b)/2)/besselk(m, ALPHAp1*b)) * (cos(phi_p(p))/(BETAz^2-
            BETA1)) * (BETAz/(w*Uo)) * ALPHAp1 * (-besselk(m-1, ALPHAp1*rho(p)) -
            (m/(ALPHAp1*rho(p))) * besselk(m, ALPHAp1*rho(p))) * sin(m*phi_p(p)+THETAe);
            E_TD1(p, (m+1)/2) = (ALPHAp1^2*((a+b)/2)/besselk(m, ALPHAp1*b)) * (sin(phi_p(p))/(BETAz^2-BETA1)) * ALPHAp1 * (-
            besselk(m-1, ALPHAp1*rho(p)) - (m/(ALPHAp1*rho(p))) * besselk(m, ALPHAp1*rho(p))) * sin(m*phi_p(p)+THETAh);
            E_TD2(p, (m+1)/2) = (ALPHAp1^2*((a+b)/2)/besselk(m, ALPHAp1*b)) * (cos(phi_p(p))/rho(p)) * (1/(BETAz^2-
            BETA1)) * (m*besselk(m, ALPHAp1*rho(p)) * cos(m*phi_p(p)+THETAh));
        end
    end
end

% Generate H_TA1, H_TA2, H_TB1, H_TB2, H_TC1, H_TC2, H_TD1, H_TD2 (transverse H)
for p = 1:1:P,
    for m=1:2:M,
        if phi_p(p) < phi_c
            H_TA1(p, (m+1)/2) = (BETAp2^2*((a+b)/2)/abs(besselj(m, BETAp2*b))) * (cos(phi_p(p))/rho(p)) * (BETAz/(BETAz^2-
            BETA2)) * (w*E2) * BETAp2 * (besselj(m-1, BETAp2*rho(p)) - (m/(BETAp2*rho(p))) * besselj(m, BETAp2*rho(p))) * sin(m*phi_p(p)+THETAe);
            H_TA2(p, (m+1)/2) = (BETAp2^2*((a+b)/2)/abs(besselj(m, BETAp2*b))) * (-sin(phi_p(p))/rho(p)) * (w*E2/(BETAz^2-
            BETA2)) * (m*besselj(m, BETAp2*rho(p)) * cos(m*phi_p(p)+THETAe));
            H_TB1(p, (m+1)/2) = (BETAp2^2*((a+b)/2)/abs(besselj(m, BETAp2*b))) * (cos(phi_p(p))/rho(p)) * (BETAz/(BETAz^2-
            BETA2)) * (m*besselj(m, BETAp2*rho(p)) * cos(m*phi_p(p)+THETAh));
            H_TB2(p, (m+1)/2) = (BETAp2^2*((a+b)/2)/abs(besselj(m, BETAp2*b))) * (sin(phi_p(p))/(BETAz^2-
            BETA2)) * BETAz * BETAp2 * (besselj(m-1, BETAp2*rho(p)) - (m/(BETAp2*rho(p))) * besselj(m, BETAp2*rho(p))) * sin(m*phi_p(p)+THETAh);
            H_TC1(p, (m+1)/2) = (ALPHAp1^2*((a+b)/2)/besselk(m, ALPHAp1*b)) * (cos(phi_p(p))/(BETAz^2-BETA1)) * (w*E1) * ALPHAp1 * (-
            besselk(m-1, ALPHAp1*rho(p)) - (m/(ALPHAp1*rho(p))) * besselk(m, ALPHAp1*rho(p))) * sin(m*phi_p(p)+THETAe);
            H_TC2(p, (m+1)/2) = (ALPHAp1^2*((a+b)/2)/besselk(m, ALPHAp1*b)) * (-sin(phi_p(p))/rho(p)) * (w*E1/(BETAz^2-
            BETA1)) * (m*besselk(m, ALPHAp1*rho(p)) * cos(m*phi_p(p)+THETAe));
            H_TD1(p, (m+1)/2) = (ALPHAp1^2*((a+b)/2)/besselk(m, ALPHAp1*b)) * (cos(phi_p(p))/rho(p)) * (BETAz/(BETAz^2-
            BETA1)) * (m*besselk(m, ALPHAp1*rho(p)) * cos(m*phi_p(p)+THETAh));
            H_TD2(p, (m+1)/2) = (ALPHAp1^2*((a+b)/2)/besselk(m, ALPHAp1*b)) * (sin(phi_p(p))/(BETAz^2-BETA1)) * BETAz * ALPHAp1 * (-
            besselk(m-1, ALPHAp1*rho(p)) - (m/(ALPHAp1*rho(p))) * besselk(m, ALPHAp1*rho(p))) * sin(m*phi_p(p)+THETAh);
        else
            H_TA1(p, (m+1)/2) = (BETAp2^2*((a+b)/2)/abs(besselj(m, BETAp2*b))) * (-sin(phi_p(p))/rho(p)) * (BETAz/(BETAz^2-
            BETA2)) * (w*E2) * BETAp2 * (besselj(m-1, BETAp2*rho(p)) - (m/(BETAp2*rho(p))) * besselj(m, BETAp2*rho(p))) * sin(m*phi_p(p)+THETAe);
            H_TA2(p, (m+1)/2) = (BETAp2^2*((a+b)/2)/abs(besselj(m, BETAp2*b))) * (-cos(phi_p(p))/rho(p)) * (w*E2/(BETAz^2-
            BETA2)) * (m*besselj(m, BETAp2*rho(p)) * cos(m*phi_p(p)+THETAe));
            H_TB1(p, (m+1)/2) = (BETAp2^2*((a+b)/2)/abs(besselj(m, BETAp2*b))) * (-sin(phi_p(p))/rho(p)) * (BETAz/(BETAz^2-
            BETA2)) * (m*besselj(m, BETAp2*rho(p)) * cos(m*phi_p(p)+THETAh));
        end
    end
end

```

```

H_TB2(p, (m+1)/2) = (BETAp2^2 * ((a+b)/2) / abs(besselj(m, BETAp2*b))) * (cos(phi_p(p)) / (BETAz^2 -
BETA2)) * BETAz * BETAp2 * (besselj(m-1, BETAp2*rho(p)) - (m / (BETAp2*rho(p))) * besselj(m, BETAp2*rho(p))) * sin(m*phi_p(p) + THETAh);
H_TC1(p, (m+1)/2) = (ALPHApl^2 * ((a+b)/2) / besselk(m, ALPHApl*b)) * (-sin(phi_p(p)) / (BETAz^2 -
BETA1)) * (w*E1) * ALPHApl * (-besselk(m-1, ALPHApl*rho(p)) - (m / (ALPHApl*rho(p))) * besselk(m, ALPHApl*rho(p))) * sin(m*phi_p(p) + THETAe);
H_TC2(p, (m+1)/2) = (ALPHApl^2 * ((a+b)/2) / besselk(m, ALPHApl*b)) * (-cos(phi_p(p)) / rho(p)) * (w*E1 / (BETAz^2 -
BETA1)) * (m * besselk(m, ALPHApl*rho(p)) * cos(m*phi_p(p) + THETAe));
H_TD1(p, (m+1)/2) = (ALPHApl^2 * ((a+b)/2) / besselk(m, ALPHApl*b)) * (-sin(phi_p(p)) / rho(p)) * (BETAz / (BETAz^2 -
BETA1)) * (m * besselk(m, ALPHApl*rho(p)) * cos(m*phi_p(p) + THETAh));
H_TD2(p, (m+1)/2) = (ALPHApl^2 * ((a+b)/2) / besselk(m, ALPHApl*b)) * (cos(phi_p(p)) / (BETAz^2 - BETA1)) * BETAz * ALPHApl * (-
besselk(m-1, ALPHApl*rho(p)) - (m / (ALPHApl*rho(p))) * besselk(m, ALPHApl*rho(p))) * sin(m*phi_p(p) + THETAh);

```

end

end

end

% Add up the submatrices to form the main matrices

E\_TA = E\_TA1 + E\_TA2;

E\_TB = E\_TB1 + E\_TB2;

E\_TC = E\_TC1 + E\_TC2;

E\_TD = E\_TD1 + E\_TD2;

H\_TA = H\_TA1 + H\_TA2;

H\_TB = H\_TB1 + H\_TB2;

H\_TC = H\_TC1 + H\_TC2;

H\_TD = H\_TD1 + H\_TD2;

% Generating G matrix

Z = zeros(P, H);

```

G = [E_LA    Z    -E_LC    Z
      Z    H_LB    Z    -H_LD
      E_TA    E_TB    -E_TC    -E_TD
      H_TA    H_TB    -H_TC    -H_TD];

```

% Calculate the determinant of the G matrix

det\_G = det(G);



## APPENDIX B

---

### Frame

The frame used to measure the holographic antennas is illustrated in Figure B.1.

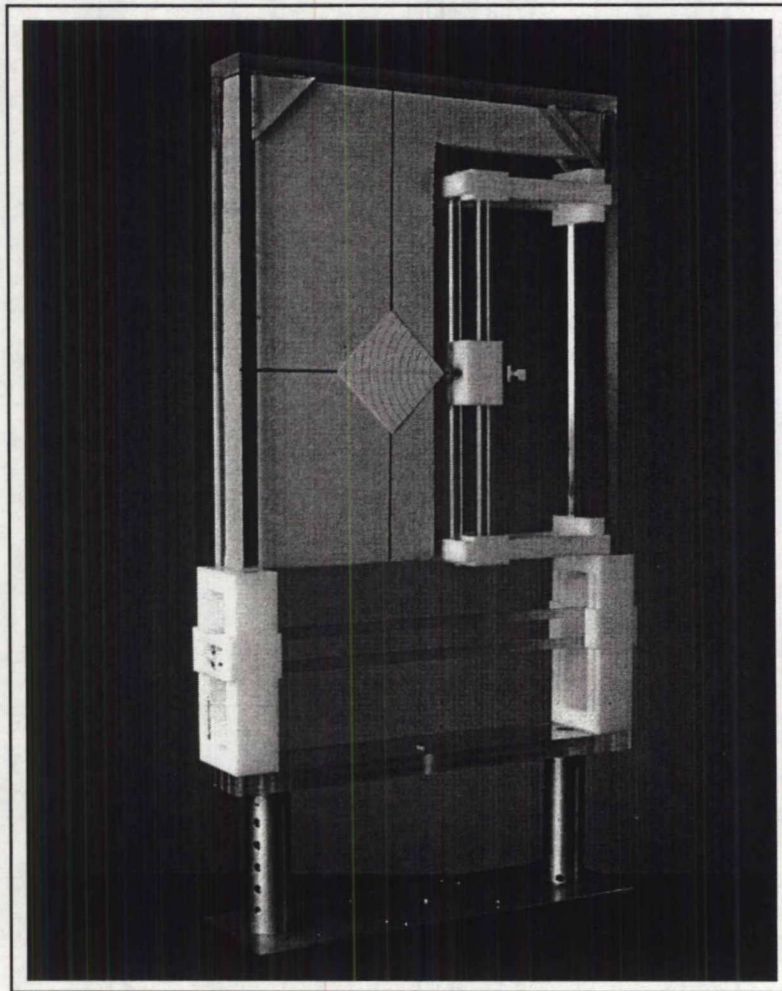


**Figure B.1. Frame.**

The frame's width  $w_1$  is approximately  $46\text{cm}$  and the height  $h_1$  of the foam section is  $55\text{cm}$  as illustrated in Figure B.2. The foam's uncut section on which the hologram is placed in the above picture has a width  $w_2$  of  $23.5\text{cm}$ .



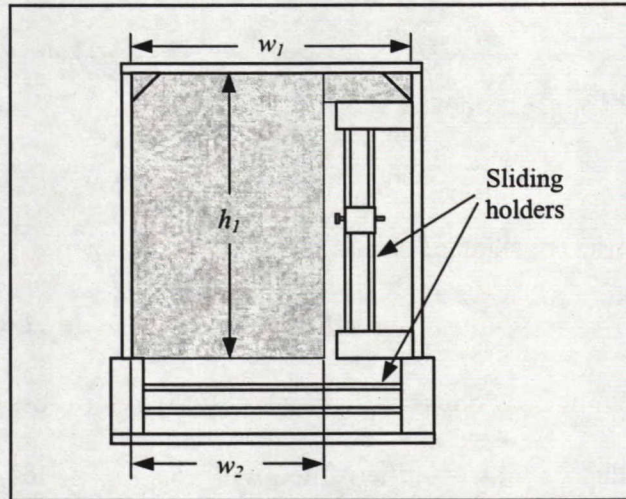


**Figure B.2. Dimensions.**

The materials used to design the frame are plexiglass, delrin and foam. The feed can be adjusted in the  $x$ ,  $y$ ,  $z$  coordinate system such that it is properly focused with the holographic plate. The feed can also be set up to measure both planes of the antenna by simply moving the open waveguide from the bottom sliding holder (E-plane) to the side one (H-plane). Every component of the frame can be adjusted or removed with the help of screws. Note that foam is used instead of a metal back plane because the holographic antenna has no ground plane.



## APPENDIX C

### Evaluation of the Dielectric Constant of the Foam

Ideally, the dielectric constant of the foam used to mount the antenna should be very close to that of air ( $\epsilon_r = 1$ ). To confirm this affirmation the dielectric constant of the foam was evaluated experimentally. The idea consists in measuring the return loss (amplitude and phase) of a shorted waveguide filled with air and then filled with foam. The test setup for this analysis is shown in Figure C.1.

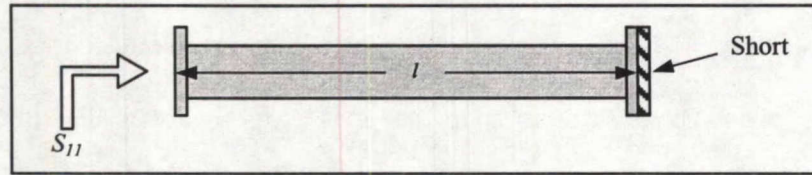


**Figure C.1. Open waveguide test setup.**

The reflection coefficient can be expressed as:

$$S_{11}^a = |S_{11}^a| e^{j\phi_a} = |S_{11}^a| e^{j2\beta_z^a l}, \quad (\text{C-1})$$

for the air filled waveguide case and

$$S_{11}^f = |S_{11}^f| e^{j\phi_f} = |S_{11}^f| e^{j2\beta_z^f l}, \quad (\text{C-2})$$

for the foam filled waveguide assuming the materials are lossless. The phase constant  $\beta_z$  of the waveguide is:

$$\beta_z = \pm \kappa \sqrt{1 - \left(\frac{f_c}{f}\right)^2}, \quad (\text{C-3})$$

where  $\kappa = 2\pi f \sqrt{\mu \epsilon_0 \epsilon_r}$ ,  $f_c$  is the cutoff frequency of the waveguide,  $f$  is the operating frequency, and  $l$  is the length of the waveguide. The cutoff frequency is expressed as:



$$f_c = \frac{1}{2a\sqrt{\mu\epsilon}}, \quad (\text{C-4})$$

where  $a$  is one of the dimensions of the waveguide ( $a = 7.112\text{mm}$ ). Taking the phase difference between the return losses ( $\phi_a - \phi_f = \Delta\phi$ ), the phase constant of the foam filled waveguide becomes:

$$\beta_z^f = \frac{\Delta\phi}{2l} - \beta_z^a, \quad (\text{C-5})$$

where  $\beta_z^a$  is evaluated theoretically (for  $f_c = f_c^a$ , and  $\epsilon_r = 1$ ) and  $\Delta\phi$  is calculated from the measured results.

At various frequencies, the return loss was measured and the phase difference at these frequencies is listed in Table C.1.

**Table C.1 Return loss measurements**

Frequency $f$ [GHz]	Amplitude $\Delta S_{11}  =  S_{11}^a  -  S_{11}^f $	Phase $\phi_a - \phi_f = \Delta\phi$
28.000	-0.271dB	-136.43°
29.008	-0.126dB	-128.54°
30.016	-0.117dB	-123.85°
31.000	-0.025dB	-133.35°
32.000	-0.612dB	-143.64°

Using (C-5) and the above results,  $\beta_z^f$  (for  $f_c = f_c^f$ , and  $\epsilon_r = \epsilon_r^f$ ) can be evaluated at each frequency and the dielectric constant of the foam, derived from (C-3), can be expressed as:

$$\epsilon_r^f = \frac{a^2 \beta_z^f + \pi^2}{(2\pi f a)^2 \mu \epsilon_0}, \quad (\text{C-6})$$

which is listed at various frequencies in Table C.2.

**Table C.2 Dielectric constant of foam**

<b>Frequency <math>f</math> [GHz]</b>	<b>Dielectric constant <math>\epsilon_r^f</math></b>
<i>28.000</i>	<i>1.04</i>
<i>29.008</i>	<i>1.03</i>
<i>30.016</i>	<i>1.03</i>
<i>31.000</i>	<i>1.04</i>
<i>32.000</i>	<i>1.04</i>

Based on the results listed in Table C.2 the dielectric constant of the foam is very close to the air dielectric constant.

## APPENDIX D

### H-Plane Sectoral Horn and Pyramidal Horn

#### D.1 H-Plane Sectoral Horn

The H-plane sectoral horns are fabricated based on the design guidelines described in [19, Section 12.3]. The horns must be attached to the open waveguide such that they can be mounted onto the frame. The dimensions of the open waveguide (WR28), which are useful for the horn design, are illustrated in Figure D.1.

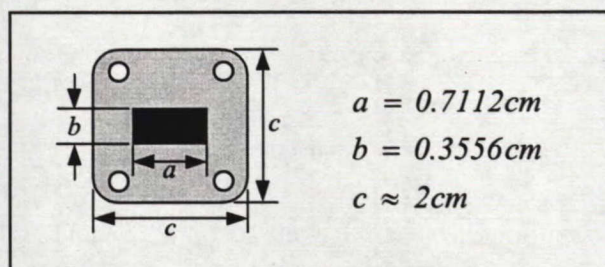


Figure D.1. Dimensions of open waveguide.

Three horns are designed with different beamwidths where the dimensions of the horns, described in Figure D.2 and Table D.1, are selected to reduce the phase errors ( $\delta$ ). Note that the dimensions  $a$  and  $b$  are the same as in Figure D.1.

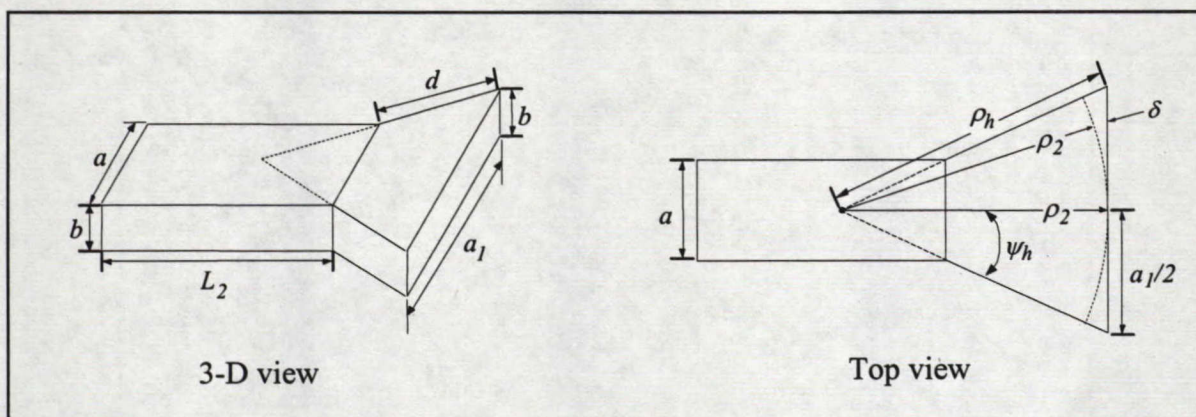


Figure D.2. Dimensions of the H-plane sectoral horn.



**Table D.1 H-plane sectoral horn characteristics**

H-plane Beamwidth	$\rho_2$	$2\cdot\psi_h$	$a_1$ [cm]	$d$ [cm]	Phase error ( $\delta$ )	Simulated beamwidth
20°	$10\lambda$	20.41°	3.60	8.153	0.162	19.23°
30°	$10\lambda$	13.24°	2.32	6.978	0.068	29.12°
40°	$10\lambda$	10.00°	1.75	5.959	0.038	38.17°

The center frequency of operation is  $f_o = 30\text{GHz}$  ( $\lambda \approx 1\text{cm}$ ). The last column of the above table shows the beamwidth simulation results found with **ARPS**. The E-plane beamwidth should be similar to the open waveguide (around  $100^\circ$ ) since the aperture width ( $b$ ) of both feeds is the same. The phase error (or phase deviation) was evaluated [28, Chapter 10] using the following expression:

$$\delta = \frac{a_1^2}{8\lambda\rho_2}, \quad (\text{D-1})$$

where  $\delta$  is the number of wavelengths. Usually, an acceptable phase error value is  $45^\circ$  (0.125).

The horns were machined in two pieces and put together with screws as shown in Figure D.3.

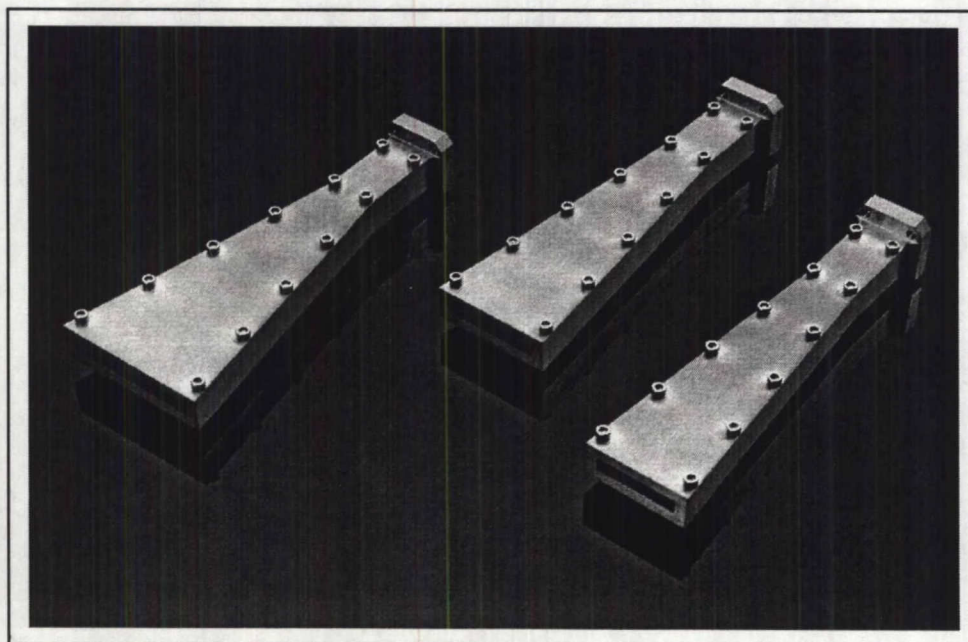


**Figure D.3. H-plane sectoral horns.**



Due to some fabrication errors, all the horns have a length of  $d = 8.153\text{cm}$ , which means that the feeds have the new specifications illustrated in Table D.2. Basically the error translates into a change of aperture size, a smaller beamwidth (BW) and a slight phase error increase.

**Table D.2 New H-plane sectoral horn characteristics**

H-plane Beamwidth	$\rho_2$	$2\cdot\psi_h$	$a_1$ [cm]	$D$ [cm]	Phase error ( $\delta$ )	Simulated beamwidth
$20^\circ$	$10\lambda$	$20.41^\circ$	3.60	8.153	0.162	$19.23^\circ$
$28^\circ$	$11.2\lambda$	$13.24^\circ$	2.59	8.153	0.075	$26.17^\circ$
$37^\circ$	$12.2\lambda$	$10.00^\circ$	2.13	8.153	0.047	$31.58^\circ$

The measured radiation patterns of each horn are illustrated in Figures D.4 to D.6 and Table D.3 summarizes these results.

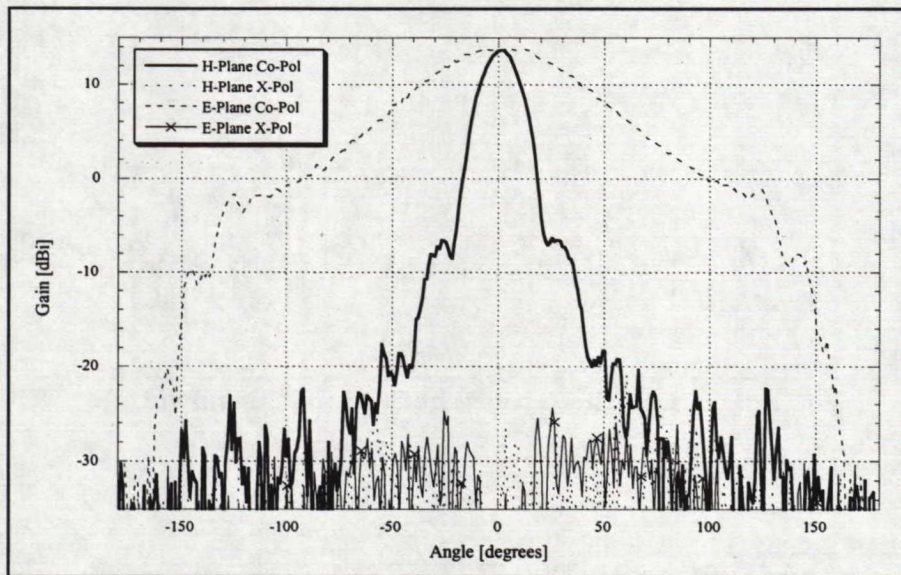


**Figure D.4. H-plane sectoral horn #1 ( $20^\circ$  Beamwidth).**



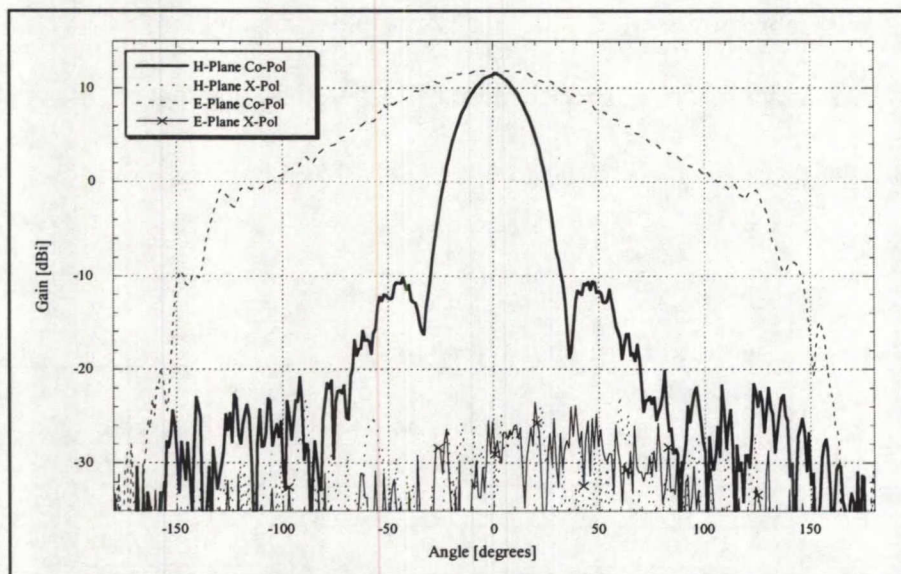


**Figure D.5. H-plane sectoral horn #2 (28° Beamwidth).**

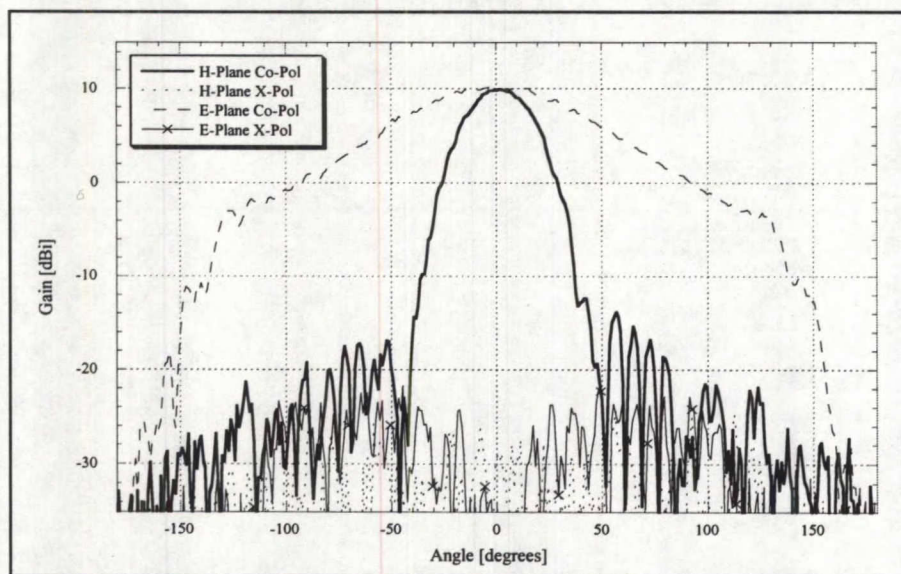


**Figure D.6. H-plane sectoral horn #3 (37° Beamwidth).**

**Table D.3 H-plane sectoral horn results**

Horn	Theoretical H-plane BW	Simulated H-plane BW	Measured H-plane BW	Measured E-plane BW
1	20°	19.23°	16.86°	66.67°
2	28°	26.17°	25.86°	82.18°
3	37°	31.58°	32.33°	81.81°



Compared to the waveguide discussed in Chapter 4, Section 4.2, the sectoral horns offer a higher gain and a uniform E-plane pattern. Gain is not a critical issue since the horns were designed to provide a certain beamwidth and not to obtain a high directivity. The measured H-plane beamwidths are close to the simulated values and within  $4^\circ$  from the theoretical values. Note that the horns' dimensions were selected based on a half-power beamwidth versus the total flare angle  $2\psi_h$  in [19] and it was very difficult, for a desired beamwidth, to read off the angle value on the design curves. Therefore, one should expect some slight variations between the experimental results and the theoretical values.

The cross-polarization of the horns is better than  $31dB$  corresponding to a  $5dB$  improvement compared to the open waveguide. The E-plane beamwidth, however, is not as wide as expected (for the three cases the simulated E-plane bandwidth was around  $104.3^\circ$ ). In fact, the half power-beamwidth is less than the required  $90^\circ$ , which is probably caused by edge diffraction on the metal edges around the open aperture of the horns as shown in Figure D.7.

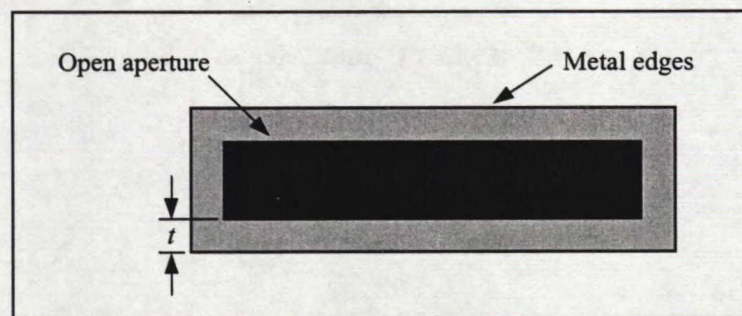


**Figure D.7. Open aperture of H-plane sectoral horns.**

Initially the thickness  $t$  was supposed to be less than a millimeter, but after the fabrication process it was  $3mm$ . It is possible to improve the performance of the horns by reducing the thickness  $t$  of the edges around the aperture but this issue is not investigated in this thesis.



To complete the analysis, the return loss of each horn was also measured and is illustrated in Figure D.8. In general the return loss is better than  $10\text{dB}$  across the entire frequency range of interest. The little mismatch at certain frequencies can be attributed to interface reflections between the horns and the waveguide that was used to excite the horns and to mount them onto the frame.

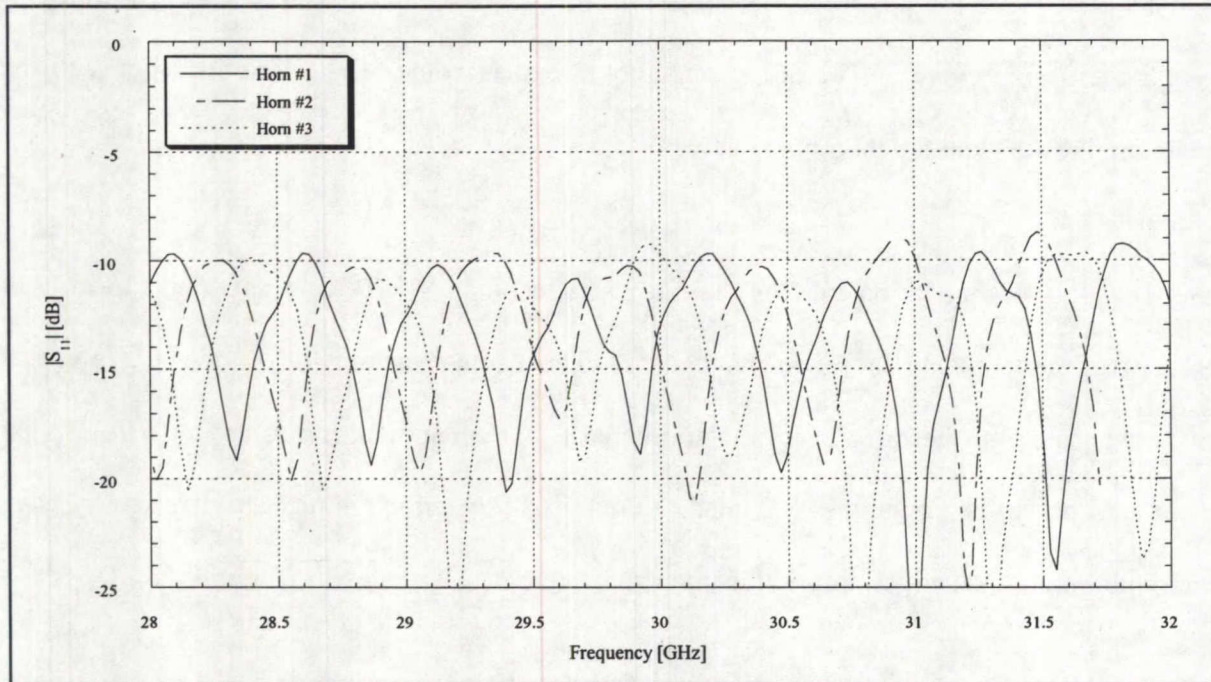


**Figure D.8.**  $|S_{11}|$  of H-plane sectoral horns.

## D.2 Pyramidal Horn

### D.2.1 General description

Along with the H-plane sectoral horn, an in-house pyramidal horn was considered as a possible feed structure for the holographic antennas. The pyramidal horn has an open aperture of approximately  $2.3\text{cm} \times 1.7\text{cm}$  and extends out by  $1.5\text{cm}$  as shown in Figure D.9. The radiation pattern of the pyramidal horn is illustrated in Figure D.10 and the return loss in Figure D.11.



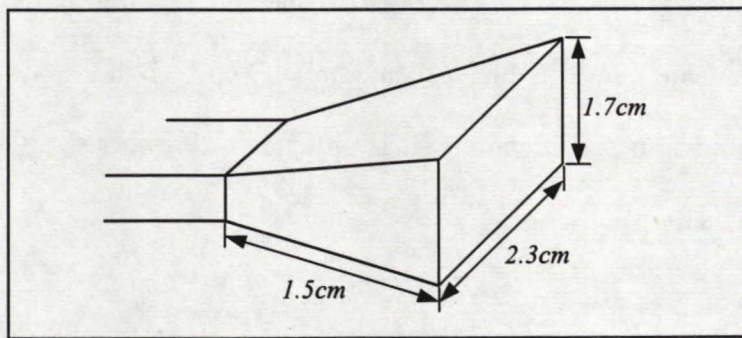


**Figure D.9. Pyramidal horn.**

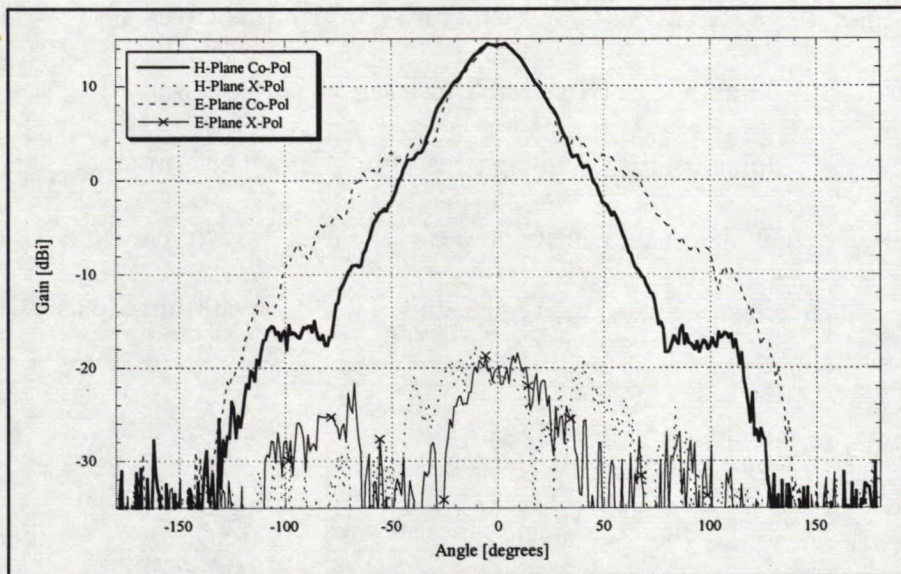


**Figure D.10. Radiation patterns of pyramidal horn (horn #4).**

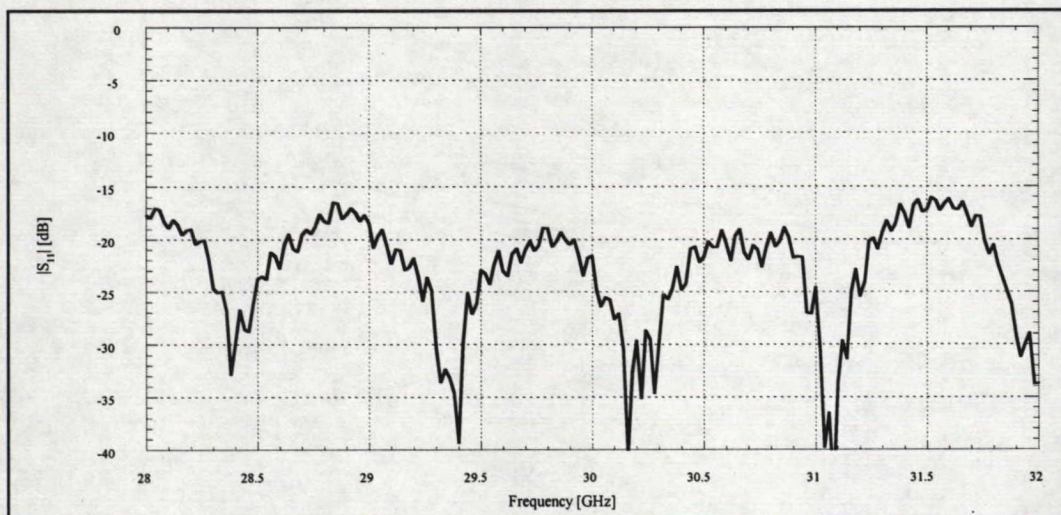


**Figure D.11.  $|S_{11}|$  of pyramidal horn.**



The H-plane beamwidth of the measured patterns is  $30.88^\circ$  and the E-plane beamwidth is  $30.53^\circ$ . The cross-polarisation level is better than  $32dB$ . Even though the pyramidal horn does not quite meet the beamwidth specifications, it is still interesting to see how the holographic antenna behaves with this horn.

### D.2.2 Apex and phase center

With a horn, there are two possible points from which the waves are generated: the apex or the phase center. The apex can be referred to as the near-field point source and the phase center as the far-field point source. The apex is simply evaluated from the geometry of the structure and for a rectangular open aperture, the E-plane apex is different from the H-plane. For the pyramidal horn considered above, the H-plane apex is evaluated from Figure D.12.

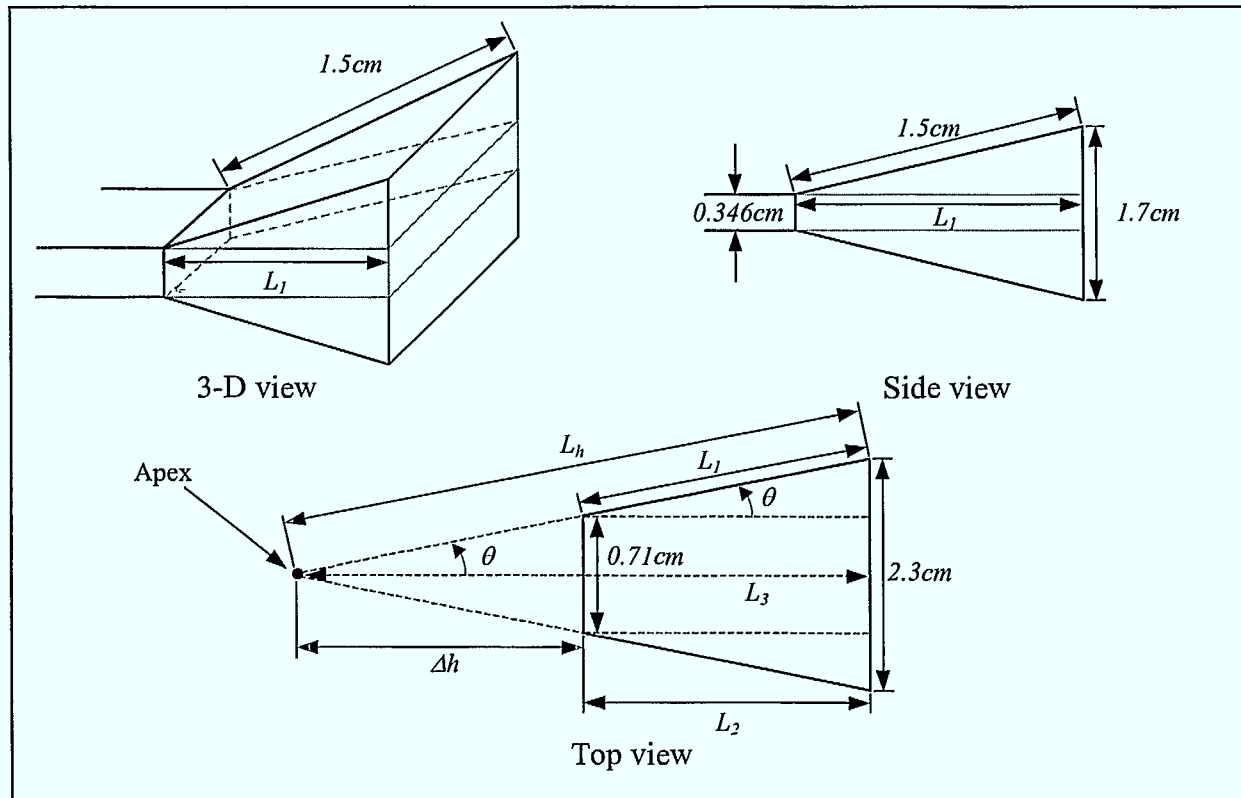


Figure D.12. H-plane apex.

From the dimensions in the side view,  $L_1$  is:

$$L_1 = \sqrt{(1.5)^2 - \left(\frac{1.7 - 0.346}{2}\right)^2} = 1.34cm. \quad (D-2)$$

$L_2$  can now be determined, and from the top view:

$$L_2 = \sqrt{(L_1)^2 - \left(\frac{2.3 - 0.71}{2}\right)^2} = 1.08cm. \quad (D-3)$$

From (D-2) and (D-3), the angle  $\theta$  becomes:

$$\theta = \arccos\left(\frac{L_2}{L_1}\right) = 36.44^\circ, \quad (D-4)$$

and the distance between the apex and the center of the open aperture is:

$$L_3 = L_2 + \Delta h = \frac{2.3}{2 \tan(\theta)} = 1.56cm, \quad (D-5)$$

where  $\Delta h = L_3 - L_2 = 0.48cm$ . Using (D-4) and (D-5),  $L_h$  is found to be:

$$L_h = \frac{L_1}{\cos(\theta)} = 1.94cm. \quad (D-6)$$

The same derivation must be applied for the E-plane apex, which is evaluated based on Figure D-13. From the dimensions in the top view,  $L_1$  is:

$$L_1 = \sqrt{(1.5)^2 - \left(\frac{2.3 - 0.71}{2}\right)^2} = 1.27cm. \quad (D-7)$$

$L_2$  can now be determined, and from the side view:

$$L_2 = \sqrt{(L_1)^2 - \left(\frac{1.7 - 0.346}{2}\right)^2} = 1.08cm. \quad (D-8)$$

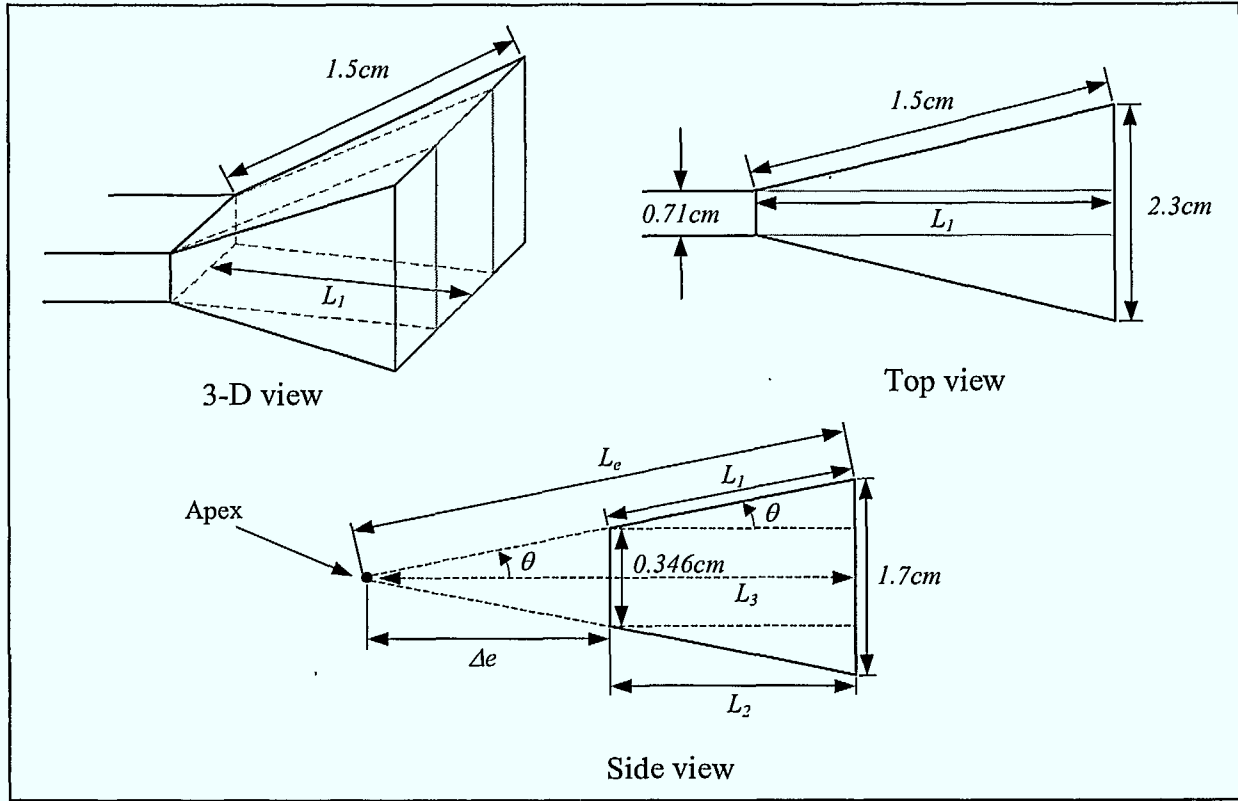


**Figure D.13. E-plane apex.**

From (D-7) and (D-8), the angle  $\theta$  becomes:

$$\theta = \arccos\left(\frac{L_2}{L_1}\right) = 32.16^\circ, \quad (\text{D-9})$$

and the distance between the apex and the center of the open aperture is:

$$L_3 = L_2 + \Delta e = \frac{1.7}{2 \tan(\theta)} = 1.35 \text{ cm}, \quad (\text{D-10})$$

where  $\Delta e = L_3 - L_2 = 0.27 \text{ cm}$ . Finally using (D-9) and (D-10),  $L_e$  is found to be:

$$L_e = \frac{L_1}{\cos(\theta)} = 1.60 \text{ cm}. \quad (\text{D-11})$$

The phase center, which is derived mathematically in the far-field region, was evaluated for different types of horns [29]. Again like the apex, the E and H-plane phase centers are



different. For the pyramidal horn described above, the phase center point with respect to the open aperture of both planes was found graphically from design curves in [29] and are listed, along with the apex points, in Table D.4.

**Table D.4 Apex and phase center of pyramidal horn**

<b>Plane</b>	<b>Apex [cm]</b>	<b>Phase center [cm]</b>
H-plane	<i>1.56</i>	<i>0.8</i>
E-plane	<i>1.35</i>	<i>0.9</i>

## REFERENCES

---

1. G. Heftman, "LMDS Set to Challenge for Last-Mile Supremacy", *Microwaves & RF*, vol. 38, no. 4, April 1999, pp. 30-38.
2. B. Pontano, "Satellite Communications: Services, Systems & Technologies", *1998 IEEE MTT-S Digest*, 1998, p. TU1A-1.
3. B. Wignall, "LMCS – a technical primer", *Wireless Telecom*, vol. 14, no. 4, 1996, pp. 23-25.
4. W.E. Kock, "Microwave Holography", *Microwaves*, November 1968, pp. 46-54.
5. K. Iizuka *et al.*, "Volume-Type Holographic Antenna", *IEEE Transactions on Antennas and Propagation*, vol. AP-23, November 1975, pp. 807-810.
6. D.J. Rochblatt and B.L. Seidel, "Microwave Antenna Holography", *IEEE Transactions on Microwave Theory and Techniques*, vol. 40, no. 6, June 1992, pp. 1294-1300.
7. T. Hirvonen, *et al.*, "A Compact Antenna Test Range Based on a Hologram", *IEEE Transactions on Antennas and Propagation*, vol. 45, no. 8, August 1997, pp. 1270-1276.
8. G.C. James *et al.*, "Panel Setting from Microwave Holography by the Method of Successive Projections", *IEEE Transactions on Antennas and Propagation*, vol. 41, no. 11, November 1993, pp. 1523-1529.
9. P.F. Checcacci *et al.*, "A Holographic VHF Antenna", *IEEE Transactions on Antennas and Propagation*, vol. AP-19, March 1971, pp. 278-279.
10. P.F. Checcacci *et al.*, "Holographic Antennas", *IEEE Transactions on Antennas and Propagation*, vol. AP-18, no. 6, November 1970, pp. 811-813.
11. E.C. Jordan and K.G. Balmain, Electromagnetic Waves and Radiation Systems, Second ed., New Jersey: Prentice-Hall, Inc., 1968.
12. J.W. Goodman, "An Introduction to the Principles and Applications of Holography", *Proceedings of the IEEE*, vol. 59, no. 9, September 1971, pp. 1292-1304.
13. J.W. Goodman, Introduction to Fourier Optics, Second ed., New York: The McGraw-Hill Companies, Inc., 1996.
14. P. Hariharan, Optical Holography – Principles, techniques, and applications, Second ed., Cambridge: Cambridge University Press, 1996.

15. S. Ramo, *et al.*, Fields and Waves in Communication Electronics, Third ed., New York: John Wiley & Sons, Inc., 1994.
16. A.H. Cook, Interference of Electromagnetic Waves, Oxford: Clarendon Press, 1971.
17. G.W. Stroke, An Introduction to Coherent Optics and Holography, New York: Academic Press, Inc., 1966.
18. G. Tricoles and N.H. Farhat, "Microwave Holography: Application and Techniques", *Proceedings of the IEEE*, vol. 65, no. 1, January 1977, pp. 108-121.
19. C.A. Balanis, Antenna Theory – Analysis and Design, New York: John Wiley & Sons, Inc., 1982.
20. MathSoft, Mathcad 6.0, Cambridge: MathSoft, Inc., 1995.
21. **Far Field**, ARPS, Antenna Radiation Pattern Software – User's guide, Canada: **Far Field**, 1998.
22. P. Berini, "Numerical Methods in Electromagnetic Engineering", ELG5379 course notes, University of Ottawa, 1998.
23. MathWorks, MATLAB 5.1, Natick: The MathWorks, Inc., 1997.
24. C.H. Walter, Traveling Wave Antennas, New York: Dover Publications, Inc., 1965.
25. R.E. Collin and F.J. Zucker, Antenna Theory- part 2, New York: McGraw-Hill Book Company, 1969.
26. P. Berini, "Wave Transmission Media", ELG4103 course notes, University of Ottawa, 1996.
27. R.J. Mailloux, Phased Array Antenna Handbook, Boston: Artech House, Inc., 1994.
28. H. Jasik, Antenna Engineering Handbook, New York: McGraw-Hill, Inc., 1961.
29. E.I. Muehldorf, "The Phase Center of Horn Antennas", *IEEE Transactions on Antennas and Propagation*, vol. AP-18, no. 6, November 1970, pp. 753-760.



LKC  
TK5102.5 .C673e #2000-002  
c.2  
Ka-band holographic antennas

**DATE DUE**  
DATE DE RETOUR

[illegible]

